



Libraries and Learning Services

University of Auckland Research Repository, ResearchSpace

Copyright Statement

The digital copy of this thesis is protected by the Copyright Act 1994 (New Zealand).

This thesis may be consulted by you, provided you comply with the provisions of the Act and the following conditions of use:

- Any use you make of these documents or images must be for research or private study purposes only, and you may not make them available to any other person.
- Authors control the copyright of their thesis. You will recognize the author's right to be identified as the author of this thesis, and due acknowledgement will be made to the author where appropriate.
- You will obtain the author's permission before publishing any material from their thesis.

General copyright and disclaimer

In addition to the above conditions, authors give their consent for the digital copy of their work to be used subject to the conditions specified on the [Library Thesis Consent Form](#) and [Deposit Licence](#).

THE UNIVERSITY OF AUCKLAND

DOCTORAL THESIS

**Optimising Recording &
Stimulation Performance of
Neuronal Microelectrode Arrays
through Macroporous
Conducting Polymer
Modification**

Author:

Zaid AQRAWA

*A thesis submitted in partial fulfillment of the requirements
for the degree of Doctor of Philosophy*

in the

School of Pharmacy

February 26, 2018

“The unexamined life is not worth living.”

— Socrates

Abstract

Microelectrodes are commonly used to interface with electrically active cells, such as neurons (typically as an array of microelectrodes) allowing for their monitoring (recording) and manipulation (stimulation). Recent trends towards smaller electrodes for improved spatial resolution have revealed limitations of conventional planar microelectrode materials, such as gold and platinum, due to the subsequent reduction in electrochemical surface area. Strategies utilised to increase electrochemical surface area whilst maintaining the desired geometric area involve modification with rough, conductive electrode coatings, such as conducting polymers (CPs). This research aims to investigate a macroporous templated CP based on poly(3,4-ethylenedioxythiophene)/polystyrene sulphonate (PEDOT/PSS) hypothesised to further increase electrochemical surface area of conventional CP coatings. The enlarged electrochemical surface area offered is hypothesised to improve (i) recording, through reduced impedance and thermal noise and (ii) stimulation, through increased cathodic charge storage capacity (CSC_c) and charge injection limits (CIL). Alongside microelectrode modification, we hypothesise that the refinement of recording instrumentation (amplifier and digitiser) required to acquire signals from MEA devices will compliment reduced thermal noise of modified microelectrodes, yielding a low noise recording and stimulation set-up. This research aims to produce an amplifier with intrinsic noise levels 45% (or less) that of microelectrode thermal noise.

Conventional and macroporous PEDOT/PSS coated microelectrodes were deposited onto custom made gold MEAs at four increasing charge densities (32, 127, 318 and 637 $mC\ cm^{-2}$) using both potentiostatic and galvanostatic electrochemical deposition. Scanning electron microscopy confirmed the presence of macropores within the CP structure. Electrochemical characterisation for properties central to neuronal recording and stimulation, comprised (i) cyclic voltammetry (CV) to yield CSC_c , (ii) voltage transient measurements (VTM) to yield CIL and (iii) electrochemical impedance spectroscopy (EIS) to yield impedance spectra and thermal noise estimates. All CP coatings drastically improved electrochemical properties of gold and this effect was more apparent

as deposition charge density increased. Comparisons between conventional PEDOT/PSS and macroporous PEDOT/PSS coatings revealed (i) no significant difference in CSC_c for all deposition charge densities, (ii) a significant increase in CIL at the highest deposition charge density of 637 mC cm^{-2} from $6.4 \pm 0.3 \text{ mC cm}^{-2}$ to $8.8 \pm 0.3 \text{ mC cm}^{-2}$ ($p < 0.05$), (iii) a significant reduction in impedance magnitude (at 100 Hz) at the highest deposition charge density of 637 mC cm^{-2} from $59 \pm 5 \text{ k}\Omega$ to $41 \pm 1 \text{ k}\Omega$ ($p < 0.05$) and (iv) a significant reduction in predicted thermal noise amplitude at the highest deposition charge density of 637 mC cm^{-2} from $12.6 \pm 0.3 \mu\text{V}_{p-p}$ to $10.5 \pm 0.6 \mu\text{V}_{p-p}$ ($p < 0.05$). No differences in electrochemistry were observed between potentiostatic and galvanostatic deposition methods. Stability studies, performed through long-term biphasic current injection, revealed conventional PEDOT/PSS coatings were less prone to delamination. However, macroporous PEDOT/PSS coatings exhibited an improvement in impedance throughout the time-course of the experiment, followed by abrupt delamination. Neurite outgrowth and viability assays, indicated the biocompatibility of both conventional and macroporous PEDOT/PSS coatings alongside primary hippocampal neurons.

An amplification system was designed and coupled with an analog to digital converter from National Instruments to produce a low noise neuronal data acquisition system for the MEA devices. The amplifier was (i) operated between 0 and 5 V utilising a DC battery power supply, (ii) had a bandwidth of 10 kHz, (iii) removed DC voltage created at the electrode/electrolyte interface with a high-pass cut-off frequency of 0.7 Hz and (iv) had a gain of 2000. An offset voltage of 2.5 V was employed to allow for amplification of both negative and positive signals, due to the biphasic nature of neuronal action potentials. Strategies to reduce environment electromagnetic interference at the amplifier front end were employed and involved a customised neural interface board connected between the MEA and amplifier. A final intrinsic noise amplitude of $4.6 \mu\text{V}_{p-p}$ was achieved and met the threshold target of $< 45\%$ of the microelectrode thermal noise for unmodified gold as well as for the lower thermal noise of conventional PEDOT/PSS and macroporous PEDOT/PSS coatings.

In-vitro characterisation involved noise floor measurements pre- and post-culture to investigate microelectrode biofouling susceptibility and measurement of spontaneous neuronal activity alongside primary hippocampal cells. Conventional and macroporous PEDOT/PSS coatings both outperformed gold with pre-culture noise amplitudes at 18 ± 1 and $19 \pm 2 \mu\text{V}_{p-p}$, compared to $36 \pm 3 \mu\text{V}_{p-p}$ for gold. All microelectrode materials were susceptible to biofouling, however, both CP coatings still exhibited a smaller noise floor than gold. Conventional PEDOT/PSS coatings displayed the highest number of active recordings and recording performance, as measured via a signal to noise ratio (SNR). The maximum SNR values achieved for gold, conventional PEDOT/PSS and macroporous PEDOT/PSS were 2.7, 12.6 and 17.6, respectively. Results for *in-vitro* stimulation efficacy were not obtained due to limitations of the MEA devices used. The large inter-electrode distance on the MEA devices resulted in the use of the same microelectrode for both stimulation and recording. Noise introduced from the voltage source and post-stimulus artifacts made recording direct neuronal responses difficult. Furthermore, the young age of cultures ($< \text{DIV } 14$) may have contributed to insufficient activity post-stimulus.

In conclusion, the work presented here reveals macroporous CP coatings, at deposition charge densities of above 318 mC cm^{-2} , provide subtle advantages in electrochemical parameters central to neuronal recording and stimulation as compared to conventional PEDOT/PSS coatings. Macroporous PEDOT/PSS coatings displayed potential for long-term stimulation applications as observed through high CIL and improvements in impedance during long-term biphasic stimulation. However, strategies to improve substrate adhesion are required for their successful implementation. Recording instrumentation was successfully designed and constructed, facilitating low-noise recording of neuronal activity from primary hippocampal neurons. No additional benefit was introduced from macroporous PEDOT/PSS coatings when compared to conventional PEDOT/PSS coatings during *in-vitro* spontaneous recordings. Unfortunately, no data was obtained following *in-vitro* stimulation at both DIV 7 and DIV 14. Future *in-vitro* stimulation experiments could be refined through the use of paired stimulating and recording microelectrodes and by exploring cultures aged $> \text{DIV } 14$.

Acknowledgements

This project would have never been possible without the support and guidance from a wide range of people. First, I would like to thank my family - to Mum and Dad, thank you for providing a roof over my head and food on the table and thank you for being there to guide and keep me focused on the bigger picture - your endless love and support has turned me into the man I am today. To my brothers, Waled and Mark, you have always been there to talk to and I am grateful to have brothers like you! Special shout out to Mark who kept the childish side of me alive through PlayStation - I know Mum hates me for it. To my uncle, Muzahim, thank you for your love and support during this PhD, thank you for believing in me. To Saad, life would be boring without you. To Teta, Nana, Aunty Sahar & Amo Ammar thank you for the love, food and laughter. Special shout out to all my extended family and cousins & a BIG hello to Wadea for always making me laugh. To the retards, Rayan and Maryam, thank you for always being there when I need to talk and thank you for the gift of Alessa.

First equal, to my primary supervisor Dr Darren Svirskis - I would have never found my love for research if it wasn't for you. You have gone above and beyond to help me throughout this project. At times it may have felt like we didn't know what was going on, but you never failed to put me in contact with someone who did! A true example of a great supervisor.

To my co-supervisors Professor Jadranka Travas-Sejdic and A/Professor Johanna Montgomery, your expertise has helped me immensely and your door has always been open for discussion - thank you for your guidance and support.

Thank you to everyone who help run the pharmacy labs and to the postgrad

students; Emma, Mahima, Mimi and Saiful. To everyone in Jo's group - Yukti, Chantelle, Kevin, Jesse and Wojciech - you have been a great help for someone who knew close to nothing about neuronal electrophysiology. Special shout out to Yukti who provided me with beautiful cultures and selflessly helping me resolve any problems I had during the culture process.

To Dr Byron Wright, your microfabrication skills gave me a crucial starting point for the project. To Dr Nitish Patel, your expertise in electronics and enthusiasm for the project has been pivotal in its completion - thank you both for your help and guidance.

To Sir Moses 'Sensei' Kaufusi, if everyone was as patient as you were with me, the world would be a better place. You gave me a huge wake up call and have taught me to keep pushing even when times are tough. It's unfortunate I never got a shot at the heavy-weight title, but its safe to say that I was 'close'.

To my all my friends, thank you for keeping me sane throughout these 3 years. To Mimi, thank you for everything, you were always there when times got tough. To Mary, the sister I never had, or wanted. Thank you for your help throughout the ups and downs. You have a special knack for knowing when I'm under stress, and you've never failed to make me stress out more. To John, you've always been there to talk to although you're half way across the world now. Its safe to call you my third brother, but please stop calling me in the early hours of the morning. To Oscar & Sonny, hi and thank you for contributing to who I am today, I know your influence wasn't always 'positive'. To Bish and Maikel, thanks for the countless KFC sessions, we always regret it after but we keep going back. Special thanks to Mustafa and Ali, who have helped me directly with this project. I know most people shy away from talking about the details of a PhD, but you both seem to love it. Weird.

Research Outputs Arising from this Thesis

Publications

Agrawe Z, Montgomery J, Travas-Sejdic J, Svirskis D. The Influence of Conducting Polymers on Neuronal Multi-Electrode Array Recording, Stimulation and Performance Stability. *Sensors & Actuators: B. Chemical*. 2018. DOI: 10.1016/j.snb.2017.11.023

Agrawe Z, Montgomery J, Travas-Sejdic J, Svirskis D. Conducting Polymers as Electrode Coatings for Neuronal Multi-electrode Arrays. *Trends in Biotechnology*. 2016; 35:93-95. DOI: <http://dx.doi.org/10.1016/j.tibtech.2016.06.007>

Agrawe Z, Vyas Y, Patel N, Wright B, Malmstrom J, Montgomery J, Williams D, Travas-Sejdic J, Svirskis D. The Influence of Macropores on the Recording Performance, Stability and Biocompatibility of Conventional PEDOT/PSS Microelectrodes Intended for Neural Interfacing. *Intended for submission to Biomaterials*.

Agrawe Z, Vyas Y, Patel N, Montgomery J, Travas-Sejdic J, Svirskis D. Neuronal Stimulation Efficacy/Safety of Macroporous PEDOT/PSS Microelectrode Coatings. *Intended for submission to Acta Biomaterialia*.

Agrawe Z, Patel N, Vyas Y, Montgomery J, Travas-Sejdic J, Svirskis D. Design of a Simultaneous Optical and Electrical *In-vitro* Neuronal Recording System with High Spatiotemporal Resolution. *Intended for submission to IEEE Transactions on Biomedical Engineering*.

Refereed Full Conference Papers

Agrawe Z, Patel N, Montgomery J, Travas-Sejdic J, Svirskis D. Microelectrode Modification with Macroporous PEDOT/PSS to Enhance Neuronal Recording and Stimulation. IEEE EMBC 2017. To be presented as a poster. Jeju, Korea. 11 - 15 July 2017.

Agrawe Z, Montgomery J, Travas-Sejdic J, Svirskis D. Macro-porous PEDOT for neuronal interfacing. WBC 2016. Presented as a poster. Montreal, Canada. 17 - 22 May 2016.

Conference Presentations

Agrawe Z, Montgomery J, Travas-Sejdic J, Svirskis D. PEDOT Modified Microelectrodes for Neuronal Recording. Oral Presentation. D4 2016. Dunedin, New Zealand. 23 - 24 November 2016.

Agrawe Z, Montgomery J, Travas-Sejdic J, Svirskis D. PEDOT modified microelectrodes for neuronal recording. Oral Presentation. 11th Polymer Electronics Research Centre Symposium. Auckland, New Zealand. 17 - 18 November 2016.

Agrawe Z, Montgomery J, Travas-Sejdic J, Svirskis D. Macroporous PEDOT for neural interfacing. Oral Presentation. Exposure 2016. Auckland, New Zealand. 03 October 2016.

Agrawe Z, Montgomery J, Travas-Sejdic J, Svirskis D. Macroporous PEDOT for neural interfacing. Oral Presentation. Healthex 2016. Auckland, New Zealand. 16 September 2016.

Agrawe Z, Montgomery J, Travas-Sejdic J, Svirskis D. Conducting polymer coatings for neuronal microelectrode arrays. Oral Presentation. 10th Polymer Electronics Research Centre Symposium. Auckland, New Zealand. 16 - 17 November 2015.

Agrawe Z, Montgomery J, Travas-Sejdic J, Svirskis D. The Interaction Between Neurons and Conducting Polymers. Oral Presentation. Healthex 2014. Auckland, New Zealand. 12 September 2014.

Contents

Abstract	iii
Acknowledgements	vi
Research Outputs Arising from this Thesis	ix
Contents	xii
List of Figures	xv
List of Tables	xviii
List of Abbreviations	xix
List of Symbols	xxi
1 Introduction	2
1.1 Research Motive & Objectives	3
1.2 Thesis Structure	5
2 Literature Review	7
2.1 Introduction	8
2.2 Recording of Neural Activity through MEAs	10
2.2.1 Amplification Systems	11
2.3 Stimulation of Neural Activity through MEAs	12
2.4 Ideal Microelectrode Properties	13
2.4.1 Recording Specific Properties	13
2.4.2 Stimulation Specific Properties	14
2.4.3 Performance Stability	15
2.5 Conducting Polymers as Microelectrode Surface Coatings	17
2.5.1 Reduced Impedance	20
2.5.2 Increased Charge Injection Capability	23
2.5.3 Enhanced Performance Stability	25
2.5.4 Influence on Biocompatibility	29
2.5.4.1 Influence on chronic <i>in-vivo</i> performance	31
2.6 Conclusion	36
3 MEA Fabrication, Coating and Characterisation	37
3.1 Introduction	38
3.2 Aims and Objectives	40
3.3 Methods	41

3.3.1	Chemicals & Materials	41
3.3.2	MEA Fabrication	42
	3.3.2.1 MEA Substrate	42
	3.3.2.2 Patterning of Electrode Tracts and Insulation	43
	3.3.2.3 Fluid-well Construction:	46
3.3.3	Conducting Polymer Deposition	47
	3.3.3.1 Conventional Conducting Polymers	47
	3.3.3.2 Macroporous Conducting Polymers	48
3.3.4	Electrochemical Characterisation	49
	3.3.4.1 Cyclic Voltammetry	50
	3.3.4.2 Voltage transient measurements	50
	3.3.4.3 Electrochemical Impedance Spectroscopy	51
3.3.5	Morphological Characterisation	52
3.3.6	Performance Stability	52
3.3.7	Biocompatibility	53
	3.3.7.1 Primary Hippocampal Neuron Culture	55
	3.3.7.2 <i>In vitro</i> Neurite Outgrowth and Viability Assays	55
3.3.8	Statistical Evaluation	57
3.4	Results and Discussion	58
	3.4.1 MEA Fabrication	58
	3.4.2 Conventional and Macroporous PEDOT/PSS Deposition	61
	3.4.3 Electrochemical characterisation	66
	3.4.3.1 Cyclic Voltammetry	67
	3.4.3.2 Voltage Transient Measurements	72
	3.4.3.3 Electrochemical Impedance Spectroscopy	73
	3.4.3.4 Summary of Electrochemical Results	81
	3.4.4 Morphological characterisation	82
	3.4.5 Performance Stability	85
	3.4.6 Biocompatibility	87
3.5	Conclusions	90
4	MEA Acquisition System	92
	4.1 Introduction	93
	4.1.1 Aims & Objectives	94
	4.2 Methods	96
	4.2.1 Chemicals & Materials	96
	4.2.2 Amplifier Design	97
	4.2.2.1 Power Supply	98
	4.2.2.2 Reference Voltage	98
	4.2.2.3 Amplifier architecture	100
	4.2.3 MEA to amplifier interface	101
	4.2.3.1 Shielding	101
	4.2.4 Acquisition System Design	102
	4.2.4.1 Synchronisation of ADCs	106
	4.2.4.2 Digital I/O	107
	4.2.5 Intrinsic Noise Measurements	108
	4.2.5.1 RMS Noise Assessment	108

4.2.6	Amplifier and Microelectrode Noise Assessment	110
4.2.6.1	Tyrode's Solution	110
4.3	Results	111
4.3.1	Amplifier Performance	111
4.3.2	Modified Amplifier Architecture	115
4.3.3	Modified Interface Board	115
4.3.3.1	Modified Amplifier Performance	118
4.3.4	Acquisition System	121
4.4	Conclusions	124
5	Neuronal Recording & Stimulation	125
5.1	Introduction	126
5.1.1	Aims and Objectives	130
5.2	Methods	131
5.2.1	Chemicals & Materials	131
5.2.2	MEA Set-up	131
5.2.2.1	MEA Device	131
5.2.2.2	Microelectrode Materials	132
5.2.2.3	Data Acquisition	133
5.2.2.4	Primary Hippocampal Neuron Cultures	133
5.2.2.5	Noise Floor Characterisation	134
5.2.2.6	Confirmation of Neuronal Activity	134
5.2.2.7	Neuronal Activity Recording	135
5.2.2.8	Stimulation Efficacy	136
5.3	Results & Discussion	137
5.3.1	<i>In-vitro</i> Microelectrode Noise Characterisation	137
5.3.1.1	Pre-Culture	137
5.3.1.2	Post-Culture	138
5.3.2	Spontaneous Neuronal Recording	141
5.3.2.1	Confirmation of Neuronal Activity	141
5.3.2.2	Signal to Noise Ratio	142
5.3.3	<i>In-vitro</i> Stimulation Efficacy	149
5.4	Conclusions	153
6	Conclusions & Future Outlook	154
6.1	Conclusions	155
6.2	Limitations & Future Directions	158
6.2.1	Low Deposition Charge Density	158
6.2.2	Macroporous PEDOT/PSS Performance Stability	158
6.2.3	Signal to Noise Ratio Metric	159
6.2.4	Stimulation Efficacy	164

List of Figures

1.1	A general outline of the thesis structure which details the type of investigations carried out in each of the experimental chapters.	6
2.1	Simplified schematic of a MEA	9
2.2	SEM images of nanostructured conducting polymers	21
2.3	Impact of <i>in-vivo</i> implantation on $ Z $	32
3.1	Photomasks used for gold and insulation patterning	43
3.2	MEA fabrication process chart	44
3.3	Reaction scheme between amino group and residual epoxy group on SU-8	47
3.4	FCVD setup for the uniform deposition of PS-COOH beads onto MEA devices	48
3.5	A typical charge balanced, biphasic, current waveform utilised for performance stability testing of the CP coatings	53
3.6	Patterned MEA slides with Ti/Au sputtered in-house (NANO 36) or commercially (DRLI) using nLOF as an insulation layer.	58
3.7	Custom multi-electrode array, inset detailing layer properties (not to scale)	59
3.8	CV curve comparing silver epoxy and solder connection methods	60
3.9	The influence of immersing MEA devices into 0.1 M polystyrene sulphonate solution on PS-COOH coating uniformity	62
3.10	FTIR spectra of a SU-8 coated microscope slide (—) and SU-8 coated slide immersed in PSS (- - -).	62
3.11	Current and potential response of conventional and macroporous PEDOT/PSS using potentiostatic and galvanostatic methods . .	63
3.12	The influence of organic solvents on PS-COOH bead removal at different time points	64
3.13	CSC_c and $ Z $ of macroporous PEDOT/PSS polymerised potentiostatically at 127 mC cm^{-2} treated with different solvents. . .	65

3.14	SU-8 collapse observed after 1 hour immersion in DMF	66
3.15	A summary of electrochemical tests for conventional and macroporous PEDOT/PSS polymerised potentiostatically at increasing deposition charge densities	68
3.16	A summary of electrochemical tests for conventional and macroporous PEDOT/PSS polymerised galvanostatically at increasing deposition charge densities	69
3.17	Nyquist plot of EIS data for representative CP electrode coatings illustrating the fit of the RZC model	74
3.18	Predicted thermal noise values of gold, conventional PEDOT/PSS and macroporous PEDOT/PSS polymerised potentiostatically and galvanostatically	78
3.19	SEM images of conventional and macroporous PEDOT/PSS structures potentiostatically polymerised	84
3.20	Performance stability of conventional PEDOT/PSS and macroporous PEDOT/PSS coatings.	86
3.21	Representative composite images of primary hippocampal neurons grown on various substrates for biocompatibility analysis	88
3.22	Bar graph indicating the number of viable cells per cm^{-2} and total neurite length supported on each substrate.	89
4.1	Amplifier schematics for amplification of neuronal signals.	99
4.2	Photographs of the amplifier circuit and MEA to amplifier interface.	102
4.3	Block diagram of the data acquisition program showing 5 loops which operate in parallel.	105
4.4	General architecture of the LabVIEW program.	106
4.5	Block diagram for the synchronisation of two USB 6356 ADC's.	107
4.6	Block diagram for the generation of trigger signals to external devices from the program.	108
4.7	Assessment of intrinsic noise levels of the amplifier.	112
4.8	Assessment of noise levels when the amplifier is connected to gold microelectrodes on the MEA device.	114
4.9	Modified amplifier schematics for amplification of neuronal signals.	116
4.10	Photograph of the modified interface board.	117
4.11	Photograph of the final amplifier set-up.	118
4.12	Assessment of intrinsic noise levels of the modified amplification system.	119

4.13	Assessment of noise levels for modified amplifier when connected to gold microelectrodes on the MEA device through neural interface board version 2.	120
4.14	Front panel of acquisition program	123
5.1	Comparison of stimulating waveforms.	129
5.2	Representative noise spectra for gold, conventional PEDOT/PSS and macroporous PEDOT/PSS coatings pre-culture.	139
5.3	Representative noise spectra for gold, conventional PEDOT/PSS and macroporous PEDOT/PSS coatings post-culture.	140
5.4	Nyquist plots of conventional and macroporous PEDOT/PSS before and 28 days after culture.	142
5.5	Time trace acquired from a conventional PEDOT/PSS modified microelectrode before and after addition of TTX.	143
5.6	Representative time traces of recorded spontaneous activity for unmodified gold, conventional PEDOT/PSS macroporous PEDOT/PSS coated microelectrodes.	144
5.7	Extracted and clustered spikes for unmodified gold, conventional PEDOT/PSS macroporous PEDOT/PSS coated microelectrodes.	145
5.8	Cumulative frequency plot of SNR values for unmodified gold, conventional PEDOT/PSS and macroporous PEDOT/PSS coatings.	149
5.9	Noise recorded from a conventional PEDOT/PSS microelectrode with a voltage stimulator connected in parallel.	151
5.10	Magnitude response of the constructed IIR comb filter.	151
5.11	Stimulus artifact in response to monophasic and biphasic voltage pulses of 100 μ s duration and 1 V amplitude.	152
6.1	Illustration of the set-up used to obtain simultaneous electrical and optical signals from primary hippocampal cells cultured on MEA devices.	160
6.2	An example of combined electrical and optical recordings from a single electrode.	162
6.3	Confirmation of neuronal action potentials following antagonism with tetrodotoxin (TTX) addition.	164

List of Tables

2.1	Surface modifications and their impact on microelectrode electrochemical parameters	18
2.2	Summary of accelerated ageing studies and chronic <i>in-vitro</i> stimulation carried out on CP microelectrodes	27
2.3	Impedance ($ Z $ at 1 kHz) changes following <i>in-vivo</i> implantation of multi-electrode array in animal models	33
3.1	Modelled impedance parameters for both conventional and macroporous PEDOT/PSS polymerised either potenti- or galvanostatically at different deposition charge densities	80
4.1	Amplifier parts list	96
4.2	The calculated % of amplifier noise as compared to microelectrode thermal noise values taken from <i>Chapter 3</i>	111
4.3	The calculated % of the modified amplifier intrinsic noise as compared to microelectrode thermal noise values taken from <i>Chapter 3</i> . The target % value was 45%.	119
4.4	Summary of peak to peak noise values for both amplification systems	121
5.1	Expected and recorded peak-to-peak noise (μV_{p-p}) values of gold, conventional PEDOT/PSS and macroporous PEDOT/PSS pre- and post-culture.	137
5.2	SNR values of unmodified gold, conventional PEDOT/PSS and macroporous PEDOT/PSS with detectable neuronal recordings	147
5.3	Statistical parameters of SNR values for unmodified gold, conventional PEDOT/PSS and macroporous PEDOT/PSS	148

List of Abbreviations

ADC	Analog to Digital Converter
BS	Benzene Sulphonate
CP	Conducting Polymer
CIL	Charge Injection Limit
CNT	Carbon Nanotube
CS	Chondroitin Sulphate
CSC	Charge Storage Capacity
CSC _c	Charge Storage Capacity <i>Cathodic</i>
CV	Cyclic Voltammetry
DAQ	Data Acquisition (Device)
DBS	Dodecyl Benzene Sulphonate
DFT	Discrete Fourier Transform
DIV	Days <i>In-Vitro</i>
DMF	Dimethylformamide
EDOT	3,4-Ethylenedioxythiophene
EEG	Electroencephalography
EF	Enlargement Factor
EIS	Electrochemical Impedance Spectroscopy
fcc	Face-centred cubic
FCVD	Flow Controlled Vertical Deposition
FFT	Fast Fourier Transform
FTIR	Fourier Transform Infrared Spectroscopy
HA	Hyaluronic Acid
HBSS	Hank' Balanced Salt Solution
IrO _x	Iridium Oxide
ITO	Indium Tin Oxide
MEA	Microelectrode Array
NBM	Neural Basal Media
NGF	Nerve Growth Factor

NT-3	Neotrophin-3
PBS	Phosphate Buffered Saline
PC12	Pheochromocytoma 12
PDMS	Poly(Dimethyl Siloxane)
PEDOT	Poly(3,4-ethylenedioxythiophene)
PFI	Programmable Function Interface
PGMEA	Propylene Glycol Monoethyl Ether Acetate
PMAS	Poly(2-methoxyaniline-5-sulphonic acid)
PMMA	Poly(Methyl Methacrylate)
PS-COOH	Carboxyl terminated Polystyrene beads
PSS	Polystyrene Sulphonate
PTH	Printed Through Hole
<i>p</i>TS	<i>para</i>-Toluene Sulphonate
Py	Pyrrrole
QMH	Queued Message Handler
RIE	Reactive Ion Etching
RMS	Root Mean Square
SEM	Scanning Electron Microscopy
SGN	Spiral Ganglion Neuron
SNR	Signal (to) Noise Ratio
TFB	Tetrafluoroborate
TTX	Tetrodotoxin
THF	Tetrahydrofuran
UV	Ultra Violet
VTM	Voltage Transient Measurement

List of Symbols

Symbol	Name	SI Unit
c^*	bulk concentration	mol cm^{-3}
C_D	diffusional pseudocapacitance	F
C_{tot}	total capacitance	F
D	diffusion coefficient	$\text{cm}^2 \text{s}^{-1}$
E_{mc}	maximum cathodic potential	V
f	frequency	Hz
F	Faraday's constant	C mol^{-1}
G	Gain	-
I	current	A
I_a	anodic current	A
I_c	cathodic current	A
k_B	Boltzmann's constant	J K^{-1}
L	diffusion length	m
$Noise_{p-p}$	noise amplitude	V
P_f	pulse frequency	Hz
P_w	pulse width	min
Q_{10}	accelerated ageing factor	-
r	electrochemical radius	m
r_o	original electrochemical radius	m
R_s	solution resistance	Ω
S_{vnm}	thermal noise spectral density	V Hz^{-1}
Sig_{p-p}	signal amplitude	V
SNR	signal to noise ratio	dB
t	time	min
t_{37}	simulated time at 37 °C	min
t_T	time at elevated temperature	min
T	temperature	K
V	potential	V

V_a	access voltage	V
$V_{RMS(ADC)}$	RMS digitiser noise	V
$V_{RMS(amp)}$	RMS intrinsic amplifier noise	V
$V_{RMS(bio)}$	RMS biological noise	V
$V_{RMS(inst)}$	RMS instrumentation noise	V
$V_{RMS(th)}$	RMS thermal noise	V
ΔV	voltage transient	V
$ x $	filtered waveform	V
$ Z $	impedance magnitude	Ω
Z'	real impedance	Ω
Z''	imaginary impedance	Ω
Z_D	Warburg diffusion element	-
ω	angular frequency	rad
ρ	solution resistivity	$\Omega \text{ m}$
σ	solution conductivity	S m^{-1}
σ_n	median standard deviation	-
τ_D	diffusional time constant	min

Dedicated to my family

Chapter 1

Introduction

1.1 Research Motive & Objectives

Microelectrode arrays (MEAs) comprise a multitude of microelectrodes, embedded on a substrate, which are capable of recording from and stimulating electrically active cells, *in-vitro* and *in-vivo* [1–4]. They have become invaluable tools in the extracellular assessment and manipulation of neuronal populations. For recording, local ionic changes associated with neuronal activity are transduced to analog electronic signals at the microelectrode site through capacitive mechanisms. Analog signals are then amplified and digitised for visualisation. MEA recording performance is usually represented as a signal to noise ratio (SNR) and is heavily dependent on the amplitude of the noise floor. Noise can be introduced into the system in three distinct areas, (i) biological noise resulting from background neuronal activity, (ii) instrumentation noise contributed from recording equipment (amplifier and analog to digital converter) and (iii) thermal noise at the microelectrode/electrolyte interface, which increases in proportion to microelectrode impedance. Stimulation is achieved via charge injection through the microelectrode resulting in redistribution of ions surrounding the cell and subsequent neuronal activation as a result of changes in the transmembrane potential. Stimulation efficacy and safety is influenced by microelectrode electrochemical properties, namely, capacitance and impedance. Current research aims to produce stable, small and/or high density MEAs in order to improve recording and/or stimulation selectivity for *in-vitro* and *in-vivo* applications [5–7]. The demand for MEAs with high selectivity places a size restriction on microelectrodes, reducing the effective electrochemical surface area. This negatively impacts recording quality and stimulation efficacy through increased impedance and reduced charge injection properties [8].

Strategies to improve electrochemical surface area whilst maintaining the desired geometric area revolve around the development of rough microelectrodes

and/or microelectrode coatings onto traditional planar microelectrode materials such as gold and platinum [7, 9]. Conducting polymers (CPs) are electroactive materials which have commonly been used with success as microelectrode coatings to increase electrochemical surface area and improve properties central to neuronal recording and stimulation [10–15]. This thesis aims to further improve recording and stimulation properties of CP coatings through the introduction of macropores within the CP structure. **We hypothesise that the macroporous CP coating will further increase electrochemical surface area and subsequently result in an electrode coating with superior recording and stimulation performance.** Furthermore, **we hypothesise that the construction of a low noise amplification system will compliment microelectrode modification strategies in order to produce a low noise, highly sensitive recording setup.** Intrinsic noise of the amplifier is the second largest determinant of recorded noise through MEA systems and strategies to improve this will prove beneficial for recording quality. To investigate these hypotheses the following objectives will be carried out;

1. Construct a MEA comprising an electrode material common to conventional devices, such as gold.
2. Develop reproducible methods for the modification of planar microelectrodes with **conventional** and **macroporous** CP structures.
3. Characterise and compare the microelectrode materials for electrochemical properties central to neuronal recording and stimulation, performance stability, morphology and biocompatibility.
4. Construct an amplification system with a maximum intrinsic noise value of 45% of the predicted microelectrode thermal noise.
5. Analyse recording performance and stimulation efficacy of the microelectrode materials *in-vitro*, alongside primary hippocampal neurons.

1.2 Thesis Structure

The thesis will be structured as follows, refer to *Figure 1.1* for a summary of the experiments undertaken in each chapter.

Chapter 2 reviews the literature on background processes that occur during neural recording and stimulation through MEAs. The application of conducting polymers as electrode coatings to improve recording, stimulation efficacy and chronic electrode stability is also reviewed.

Chapter 3 details the design of an MEA made from gold electrodes and fabrication processes for conventional and macroporous CP coatings. Unmodified gold microelectrodes and CP coatings will be characterised and directly compared for properties relevant to neuronal recording and stimulation such as cathodic charge storage capacity, charge injection limit, impedance, morphology, performance stability, and biocompatibility. The influence of polymerisation method, galvanostatic and potentiostatic, on the electrochemical properties of these microelectrodes will also be addressed. This study sheds new light on how a macroporous CP coating influences electrochemical properties, relevant to neuronal recording and stimulation, compared to a conventional CP coating.

Chapter 4 details the design and development of an amplification and data acquisition system to record neuronal action potentials through the MEA. The amplifier will be characterised for intrinsic noise with a target peak-to-peak noise level of 45% (or less) of the predicted microelectrode thermal noise. This chapter also includes schematics for a LabVIEW based program used to control data acquisition and stimulation through National Instruments hardware.

Chapter 5 investigates recording performance and stimulation efficacy of conventional and macroporous CP coatings, *in-vitro*, alongside primary hippocampal neurons. To achieve this, noise of the system (i.e. MEA connected with the amplification and data acquisition system) will be characterised pre- and

post-culture. The system will then be used to record spontaneous activity of primary hippocampal neurons and a SNR value for uncoated gold and conventional and macroporous CP coatings is then calculated. Stimulation efficacy will be assessed by the number of direct neuronal responses to biologically relevant voltage stimulation pulses through unmodified gold, conventional PEDOT/PSS and macroporous PEDOT/PSS.

Chapter 6 presents the conclusions and recommendations arising from these studies.

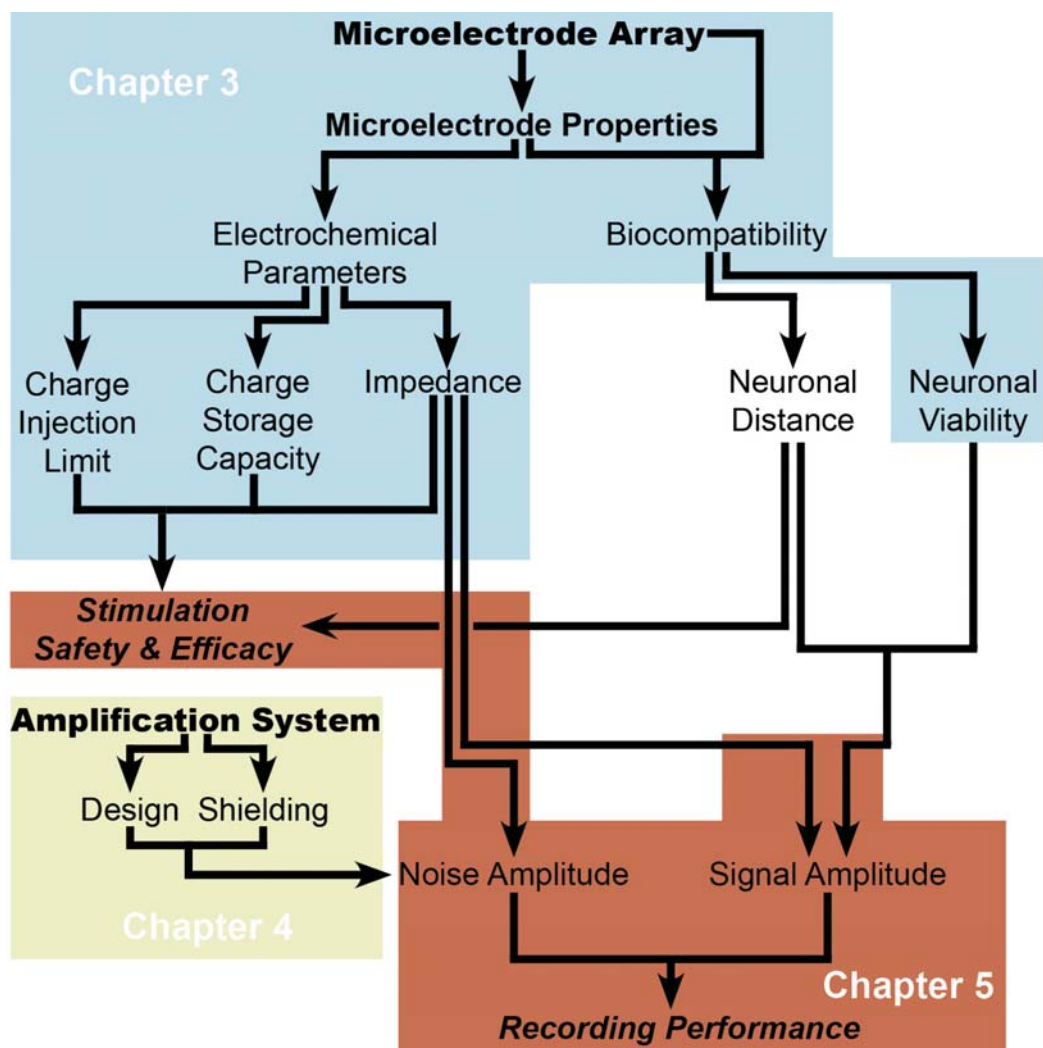


Figure 1.1: A general outline of the thesis structure which details the type of investigations carried out in each of the experimental chapters.

Chapter 2

Reviewing The Influence of Conducting Polymers on Neuronal Microelectrode Array Recording, Stimulation and Performance Stability

2.1 Introduction

The complexity of the nervous system is exemplified by the vast network of neurons and supporting cells, which work synchronously to process external and internal cues that result in movement, emotions, sight, speech and hearing. Understanding the nervous system and disorders associated with it has engaged the interest of scientists in a wide range of disciplines. The electrochemical nature of signalling between neurons is well understood, with many diseases presenting themselves as a fault within the signalling chain [16–18]. Microelectrode arrays (MEAs) were introduced as tools to interface between biological and electronic systems, allowing for monitoring and manipulation of neural circuits that underpin both normal and diseased states [19, 20]. *In-vivo* MEAs have introduced novel treatment strategies to a variety of neural impairments such as deafness [21], blindness [22] and movement disorders [18]. *In-vitro* use of MEA devices has provided insight into the dynamics of neural networks and their response to bioactive substances. MEAs were pioneered by Pine, Thomas and Gross in the 1970's and their early work provided a platform for MEA device fabrication [1–4]. The general architecture of devices (*Figure 2.1*) is comprised of (i) metallic electrodes, which act to transduce ionic signals associated with neuronal firing into an electrical signal (and vice versa) (ii) a substrate onto which the electrode material can be deposited on (commonly glass or silicon) and (iii) an electrically inert insulation layer which defines the size of the electrode.

Current research aims to produce stable, small and/or high density MEAs in order to improve chronic *in-vivo* integration and recording/stimulation selectivity for neural prosthetic applications [5–7]. The demand for high density MEAs places a size restriction on microelectrodes, which reduces both recording quality (reduced signal to noise ratio (SNR)), and stimulation efficacy through high

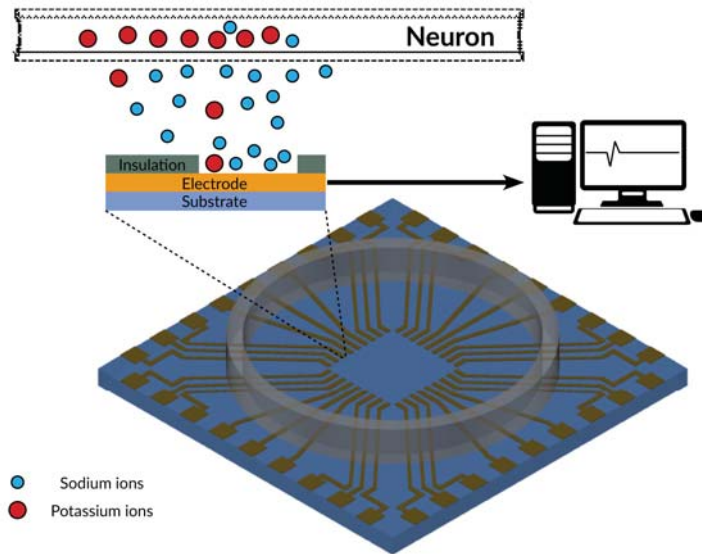


Figure 2.1: Simplified schematic of a single microelectrode component on a MEA. Neuronal action potentials are associated with changes in local ionic concentrations, these can be detected and digitised via microelectrodes embedded on multi-electrode arrays.

impedance and impaired charge injection [8]. Established microelectrode materials such as platinum (Pt) and gold (Au) struggle to meet current demands. Meanwhile, essential research into more compatible materials is ongoing [7, 9]. This chapter provides a background on the processes that occur during neuronal recording and stimulation through MEAs. The application of conducting polymers as electrode coatings to improve recording, stimulation efficacy and performance stability is then discussed.

2.2 Recording of Neural Activity through MEAs

Recording neuronal activity through MEAs can be broken up into three segments to better understand the processes at work, (i) neuronal signal generation, (ii) signal propagation and (iii) signal transduction. In neuronal recordings, electrical signals (i.e. action potentials) are generated by neurons and involve the movement of ions across the cell membrane (mainly sodium and potassium) [23, 24]. This process creates a localised change in ionic concentrations which propagate to an electrode contact throughout an electrolyte, as described by the volume conduction theory (*Equation 2.1*) [25–27].

$$V(x, y, z) = \frac{I}{4\pi\sigma\sqrt{(x - x')^2 + (y - y')^2 + (z - z')^2}} \quad (2.1)$$

Where I is the transmembrane current source (action potential located at x' , y' , z') and V is the potential recorded at an electrode (located at x , y , z) in an infinite volume conductor with homogeneous extracellular electrical conductivity (σ).

From Equation 2.1, it is evident that distance between electrode and the signal source strongly influences the amplitude of signals recorded, therefore electrode materials that promote intimate neuronal interactions are favourable for both *in-vivo* and *in-vitro* MEA devices. Pre-patterned MEA devices can also be designed to guide neurite growth towards electrode contacts for enhanced recording performance *in-vitro* [28–32]. Additionally, conductivity of the media influences the potential recorded, although it is unlikely that conductivity will change within biological systems, this concept is important when extrapolating data from *in-vitro* to *in-vivo* systems due to differences in conductivity between extracellular fluid (ECF), with values in between $0.2 - 0.6 \text{ S cm}^{-1}$, and *in-vitro* test solutions (typically artificial cerebrospinal fluid) [33]. At the

electrode/electrolyte interface, signal transduction of charge carriers from ions in the electrolyte to electrons in the metal occurs [34, 35]. Two primary mechanisms of charge transfer can occur at this interface, faradaic and capacitive (non-faradaic) reactions [6]. Faradaic mechanisms involve the transfer of electrons at the electrode/electrolyte interface and generally occur when charge is applied to an electrode resulting in potentials that exceed the threshold for reduction/oxidation (redox) reactions [6, 34]. Capacitive mechanisms dominate in recording electrodes and involve the redistribution of charged chemical species in the electrolyte creating an electric double layer at the interface [36]. The change in local ionic concentrations associated with neuronal action potentials alters the composition of the electric double layer and ultimately the voltage seen by the microelectrode [36]. The transduced signal is then amplified, filtered and digitized for visualisation on a computer [37].

2.2.1 Amplification Systems

Amplification systems are a key component for neuronal signal acquisition through MEA devices [38]. They serve to amplify weak bioelectronic signals transduced at the microelectrode/electrolyte interface within the range of an analog-to-digital converter which enables visualisation of neural activity on-screen. Stringent low noise requirements are placed on amplifiers intended for neuronal data acquisition due to the small signal amplitudes expected. A general target for intrinsic amplifier noise is 45% that of the noise expected at the microelectrode/electrolyte interface (thermal noise) [37, 39].

The general architecture of neuronal amplification systems comprises (i) a high pass filter at the front-end to remove DC offsets created at the microelectrode/electrolyte interface [39], (ii) a gain of approximately 2000, to amplify neuronal signals which are typically within the range of 50 - 500 μV [40, 41]. This gain

is typically distributed across two amplification stages, with the first stage referred to as the ‘pre-amplifier.’ (iii) A bandwidth of approximately 10 kHz, capable of capturing both action potential related data (300 - 3000 Hz) and local field potentials (1 - 200 Hz) [38,40,42], and (iv) a voltage offset to enable amplification of both negative and positive signals typical of neuronal action potentials [41].

2.3 Stimulation of Neural Activity through MEAs

Neuronal stimulation through MEAs has significant potential to modulate or restore neurological function [43]. Stimulation processes through microelectrodes rely on an inversion of the events that occur for recording. Current-controlled or voltage-controlled charge injection into microelectrodes creates an electric field throughout the electrolyte which can also be modelled by *Equation 2.1* [6,34], where the extracellular potential (V) at a neuron located at (x,y,z) is determined by the current (I) flowing through the electrode at (x',y',z') [34].

Commonly, a biphasic current pulse is used, where the first phase drives the electrode potential negative (cathodic phase) in order to elicit action potential generation, followed by a reversal phase where the electrode is driven to a positive potential (anodic phase). The reversal phase is commonly used to prevent or reduce the incidence of irreversible faradaic reactions [34]. As mentioned above, charge transfer across the electrode/electrolyte interface can either be capacitive or faradaic. Although capacitive mechanisms are preferred faradaic mechanisms can dominate in stimulating electrodes due to the high charge injection requirements for neuronal activation. Faradaic reactions can take the form of reversible redox events or more sinister irreversible corrosion reactions that damage both electrode and neural cells around it [6,34,44]. Irreversible faradaic reactions occur when charge injection causes potential changes large

enough to oxidise or reduce chemical reactants that cannot be reversed within the duration of the applied pulse. An example of such a reaction is the oxidation or reduction of water, which is why most stimulating electrodes are characterised within the redox potentials of water (also referred to as the water potential window) [34].

2.4 Ideal Microelectrode Properties

Due to the key role of electrodes as ion to electron transducers, optimisation of their properties is integral for successful recording and stimulation through MEA systems. Electrode materials common to conventional MEA devices include gold and platinum. Use of these materials is well defined within neural environments however their application to high density MEAs is limited by high impedance, small charge injection capabilities and poor long term performance stability within the neuronal environment [45].

2.4.1 Recording Specific Properties

For neuronal recording, low impedance microelectrodes with high spatial resolution (i.e. the ability to detect single unit activity) are desirable. The reduction of microelectrode size required for improving spatial resolution reduces the total electrochemical surface area which in turn increases impedance [10,26]. Impedance is a measure which is often presented when characterising electrodes for neuronal applications and can be loosely defined as resistance to alternating currents. For neuronal recordings, high impedance degrades signal quality through two mechanisms; noise and shunt loss [11,46]. Noise at the electrode/electrolyte interface can be caused by random fluctuations of charged carriers through Brownian motion of electrons (thermal noise) in the electrode and

drift and diffusion of charged ions due to concentration gradients in the electrolyte [11, 36]. These random movements create current disturbances which increase the voltage noise in proportion to impedance [11]. Other sources of noise include (but are not limited to); instrumentation noise, shot noise, flicker noise and biological noise.

Shunt loss describes the loss of signal from the electrode and measurement system to ground which affects signal amplitude and increases in proportion to impedance [35]. Shunt loss occurs in three distinct areas; (i) capacitive loss from the electrode to the surrounding electrolyte, (ii) loss in the metal wiring between the electrode and measurement system due to inherent electrical resistance and (iii) loss in the measurement system through capacitive mechanisms [11]. Generally, an impedance value higher than 5 M Ω at 1 kHz introduces high levels of noise and shunt loss which makes recording from individual neurons problematic [35]. The trade-off between high spatial resolution and recording quality is the focus of many research groups within the area of MEA devices, with the objective of recording single units with a SNR of 5:1 or greater [43].

2.4.2 Stimulation Specific Properties

Ideal stimulating microelectrodes should be able to operate within a potential window that can effectively stimulate neuronal tissue whilst maintaining irreversible faradaic reactions to a minimum. In order for these conditions to be met an ideal microelectrode should display low impedance, high charge storage capacity (CSC) and high maximum charge injection limits (CIL). Low impedance microelectrodes reduce the charge injection requirements to meet neuronal activation thresholds, which in turn reduces the risk of irreversible faradaic reactions [6, 34, 44, 47]. Alongside impedance, CSC is often used to characterise stimulating microelectrodes. CSC is derived by integrating the current/time curve of a slow potential scan (cyclic voltammetry) and measures

the total amount of charge available for stimulation during the scan [5]. A material with high CSC within a safe potential window (i.e. range that does not initiate irreversible faradaic reactions) is desirable. Although a good indicator of electrode properties, CSC cannot be directly extrapolated to evaluate the fast charge injection requirements for neuronal stimulation as only a fraction of this charge is available during sub-millisecond current or voltage pulses [5, 48]. Charge injection capability looks at the amount of charge a microelectrode can inject into the electrolyte within a time-frame relevant for neural stimulation (100 μs — 1000 μs) [5]. A subset of this parameter is the maximum charge injection limit (CIL) which describes the amount of charge that can be injected without polarising the microelectrode beyond water reduction or oxidation potentials (irreversible faradaic reactions) [43]. Microelectrode stimulation should be operated within charge injection limits to prevent electrode and tissue damage, therefore a high CIL is advantageous for safe and effective systems.

It should also be noted that several factors independent of intrinsic microelectrode properties dictate the incidence of Faradaic reactions such as the charge per pulse, the type of waveform used for stimulation and the frequency of stimulation. These factors must be taken into consideration when designing MEAs for stimulation purposes. The reader is directed to the following reviews for an in-depth description of efficacious and safe stimulation protocols [34, 49].

2.4.3 Performance Stability

Chronic *in-vivo* and *in-vitro* stability of MEA devices is crucial for their use as long term clinical and diagnostic tools [50]. Degradation of recording and stimulation performance from MEA devices can be attributed to a range of factors which have been classed as either biotic (issues related to neural tissue) or abiotic (issues related to the electrode itself). Abiotic factors which contribute to failure revolve around physical changes to the MEA devices such as

damaged insulation, corrosion of electrodes, delamination of surface coatings and changes in surface area post-implantation [4, 51]. Electrodes intended for long term operation should be resistant to corrosion or delamination from the underlying substrate when electrode coatings are concerned. Biotic factors are centred around neuroinflammation, tissue encapsulation and astroglial scarring around the recording electrode site [4]. Biotic factors are hypothesised to occur through the mechanical mismatch between MEA systems and neural tissue, triggering inflammatory responses, which lead to encapsulation of electrodes and subsequent device failure [4, 45, 52]. Long term stability can be improved through the use of softer coatings and flexible substrates, these strategies reduce mechanical mismatch and improve biological integration between electrode and neuron [37]. Coating metallic surfaces with bioactive substances can also be employed to reduce foreign body reactions [53].

2.5 Conducting Polymers as Microelectrode Surface Coatings

To improve microelectrode properties for high-density MEA systems, research has been invested in electrode modification with porous/rough conductive materials such as Pt-black [54], carbon nanotubes (CNTs) [51, 55], iridium oxide (IrOx) [43, 44] and conducting polymers (CPs) [7, 56, 57]. Electrode modification with these materials is commonly employed to increase the effective surface area and therefore lower impedance and improve CSC/CIL; producing recording electrodes with high SNR and more effective stimulating electrodes [6, 8, 12, 37, 48, 58]. IrOx is the most extensively studied electrode coating due to its biocompatibility, low-impedance properties and high CIL. However IrOx is limited in chronic applications due to susceptibility to degradation under chronic aggressive stimulation [44]. CNTs have gained attention as novel electrode coatings due to their improved stability under constant polarisation conditions. Although promising for recording purposes [59], single CNT coatings exhibit a relatively low CIL compared to IrOx (*Table 2.1*) and struggle to meet the charge density requirements of neural prostheses [60]. For the purposes of this thesis, the application of CPs as surface coatings for microelectrodes will be reviewed.

Table 2.1: Surface modifications and their impact on microelectrode electrochemical parameters

Substrate	Surface modification	Electrode impedance @ 1 kHz x Area ($M\Omega \cdot \mu m^{-2}$)	CSC ($mC cm^{-2}$)	CIL ($mC cm^{-2}$)	Deposition charge density ($mC cm^{-2}$)
Bare metals					
Au [29]	—	684	0.4 [13]	0.4 [13]	—
Pt [5]	—	400	0.5-0.35	0.15	—
ITO [47]	—	530	—	—	—
Iridium [61]	—	586	0.1	—	—
Non CP based coatings					
Fe [60]	CNT	—	—	1-1.6	—
Iridium [62]	IrOx	—	—	2-4	—
CP doped with synthetic dopants					
Iridium [61]	PPy/ClO ₄	35	160	—	1440
Iridium [61]	PEDOT/ClO ₄	13.5	240	2.39 [63]	1440
Au [13]	PEDOT/Ionic liquid	6	8.7	1.2	260
Pt [5]	PEDOT/PSS	22	88.4 ¹	3.6	1800
Pt [64]	PEDOT/PSS	—	7	2.3	192
Iridium [9]	PEDOT/TFB	7	—	—	390
Pt [63]	PEDOT/ <i>pTS</i>	—	—	2.1	900
Pt [5]	PEDOT/MWCNT	17	202.9 ¹	8.4	1800
CP doped with biomolecular dopants					
Au [17]	PPy/SLPF	222	—	—	800
Pt [14]	PEDOT/DCDPGYIGSR	45	—	—	—
Au [65]	PPy/PSS/NGF	9	—	—	806
ITO [65]	PPy/Glutamic acid	9.7	—	—	—

Continued on next page

Table 2.1 – continued from previous page

Substrate	Surface modification	Electrode impedance @ 1 kHz x Area ($M\Omega \cdot \mu m^{-2}$)	CSC ($mC cm^{-2}$)	CIL ($mC cm^{-2}$)	Deposition charge density ($mC cm^{-2}$)
Defined CP structures					
Iridium [61]	PPy/ ClO_4 nanotubes	24	184	—	1440
Iridium [61]	PEDOT/ ClO_4 nanotubes	3	392	—	1440
Au [15]	PS templated Microporous PEDOT/ ClO_4	11	—	—	290

CPs are attractive materials for interfacing with neuronal environments as they can reduce impedance [11, 13, 55, 64, 66, 67], improve CSC and CIL [6, 7, 13, 47, 48, 55, 58, 68] and improve long term recording stability [10, 69–72]. CPs are unique in that they are organic polymers that possess electrical activity; attributed to the conjugated structure within their backbone [73–78]. The conjugated backbone provides an orbital system which, upon doping [79], allows charge carriers to move within the CP. The chemical or electrochemical polymerisation processes require the presence of dopants (otherwise known as counter-ions) to facilitate polymer formation [79]. Dopants influence the chemical, electrical and physical properties of CPs allowing them to be tailored for various applications [45, 80, 81]. Several biocompatible conducting polymers including polypyrrole (PPy) and poly(3,4-ethylenedioxythiophene) (PEDOT) have been utilised as electrode coatings for neuronal cell recording [11, 12, 14, 64]. PPy based electrodes are easily polymerised and relatively stable, however they suffer from high susceptibility to redox reactions (including oxygen) or pH interference [82]. Bobacka et al. showed that PEDOT was less sensitive to O_2 , CO_2 and H^+ making it more suitable for use in electrode coatings for biological applications [83]. The stability of PPy and PEDOT electrodes was directly

compared by Yamato et al., they showed that PEDOT/PSS retained 89% of its electrical activity under constant polarisation conditions (400 mV for 16 hours) whereas PPy/PSS only retained 5% of its original electroactivity [84]. Increased stability of PEDOT is thought to arise from the dioxy-substituted structure of EDOT, which prevents nucleophilic attack and is less likely to degrade and release dopants [85].

2.5.1 Reduced Impedance

It should be noted that impedance values are commonly taken at 1 kHz, which is characteristic of neuronal action potential activity [23]. Due to the frequency dependant nature of neuronal signals, full impedance spectra are required to understand the charge transfer processes occurring at the electrode/electrolyte interface across the entire frequency range. For example, local field potentials (low frequency oscillations associated with the summation of dendritic action potentials) are useful for discerning disease states and reside within the 1 — 200 Hz frequency band, whereas extracellular spiking associated with single-unit neuronal firing resides within the 300 — 3000 Hz band [13].

The intrinsic porosity of CP structures allows for a large electrochemical surface area when electrochemically deposited onto microelectrodes, which serves to reduce impedance (*Table 2.1*). The dependency of impedance on total electrochemical surface area, among other parameters, is usually exploited when coating microelectrodes with electroactive materials i.e. the rougher/more porous the coating the lower the impedance [45, 63, 86]. For CPs, important factors that dictate the final morphology and resulting electrical properties of the coating include the type of CP used (PEDOT vs PPy), electrochemical deposition method (potentiostatic vs galvanostatic), the type of dopant used, and the

amount of material deposited. CPs can also be electropolymerised around various templates such as electrospun fibres and polystyrene beads, adding another dimension to surface area control of CP coatings (*Figure 2.2*) [15,61].

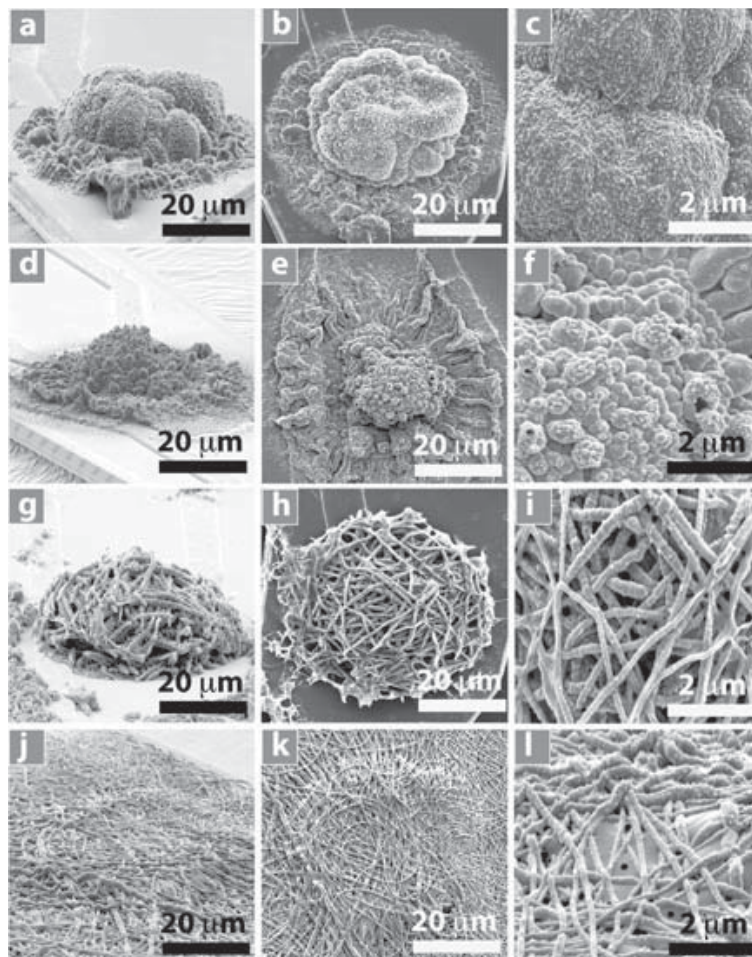


Figure 2.2: SEM image of electropolymerised nanostructured conducting polymers on the electrode sites with deposition charge density of 1.44 C cm^{-2} . Side view: a) PPy film, d) PEDOT film, g) PPy nanotubes, j) PEDOT nanotubes. Top view: b) PPy film, e) PEDOT film, h) PPy nanotubes, k) PEDOT nanotubes. High-magnification top view: c) PPy film, f) PEDOT film, i) PPy nanotubes, l) PEDOT nanotubes. Reproduced with permission from Wiley-VCH Verlag GmbH and Co. KGaA [61]

A comparison between PEDOT doped with sodium *p*-toluenesulfonate (*p*TS), PPy/*p*TS and uncoated iridium electrodes showed that PEDOT/*p*TS had the lowest impedance at 1 kHz, lowest background noise and the highest SNR [12]. Abidian et al. showed that PEDOT structures were able to decrease impedance of bare gold electrodes from $800 \text{ k}\Omega$ to $4 \text{ k}\Omega$, in comparison to PPy which reduced impedance to $80 \text{ k}\Omega$ (all impedance values are taken at 1 kHz) [70]. Another

study by Abidian et al. found a similar trend where PEDOT/ ClO_4 exhibited a lower impedance magnitude at 1 kHz ($10.8 \pm 1.8 \text{ k}\Omega$) than PPy/ ClO_4 ($28.3 \pm 2.6 \text{ k}\Omega$) under the same polymerisation conditions [61].

Cui et al. and Zhou et al. compared galvanostatic and potentiostatic polymerisation of PEDOT/PSS and PEDOT doped with multi-walled carbon nanotubes (MWCNT), respectively [5,64]. A common trend was seen in both studies where galvanostatic polymerisation yielded polymer growth within the constraints of the microelectrode, in contrast to potentiostatic polymerisation, which resulted in outgrowth of polymer structures. Zhou et al. went on to compare the impedance of galvanostatic vs potentiostatic polymerisation methods and showed that galvanostatically polymerised films displayed a lower impedance magnitude at 1 kHz ($2.2 \text{ k}\Omega$ vs. $3.3 \text{ k}\Omega$). Furthermore, galvanostatically polymerised films displayed lower diffusion impedance values (592Ω vs 7004Ω), implying a lower energy barrier of charge transfer in the film bulk [5].

Baek et al. demonstrated a relationship between dopant size and electrical properties, comparing PEDOT doped with lithium perchlorate (ClO_4^-), sodium benzenesulfonate (BS), *p*TS, sodium dodecylbenzene sulphonate (DBS) and poly(styrene sulphonate) (PSS). A trend was seen between dopant size and resulting impedance of the CP structures, with PEDOT/ ClO_4 displaying the lowest impedance magnitude at 1 kHz followed closely by PEDOT/*p*TS, PEDOT/BS, PEDOT/DBS and PEDOT/PSS [45]. This trend can be explained by the resulting morphology of each film, where smaller dopants yield rougher CP structures [45]. Mandal et al. showed a similar trend between dopant size and resulting impedance where PEDOT doped with tetrafluoroborate (BF_4^-) had impedance approximately one order of magnitude lower than PEDOT/PSS electrode coatings at 1 kHz [87].

Multiple research groups have shown a correlation between deposition charge density and resulting impedance [65,66,88]. At lower deposition charge densities

(< 800 mC/cm²) a smooth surface morphology is observed, while at higher charge densities roughness of the film increases, resulting in a ‘hairy’ morphology accompanied by a dramatic decrease in impedance. At charge densities above 4800 mC/cm² impedance starts to decrease due to a reduction in exposed surface area and delamination from the underlying substrate [66].

2.5.2 Increased Charge Injection Capability

In a similar manner to impedance, charge injection capability of an electrode or electrode coating is enhanced when surface area is increased. The porosity of CP microelectrodes and their capability to be polymerised around various templates has been utilised to enhance charge injection properties of conventional metallic electrodes. A review by Cogan has highlighted charge density requirements of neural prostheses intended for various applications, with a threshold charge density ranging from 0.05 mC/cm² to 4 mC/cm² (the amount of charge required to stimulate a neural response in the leading phase of a stimulation pulse) [43]. Most electrodes intended for neuronal applications are characterised by cyclic voltammetry, impedance (discussed above) and voltage transient measurements [43].

Cyclic voltammetry (CV) measurements record the current evolved from a cyclic sweep between two potentials, commonly within the water potential window (approx -0.6 V to 0.8 V vs Ag/AgCl (3M KCl)). CSC, and more commonly, the cathodic CSC (CSC_c) have become common characterisation parameters for stimulating electrodes and are derived from the time integral of the current in a slow-sweep-rate CV. From *Table 2.1*, a dramatic increase in CSC can be seen through the application of CPs as electrode coatings, 0.5 — 0.35 mC/cm² for Pt electrodes compared to 88.4 mC/cm² for PEDOT/PSS. CSC is inversely related to microelectrode impedance and is therefore dictated by the same parameters given in the previous section. As mentioned above, the CSC values are only

an indication of the charge available for stimulation under a slow potential scan (50 — 500 mV/s) and cannot be directly extrapolated to charge transfer occurring during fast charge injection in neuronal environments (sweep rate of approximately 3,000,000 mV/s) [48].

Voltage transient measurements are used to discern the CIL of microelectrodes from a sub-millisecond current or voltage controlled stimulation pulse (details for calculating CIL can be found in [43]). The CIL provides limits above which unwanted irreversible faradaic reactions occur, therefore, target stimulation charge densities should be within these limits [43].

Table 2.1 details CIL values for various CP coatings and illustrates the success of CPs in improving the charge transfer properties of Pt and Au microelectrodes. The rationale for using CP coatings, alongside improving CIL, is to reduce instability issues associated with planar electrodes and well characterised coatings such as IrOx (discussed in the next section) [62]. The requirement of a positive potential bias to achieve high CIL values in IrOx coatings also provides a limitation for use *in-vivo*, although CP coatings benefit from a positive bias, it is not required to achieve high CIL values [43, 62]. Most CP electrode have a charge injection limit between 1 — 3 mC/cm². Zhou et al. demonstrated that the incorporation of CNTs could further improve these values, showing a CIL of 8.4 mC/cm² [5].

2.5.3 Enhanced Performance Stability

Alongside ideal electrochemical characteristics, the fabrication of robust CP coatings is essential for long-term *in-vivo* applications. As with most electrode coatings, CPs can suffer from delamination and fractures with age and under intense stimulation conditions [89]. Studies assessing electrode stability have generally used accelerated ageing techniques to simulate long term ageing of CPs (*Table 2.2*) [5, 48, 63]. Parameters used for accelerated ageing studies typically follow the ASTM international guidelines for polymeric ageing as per *Equation 2.2* [63]. Intensive biologically relevant stimulation regimens are also employed to discern the effect of long term stimulation on CP coatings.

$$t_{37} = t_T \cdot Q10^{\frac{(T-37)}{10}} \quad (2.2)$$

A study by Green et al. demonstrated the importance of dopant choice and underlying surface morphology on CP stability. PEDOT doped with ClO_4^- , *p*TS and PSS on smooth Pt electrodes or laser roughened Pt electrodes were subjected to 89 °C for 3 weeks to simulate 2 years of ageing, CSC measurements were taken pre- and post- ageing. Results indicated that CPs deposited on roughened Pt substrates were less prone to ageing effects (loss of CSC) than CPs on smooth substrates, with the exception of PEDOT/PSS which was equally prone to ageing on both substrates. Furthermore, CPs were subjected to rigorous biologically relevant stimulation conditions in culture media containing proteins. All PEDOT coatings deposited onto smooth Pt failed within 1.3 billion pulses, whereas on roughened Pt substrates, PEDOT/*p*TS and PEDOT/ ClO_4^- were still viable after 1.5 billion pulses [63]. Another study carried out by Venkatraman et al. compared the stability of PEDOT/PSS deposited onto PtIr wires and clinical grade platinum neurostimulation electrodes at 67 °C for 13 weeks (corresponding to 2 years at 37 °C according to

Equation 2.2) [48]. Results from the study indicated a significant deterioration in impedance for PtIr coated electrodes; however, no significant difference in impedance was seen in Pt coated electrodes, reinforcing the importance of the underlying substrate on CP stability. Zhou et al. demonstrated that polymerisation method (galvanostatic vs potentiostatic) also had implications on electrochemical stability of the CP coatings [5]. Galvanostatically polymerised PEDOT/MWCNT and potentiostatically polymerised PEDOT/MWCNT were subjected to 96 hours of biologically relevant biphasic stimulation (1 mC/cm^2) while monitoring the impact on CSC. Results show that galvanostatically polymerised PEDOT/MWCNT suffered a CSC loss of 2.2% whereas potentiostatically polymerised PEDOT/MWCNT suffered a greater CSC loss of 11.4%. Galvanostatically polymerised PEDOT/MWCNT was then subjected to a higher stimulation charge density of 3 mC/cm^2 (clinically relevant in neural prosthesis) and suffered a modest decrease in CSC of 4%.

Table 2.2: Summary of accelerated ageing studies and chronic *in-vitro* stimulation carried out on CP microelectrodes

Substrate	Coating	Accelerated ageing	Stimulation
Smooth Pt [63]	PEDOT/ <i>p</i> TS 900 mC cm ⁻²	89 °C for 3 weeks (2 year sim): 39% loss in CSC	0.15 mC cm ⁻² , 0.2 ms phase ⁻¹ : Failure after 1.4 billion cycles
Rough Pt [63]	PEDOT/ <i>p</i> TS 900 mC cm ⁻²	89 °C for 3 weeks (2 year sim): 20% loss in CSC	0.15 mC cm ⁻² , 0.2 ms phase ⁻¹ : No failure after 1.5 billion cycles
Smooth Pt [63]	PEDOT/ClO ₄ 900 mC cm ⁻²	89 °C for 3 weeks (2 year sim): 65% loss in CSC	0.15 mC cm ⁻² , 0.2 ms phase ⁻¹ : Failure after 1.1 billion cycles
Rough Pt [63]	PEDOT/ClO ₄ 900 mC cm ⁻²	89 °C for 3 weeks (2 year sim): 22% loss in CSC	0.15 mC cm ⁻² , 0.2 ms phase ⁻¹ : No failure after 1.5 billion cycles
Smooth Pt [63]	PEDOT/PSS 900 mC cm ⁻²	89 °C for 3 weeks (2 year sim): 60% loss in CSC	0.15 mC cm ⁻² , 0.2 ms phase ⁻¹ : Failure after 300 million cycles
Rough Pt [63]	PEDOT/PSS 900 mC cm ⁻²	89 °C for 3 weeks (2 year sim): 65% loss in CSC	0.15 mC cm ⁻² , 0.2 ms phase ⁻¹ : Failure after 864 million cycles
Iridium [89]	PEDOT/PSS 3050 mC cm ⁻²	—	5 mC cm ⁻² , 0.2 ms phase ⁻¹ : No sig difference in impedance or CSC after 720,000 pulses

Continued on next page

Table 2.2 – continued from previous page

Substrate	Coating	Accelerated ageing	Stimulation
Iridium [89]	IrOx	—	5 mC cm⁻², 0.2 ms phase⁻¹: 70 kΩ increase in impedance at 1 kHz after 720,000 pulses
PtIr [48]	PEDOT/PSS 19.2 mC cm ⁻²	67 °C for 4 weeks (32 wk sim): 27 kΩ increase in impedance at 1 kHz	3 mC cm⁻², 0.1 ms phase⁻¹: No significant change in impedance or CSC after 24 hr
Pt [55]	PEDOT/CNT 32 mC cm ⁻²	—	0.35 mC cm⁻², at 50 Hz: No significant change in impedance or CSC after 2 weeks
Pt [5]	PEDOT/CNT 1800 mC cm ⁻²	—	3 mC cm⁻², at 50 Hz: 4% loss in CSC after 92 hours
Au [87]	PEDOT/TFB	60 °C for 11 weeks: Large impedance increase at 1 kHz over 75 days, $t_{1/2}$ of 38.7 days at 60 °C	—
Au [87]	PEDOT/PSS	60 °C for 11 weeks: Large impedance increase at 1 kHz over 75 days, $t_{1/2}$ of 3.5 days at 60 °C	—
Au [87]	PEDOT/PSS/ CNT	60 °C for 11 weeks: Large impedance increase at 1 kHz over 75 days, $t_{1/2}$ of 4.5 days at 60 °C	—

2.5.4 Influence on Biocompatibility

It is well reported that CP structures (namely, PEDOT and PPy based CPs) can support the growth of neuronal cells [45, 81, 90, 91]. In an effort to further improve biocompatibility, the incorporation of biomolecules as dopants into CP films has been studied as a means to further reduce distance between neuronal cells and the electrode – yielding enhanced recording and more efficient stimulation [72]. A common concern regarding CPs doped with biomolecules is their electrical and structural instability; therefore, these properties will also be discussed in this section.

Green et al. doped PEDOT with two different laminin peptide sequences, DED-EDYFQRYLI and DCDPGYIGSR, and made comparisons with PEDOT/*p*TS and bare platinum microelectrodes [14]. Results from this study indicated that PEDOT/ DEDEDYFQRYLI and PEDOT/ DCDPGYIGSR coatings were approximately five units softer than PEDOT/*p*TS. Impedance analysis of the films showed that all PEDOT coatings effectively reduced impedance magnitude at 1 kHz recorded from Pt by approximately 80%. Adhesion tests revealed that PEDOT doped with laminin peptides had poor adhesion with a 10% coating loss, compared to PEDOT/*p*TS with a 0.52% coating loss. Poor adhesion of laminin doped PEDOT was attributed to the larger size of laminin peptide dopants, which affected polymer attachment to the underlying Pt substrate. Electroactivity studies were in favour of PEDOT/*p*TS, which suffered reduced loss in CSC over 400 cycles compared to PEDOT/ DEDEDYFQRYLI and PEDOT/ DCDPGYIGS (11.99% loss compared to 18.77% and 16.84% loss, respectively). *In-vitro* cell data using pheochromocytoma (PC12) cells revealed that PEDOT/*p*TS facilitated higher cell density with 15,000 cell/cm² compared to 7,500 cells/cm² and 10,000 cells/cm² for PEDOT/ DEDEDYFQRYLI and PEDOT/ DCDPGYIGS, respectively. Coating the surface of all PEDOT

films with laminin increased the cell density of PEDOT/*p*TS, PEDOT/ DED-EDYFQRYLI and PEDOT/ DCDPGYIGS to around the same level (15,000 — 19,000 cells/cm²). Although the laminin peptide dopants did not behave as expected in terms of supporting neuronal growth, this study highlights an important point of post-processing CP coatings with laminin rather than incorporating it into CP structures [14]. Cui et al. also performed comparisons between PEDOT/ DCDPGYIGSR and PEDOT/PSS. Although they did not compare impedance and electroactivity of the two coatings, comparisons in bioactivity and acute *in-vivo* recording were made. Glial cells were cultured onto PEDOT/ DCDPGYIGSR and PEDOT/PSS microelectrodes. Sites which contained DCDPGYIGSR facilitated glial attachment with 1.9 cells attached compared to 0.2 cells for PEDOT/PSS. Acute *in-vivo* recordings compared PEDOT/ DCDPGYIGSR to bare gold electrodes, higher signal amplitudes and a lower amplitude noise floor was noticed for PEDOT/ DCDPGYIGSR. Although results from this study show support for peptide doped PEDOT, a more robust analysis of biocompatibility is needed to draw a clear conclusion between PEDOT/PSS and PEDOT/ DCDPGYIGSR [64].

Thompson et al. investigated how the entrapment and release of neuro-trophin-3 (NT-3) from PPy influenced growth and survival of spiral ganglion neurons (SGN) [91]. The study also investigated how different dopants; *p*TS, DBS, PSS, poly-(2-methoxyaniline-5-sulphonic acid) (PMAS), hyaluronic acid (HA) and chondroitin sulphate (CS), influenced biocompatibility and entrapment and release of NT-3. Primary studies without the incorporation of NT-3 revealed that PPy/*p*TS and PPy/DBS facilitated neurite extension from SGN explants, as well as longer neurite extension, outperforming the other dopants and study controls. The biological dopants, HA and CS, were not as biocompatible as DBS and *p*TS suggesting that overall physical and chemical properties of the polymer influence biocompatibility rather than dopant nature alone. It also was noticed

that DBS and *p*Ts dopants produced rougher films than HA and CS suggesting that resulting polymer morphology plays an important role in neurite adhesion and extension [91]. Furthermore, PPy/*p*TS was able to effectively encapsulate and release NT-3 from its structure, yielding a higher number of neurites per explant when compared to PPy/*p*TS alone [91]. Kim et al. investigated nerve growth factor (NGF) incorporation into PPy films and assessed effects on rat PC-12 cells [65]. PC-12 cells are a widely used cell-based model for indicating the presence of NGF, which causes subsequent differentiation and neurite extension upon exposure. Impedance analysis revealed that PPy/NGF films successfully reduced impedance by two orders of magnitude from uncoated gold controls. PPy/NGF also showed a higher level of PC-12 differentiation than PPy controls, indicating the successful release of NGF from the polymer matrix [65]. The reader is guided to the following reviews for further information on biofunctionalisation of CPs [92,93].

2.5.4.1 Influence on chronic *in-vivo* performance

The success of MEAs *in-vivo* is dictated by their ability to function within the neural environment without electrode damage or overt inflammatory reactions. As discussed above, biotic factors that lead to device failure are centred around inflammatory processes that arise due to mechanical mismatch between the device and neural tissue. However, abiotic factors such as delamination of coatings or electrode dissolution must also be considered when discussing CPs for chronic *in-vivo* application. The use of CPs is justified by their intrinsically soft nature which has been theorised to reduce mechanical mismatch between neural tissue and the electrode surface, ultimately reducing *in-vivo* encapsulation of electrodes [45]. Their ability to lower electrode impedance following implantation (*Figure 2.3*) and be doped with various biomolecules can also improve integration between neural tissue and MEA devices, resulting in improved

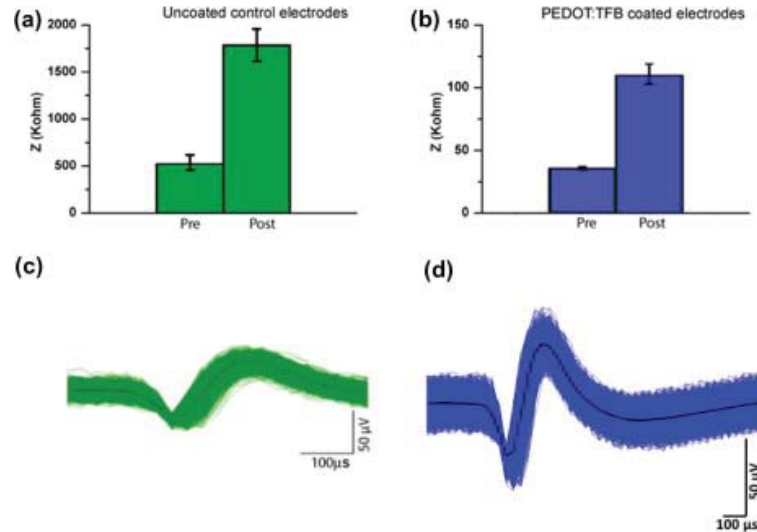


Figure 2.3: The comparison of impedance modulus of the control Au (a) and PEDOT:TFB coated (b) electrode sites before and 2 days post implantation at 1 kHz. Data are from three chronic probes implanted in three rats. Each probe contains 16 electrode sites in total. Reproduced with permission from Elsevier [87].

recording from *in-vivo* environments.

Chronic studies utilising CP electrode coatings are limited, however similar trends are noticeable across all papers (*Table 2.3*). Charkhkar et al. compared chronic intracortical neural recordings between bare gold and PEDOT/ tetrafluoroborate (TFB) modified microelectrodes. Impedance and unit recordings (at least 30 spikes within 10 minutes and a SNR greater than 2) were used as markers to assess electrode viability after in-vivo implantation [9]. An increase in impedance post insertion was noticed for both gold and PEDOT/ TFB electrodes; however, impedance values for PEDOT/TFB were consistently lower. An initial increase in impedance can be attributed to the acute brain-tissue response which lasts up to 2 weeks, as suggested by Ludwig et al. [88]. PEDOT/TFB microelectrodes exhibited higher unit recordings with greater SNR, but only for the first 4 weeks [9].

Table 2.3: Impedance ($|Z|$ at 1 kHz) changes following *in-vivo* implantation of multi-electrode array in animal models

Electrode	Location of implant	Pre implant ($M\Omega \cdot \mu m^2$)	Week 1 ($M\Omega \cdot \mu m^2$)	Week 2 ($M\Omega \cdot \mu m^2$)	Final ($M\Omega \cdot \mu m^2$)	Length of study
Iridium [88]	Motor cortex	689	1195	1195	1055	6 Weeks
Au [71]	Barrel cortex	1051	1525	1416	1225	7 Weeks
PEDOT/poly (oxyethylene) ₁₀ -oleyl ether [88]	Motor cortex	91.4	773	773	569	6 Weeks
PEDOT/ ClO ₄ nanotubes [71]	Barrel cortex	21.3	663	636	651	7 Weeks
PEDOT/ TFB [9]	Motor cortex	7.96	25.3	216	216	11 Weeks
PEDOT/ CNT [94]	Visual cortex	22.6	225	250	625	22 Weeks
PEDOT/PSS [94]	Visual cortex	24.3	350	363	486	12 Weeks

Ludwig et al. compared bare iridium microelectrodes with PEDOT (doped with tetraethylammonium perchlorate) coated microelectrodes over 6 weeks to assess chronic *in-vivo* recording performance [88]. The silicon based neural probes were implanted into Sprague-Dawley rats for 6 weeks where daily impedance and neural recordings were taken to assess electrode viability. A similar 3-phase trend to implantable MEAs was noticed for both coated and uncoated probes where an initial acute inflammatory response, early reactive response and sustained immune response occurred [9,88]. Throughout all phases PEDOT coated electrodes had significantly lower impedance values and higher SNR than non-coated iridium electrodes. PEDOT coated electrodes also recorded more quality units and had more active sites than the iridium controls [88].

A similar study carried out by Abidian et al. compared bare gold microelectrodes with and without PEDOT/ ClO_4 nanotube coatings on silicon-based probes. This study assessed *in-vivo* performance over 7 weeks with comparisons made in impedance at 1 kHz and % of active high quality recording sites (SNR >4). PEDOT coated electrodes out-performed uncoated electrodes in respect to impedance and percentage of sites recording high quality signals over the 7 week test period [71].

Kozai et al. compared the recording performance of PEDOT/PSS and PEDOT/CNT microelectrodes, investigating the effect of dopant choice on *in-vivo* recording performance [94]. Results from this study showed that PEDOT/CNT coated electrodes were able to record quality units on all electrode sites throughout the 22 week period. PEDOT/PSS was also able to record quality units but this degraded rapidly after the first week of implantation. It is important to note that although impedance magnitude at 1 kHz increased for both electrodes, PEDOT/CNT did not experience a significant decline in recording performance. This may be explained by better tissue integration of PEDOT/CNT coatings due to their nano-fibrous structure [94].

Although CP coated electrodes are softer than metallic electrodes such as Pt and Au, the average indentation modulus is still significantly higher than that of neural tissue [45]. The use of softer substrates, such as hydrogels, offers an alternative for CP interfacing with neuronal tissue [95,96]. Kim et al. fabricated hydrogel-coated microelectrodes and found that a hydrogel thickness of 100 μm had no noticeable effect on impedance of the electrodes. Despite electrochemical advantages, swelling of the hydrogel matrix *in-vivo* resulted in increased distance between electrode and neurons, resulting in low signal detection from active neurons [97]. For in-depth reviews on the application of hydrogels to MEA devices, the reader is directed to [7,98].

Another approach to improve longevity of CP based MEA devices involves the incorporation of anti-inflammatory molecules, such as dexamethasone (dex), as dopants in the CP structure [99–103]. CP/dex structures have the capacity to actively and passively release therapeutic concentrations (6 — 30 $\mu\text{g}/\text{cm}^2$ based on a 15 μm diameter microelectrode) of dex and have been shown to alleviate cellular reactive responses such as astrocyte growth [100,102]. A study carried out by Kolarcik et al. compared *in vivo* responses to PEDOT/CNT and PEDOT/CNT/dex coatings to assess the influence of dex on inflammation. Although no significant difference was seen in the kill zone radius, PEDOT/CNT/dex electrodes demonstrated lower neuronal cell death than the PEDOT/CNT coatings (14.1% versus 19.7%) [104].

2.6 Conclusion

MEAs have gained popularity both *in-vivo* and *in-vitro* as diagnostic tools and a means for novel treatment strategies to reverse neural impairments. The success of electrode modification with rough conductive materials has been extensively demonstrated and has opened the path towards smaller/high density MEA systems. CPs have made their mark within this field and have demonstrated the ability to improve electrical parameters central to MEA recording and stimulation, such as reducing impedance and improving CSC/CIL.

CPs have demonstrated their versatility through the ability to incorporate various biological dopants, improving biocompatibility and cellular interactions with the microelectrode coating. As well as, various synthetic dopants, such as PSS and TFB, which display favourable electrochemical properties. Although long-term stability of CP coatings is still of concern, the body of literature surrounding this field has demonstrated novel strategies to improve this parameter, such as laser roughening of the underlying substrate or use of IrO_x adhesion layers.

Although the search for an electronically and physically stable microelectrode goes on, CPs have demonstrated new avenues and approaches which can address this issue. It goes without saying that a collaborative approach across disciplines is pivotal in creating an ideal electrode coating with optimal biocompatibility, electrochemistry and stability.

Chapter 3

The Fabrication and Characterisation of *In-vitro* Microelectrode Arrays Modified with Macroporous Conducting Polymers

3.1 Introduction

The trend towards smaller microelectrodes for high density microelectrode arrays (MEAs) with improved selectivity has triggered research into novel electrode coatings capable of improving deleterious effects caused by reduced electrochemical surface area [10, 11, 46]. The literature (*Chapter 2*) has demonstrated the ability of CPs to improve electrochemical properties associated with neuronal recording and stimulation, allowing for the fabrication of small, selective microelectrodes. Deposition of CPs onto conventional, planar, microelectrodes is accompanied by an increase in electrochemical surface area as a result of their inherent nodular surface morphology [65, 66, 88]. This increase in surface area results in reduced impedance and increased charge storage properties [10–15].

In an effort to further increase electrochemical surface area, yielding more favourable recording and stimulation properties, this chapter details the fabrication of a modified CP structure termed macroporous CP. The macroporous CP structure is fabricated through electrochemical deposition of a CP around a sacrificial bead template with a diameter of 230 nm. Note, the term macroporous polymer is defined as a polymer with pore size between 50 and 1000 nm [105]. Removal of the template following deposition yields a highly porous, open structure which is theorised to significantly improve the electrochemical surface area. Macroporous CPs have previously been documented in works by Martin et al. [15], termed ‘microporous’ modification in their study rather than ‘macroporous’ used here. The detailed macroporous CPs were polymerised around a polystyrene bead template which was deposited on the microelectrode using sedimentation. The resulting structures were then characterised for impedance, charge storage capacity and stability over 120 CV cycles, however no direct comparisons to conventional CP structures were made to illicit the effects of macropores on electrochemical properties.

In the work presented here we optimise ordered template deposition into the microelectrode cavities using flow controlled vertical deposition [106] rather than sedimentation. The electrochemistry of fabricated macroporous structures will be directly compared to conventional CPs polymerised under the same conditions, to understand whether the increase in porosity is attributed to improved impedance, charge storage/injection properties and stability. Stability analysis will be carried out through application of biologically relevant stimulation pulses rather than slow scan CV cycling. We also detail biocompatibility analysis of the macroporous structure which, to our knowledge, has not been done previously.

Polymerisation and characterisation of both conventional and macroporous CPs were informed by the literature highlighted in *Chapter 2*. 3,4-Ethylene dioxythiophene (EDOT) was selected as the CP to be used due to superior electrochemical stability [84] and significant improvements in properties central to neuronal recording and stimulation, as compared to pyrrole (Py) based polymers [12, 61, 70]. Polystyrene sulphonate (PSS) was chosen as the dopant for CP structures due to well documented biological and electrochemical properties [5, 64]. Both potentiostatic and galvanostatic polymerisation were trialled and compared as several groups claimed deposition method influenced electrochemical properties [5, 64]. The influence of polymer thickness, as controlled by deposition charge density, on electrochemical properties was also investigated in an effort to select ideal polymerisation conditions for the CP coatings trialled.

3.2 Aims and Objectives

In this chapter, we aim to fabricate MEA devices with either conventional or macroporous poly(3,4-ethylenedioxythiophene) doped with PSS (PEDOT/PSS). The macroporous system is hypothesised to further increase the effective electrochemical surface area of conventional electropolymerised CP structures. Here we present in-depth characterisation data, relevant to neuronal recording and stimulation, which aims to investigate the morphology, cathodic charge storage capacity (CSC_c), performance stability, impedance, charge injection limit (CIL) and biocompatibility of macroporous PEDOT/PSS — with a direct comparison to conventional PEDOT/PSS coatings and planar gold microelectrodes. The influence of polymerisation method, galvanostatic or potentiostatic, on the electrochemical properties of these polymers will also be addressed. This data sheds new light on how a macroporous CP coating influences electrochemical properties, relevant to neuronal recording and stimulation, and biocompatibility compared to a conventional CP coating. The specific objectives were to:

1. Design and construct a customised MEA intended for *in-vitro* neuronal recording and stimulation. The MEA should facilitate microelectrode modification with conventional and macroporous PEDOT/PSS and allow for the culture of primary hippocampal cells.
2. Detail reproducible methods for the modification of gold microelectrodes embedded on the MEA, with conventional and macroporous PEDOT/PSS at four different deposition charge densities, using both potentiostatic and galvanostatic electrochemical polymerisation.
3. Characterise uncoated gold, conventional PEDOT/PSS and macroporous PEDOT/PSS (polymerised galvanostatically and potentiostatically) at four different deposition charge densities for CSC_c , impedance, CIL, morphology, performance stability and biocompatibility.

3.3 Methods

3.3.1 Chemicals & Materials

Cyclopentanone, dimethylformamide (DMF), ethanol, 3,4-ethylenedioxythione (EDOT), hydrochloric acid (HCl), iodine (I₂), phosphate buffered saline (PBS), poly-D-lysine, potassium ferricyanide, potassium ferrocyanide, potassium iodide (KI), propylene glycol monomethyl ether acetate (PGMEA), sodium polystyrene sulphonate (PSS), tetrahydrofuran (THF) and toluene were all purchased from Sigma Aldrich (Australia) and used as received.

Hanks balanced salt solution (HBSS), minimum essential medium (MEM) and neural basal media (NBM) were all purchased from Gibco (USA). NBM was supplemented with B27 prior to use. Papain was purchased from Worthington (USA) and used as received. Fetal bovine serum was purchased from Moregate Biotech (Australia) and used as received. The Neurite Outgrowth Staining kit, comprising neurite outgrowth indicator, cell viability indicator and background suppression dye, was purchased from Molecular Probes (USA).

Acetone and isopropanol were purchased from ECP Limited (New Zealand) and used as received. Decon 90 detergent was purchased from Decon Laboratories Limited (UK) and diluted to 10% for cleaning. nLOF 2070 negative photoresist and AZ 326-MIF developer were purchased from Microchemicals (Germany) and used as received. SU-8 2075 negative photoresist was purchased from MicroChem (USA) and diluted with cyclopentanone to yield SU-8 2005.

Conductive silver epoxy (8331) and solder paste (Sn63NC254) were purchased from MG Chemicals (Canada) and ChemTools (Australia), respectively. A poly(dimethyl siloxane) (PDMS) elastomer kit (SLYGARD 184) was purchased from Dow Corning (USA) and used as received. Medical grade silicone adhesive (4100 RTV) was purchased from Bluestar Silicones (Norway) and used as

received.

Water used in the preparation of polymers and buffers was obtained by reverse osmosis (18 M Ω) (MilliQ unit, Millipore, USA) of demineralised water.

3.3.2 MEA Fabrication

Customised MEA devices were designed for *in-vitro* neuronal recording. The MEAs consisted of a glass substrate with 14 individually addressable gold electrode tracts and an SU-8 insulating layer. The insulating layer defined the size of the microelectrodes at a diameter of 20 μm .

3.3.2.1 MEA Substrate

Glass microscope slides (2.5 mm x 76.2 mm x 1.1 mm) were chosen as substrate materials for the MEA devices. Uncoated microscope slides were purchased and coated with titanium (40 nm) and gold (100 nm) in-house using a NANO 36 metal deposition system (Kurt J. Lesker, USA). The microscope slides were cleaned prior to metal deposition using a three step process; (i) detergent (Decon 90) was used to remove oil films and most large surface contaminants, (ii) acetone and isopropanol were used to further degrease the glass substrate followed by drying with N₂ gas, (iii) Piranha solution (30% H₂O₂:96% H₂SO₄ at a ratio of 3:7) was used for 24 hours to remove remaining organic contamination.

Commercially prepared gold coated microscope slides were also purchased from Deposition Research Laboratories Inc. (DRLI, USA) and used as controls for the slides prepared in-house. The slides ordered also had a 40 nm titanium adhesion layer and 100 nm of gold on a clear glass microscope slide.

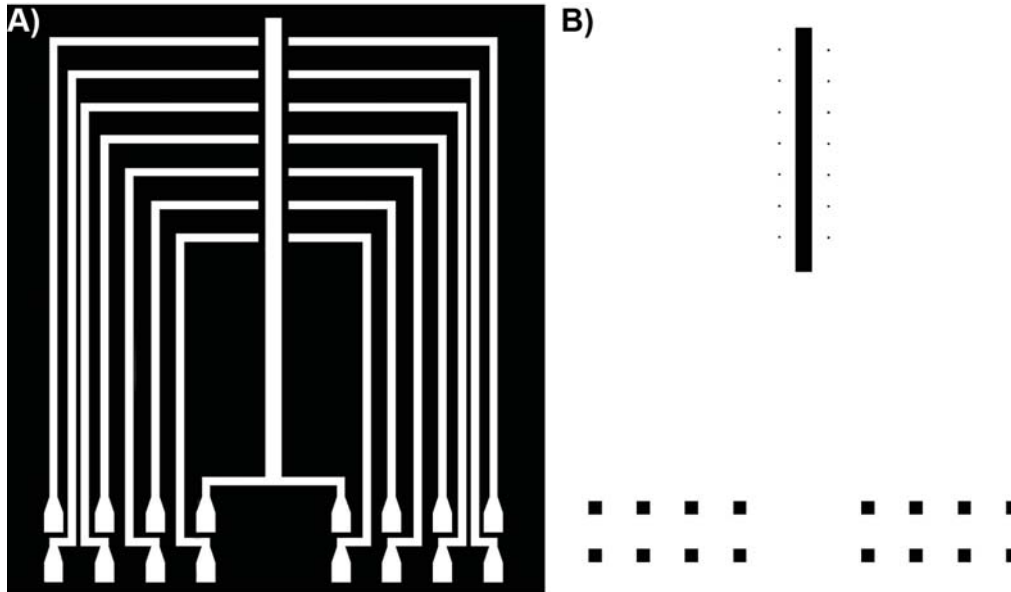


Figure 3.1: Photomasks used for A) gold patterning and B) insulation patterning. Black regions indicate areas of no UV light penetration to the underlying substrate.

3.3.2.2 Patterning of Electrode Tracts and Insulation

Photolithographic techniques were employed to achieve precise patterning of titanium/gold (Ti/Au) coated slides. Photolithography uses ultraviolet (UV) light to transfer a specific pattern from a photomask to a UV-sensitive chemical (photoresist) on the substrate. Customised chrome photomasks were designed via AutoCAD and made using femtosecond pulsed laser machining techniques (*Figure 3.1*).

Electrode patterning: Wet metal etching processes were used to pattern Ti/Au coated slides, as desired (*Figure 3.2*). nLOF 2070 negative photoresist was used as the metal etch mask, it was spun onto gold slides (Laurell WS-400B-6NPP/LITE spin coater, USA) at 500 rpm for 10 seconds, followed by 2500 rpm for 30 seconds (acceleration was 300 rpm s^{-1} for both steps) – yielding a $7 \mu\text{m}$ thick coating. Slides were then pre-baked at $110 \text{ }^\circ\text{C}$ for 1 minute to reduce solvent content and improve nLOF adhesion to the substrate [107]. The slides were left to rest for 5 minutes followed by UV exposure for 14 seconds at 11

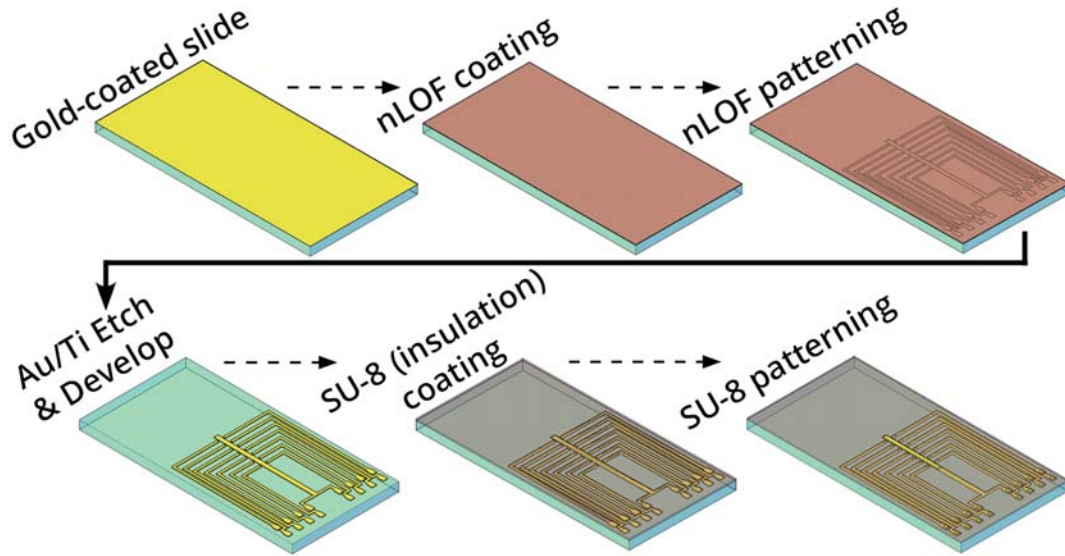


Figure 3.2: Processes involved in MEA fabrication. Samples were coated with nLOF, exposed to UV using a photomask followed by photoresist development and Au/Ti etching. SU-8 was then spun onto slides and patterned resulting in exposed gold sites at the connection pads, central counter electrode and $14 \times 20 \mu\text{m}$ micro-electrodes.

mW cm^{-2} (ABM Mask Aligner, USA) to initiate resist cross-linking — the photomask illustrated in *Figure 3.1A* was used for selective exposure of UV in a pre-designed pattern (UV light only penetrated through white regions). Post exposure bake at $110 \text{ }^\circ\text{C}$ for 1 minute was carried out to further facilitate cross-linking initiated during exposure [107]. The nLOF coating was then developed in AZ 326-MIF for approximately 90 seconds to ensure complete removal of unexposed (non cross-linked) photoresist. Gold etching was achieved by placing the slides in an aqueous solution of KI (1.4 M) and I_2 (0.3 M) for 30 seconds. Titanium was then etched by placing slides in 50% HCl heated to $65 \text{ }^\circ\text{C}$. Finally, the cross-linked nLOF was removed using acetone followed by isopropanol to yield the bare gold pattern.

Insulation: The insulating layer served to cover all areas of the MEA except for the connection pads, central gold counter electrode and 20 μm diameter spots on the working electrodes (as shown in *Figures 3.1B and 3.2*). Two photoresists were trialled as insulating layer materials, nLOF 2070 and SU-8 2005. nLOF processing was similar to that described above for gold patterning, however there was no final acetone/isopropanol wash. SU-8 patterning followed the same sequence of steps as nLOF; SU-8 2005 was spun onto the patterned Ti/Au glass slides at 500 rpm for 10 seconds, then 2900 rpm for 30 seconds (acceleration of 300 rpm s^{-1} both steps). The slides were soft baked at 95 $^{\circ}\text{C}$ for 2 minutes and left to cool for 5 minutes before further processing. Using the mask aligner, the insulating layer was aligned on top of the patterned slides and then exposed to UV light for 10 seconds at 11 mW cm^{-2} . Post baking was done at 95 $^{\circ}\text{C}$ for 3 minutes followed by development in PGMEA for 45 seconds. The slides were then rinsed with isopropanol and dried with N_2 .

Electrical Connections: Standard PCB pins were used to connect with gold pads on the MEA devices. The pins were secured onto the slides using a custom 2 mm thick poly(methyl methacrylate) (PMMA) housing unit which was cut precisely using a CO_2 laser (Universal Laser Systems, USA). The PMMA unit had double sided tape (467-200 MP, 3M) fixed to one side which allowed for firm attachment to the glass substrate. Holes in the PMMA housing unit, which lined up with connection pads on the substrate, were filled with conductive silver epoxy and the PCB pins were then inserted into these holes. The conductive epoxy was cured at 65 $^{\circ}\text{C}$ for 2 hours and left overnight at room temperature for use the following day.

The PCB pins were also directly soldered onto the connection pads using solder paste; this was done to compare electrical conduction and electrochemistry through the two connection mechanisms.

3.3.2.3 Fluid-well Construction:

In order for cells to be cultured within the confinement of the MEA devices, a small well had to be designed and fixed onto the slide. Two approaches were trialled for this purpose.

First, a design was created using CAD software (CorelDraw) and printed from a 4 mm thick PMMA sheet using a CO₂ laser. The backing of one side of the PMMA sheet was replaced with double sided tape (3M 467-200 MP, USA) so that the well could be securely connected to the underlying slide. Secondly, PDMS was used as a substitute to PMMA. PDMS base was mixed with the curing agent at a ratio of 10:1, and poured into a mould made from PMMA which was printed using a CO₂ laser and assembled. The resulting PDMS structure took on the same rectangular shape as the first PMMA structure. PDMS was then secured onto the slide using two methods;

1. Reactive ion etching (RIE) (March CS-1701, USA) was used to covalently link PDMS to the SU-8 insulating layer using a method adapted from [108]. The chamber was first purged with N₂ gas for 15 minutes and then PDMS structures were placed, face up, into the chamber. The chamber was then filled with N₂ gas at 100% pore opening and left until the pressure stabilised (approximately 1150 mTorr). PDMS structures were treated with N₂ plasma for 4 minutes, generating amino groups on the PDMS surface. The PDMS structure was then aligned onto the SU-8 surface and heated at 130 °C for 30 minutes to facilitate the reaction between the newly introduced amino groups on the PDMS and residual epoxy groups present in the SU-8 structure (*Figure 3.3*).
2. A medical grade silicone adhesive was used to bond the PDMS structure to the underlying device. The adhesive was left at room temperature for a minimum of 12 hours to allow for curing.

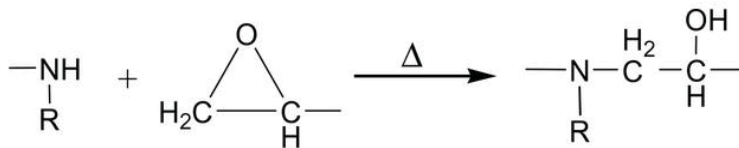


Figure 3.3: Reaction scheme between amino group and residual epoxy group on SU-8

3.3.3 Conducting Polymer Deposition

3.3.3.1 Conventional Conducting Polymers

EDOT, 0.01 M, was added to an aqueous solution of 0.1 M PSS and stirred vigorously for one hour; the mixture was then purged with N_2 for 20 minutes. Conducting polymers were deposited onto 20 μm diameter gold working electrodes using electrochemical polymerisation (Biologic VSP-300, France). A conventional three electrode setup consisting of an aqueous silver/silver chloride (Ag/AgCl) reference electrode, gold counter electrode (central electrode embedded on the device) and gold working electrode (microelectrodes on device) was used for the polymerisation procedure. CPs were deposited using either constant current (galvanostatic) or constant potential (potentiostatic) techniques. For galvanostatic polymerisation a current density of 2 mA cm^{-2} was applied to the microelectrodes (area = $3.14 \times 10^{-6} \text{ cm}^2$) for 4 different time points to yield total polymerisation charge values of 100 nC, 400 nC, 1000 nC and 2000 nC. Generally a current density of 0.5 to 1 mA cm^{-2} is used for galvanostatic polymerisation of PEDOT/PSS, with higher current densities degrading the stability of the coating. We found that for our set up, a current density of 2 mA cm^{-2} was suitable and there were no adverse effects in terms of coating stability or hydrolytic reactions noticed. Potentiostatic polymerisation involved an applied potential of 0.9 V to the working electrode until the total charge passed reached 100 nC, 400 nC, 1000 nC and 2000 nC - equating to 32, 127, 318 and 637 mC cm^{-2} , respectively. The resulting polymer films were immersed in 0.1

M PBS for 24 hours before further characterisation.

3.3.3.2 Macroporous Conducting Polymers

To fabricate high fidelity macroporous structures, carboxyl terminated polystyrene (PS-COOH) (diameter 230 nm) beads were used as a sacrificial template. PS-COOH beads were synthesised using an emulsifier-free emulsion polymerisation technique [109, 110] and deposited onto the modified gold slides using flow-controlled vertical deposition (FCVD) [106]. The PS-COOH suspension was sonicated for one hour prior to use for deposition. *Figure 3.4* illustrates the set-up used to deposit PS-COOH spheres onto the MEA, the PS-COOH suspension was placed into a beaker and the slide was carefully immersed at 70° to the base of the beaker. The PS-COOH suspension was then slowly pumped out at a rate of 1 mL min^{-1} using a peristaltic tubing pump (ISMATEC, Germany) (suspension surface area was 143 cm^2). PS-COOH beads were deposited on the surface of the MEA as the meniscus moved down the slide.

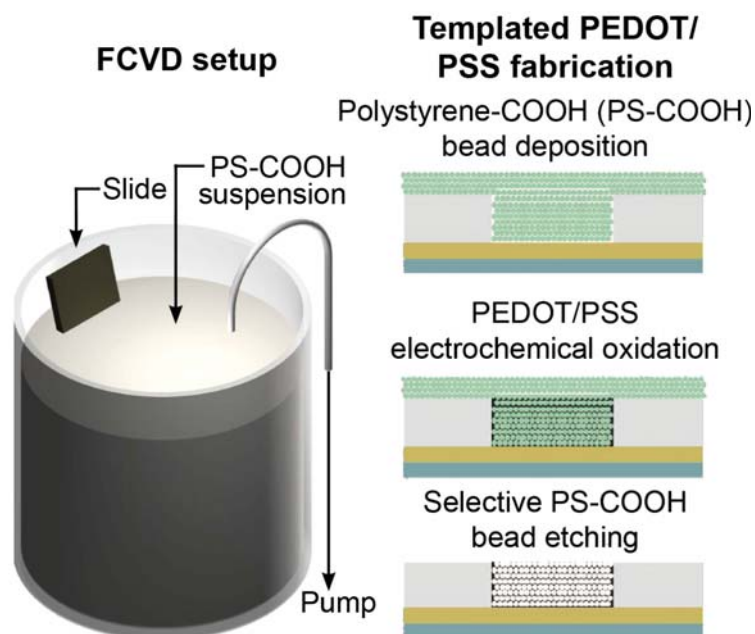


Figure 3.4: FCVD setup for the uniform deposition of PS-COOH beads onto MEA devices. Simplified schematic on the right illustrates the steps involved in the macroporous PEDOT/PSS fabrication.

The slide was left to air dry for 12 hours at room temperature, followed by curing at 95 °C for 3 hours. The CPs were polymerised around the PS-COOH template using galvanostatic and potentiostatic methods described above for conventional conducting polymer films. To selectively etch the template following polymerisation and form a highly porous CP network, three different solvents were trialled: (i) THF for 24 and 48 hours, (ii) DMF for 30 minutes and 1 hour and (iii) a mixture of toluene and acetone (1:3 v/v) for 24 hours.

The effect of different solvents on CP morphology and electrochemical parameters (CSC_c and impedance modulus ($|Z|$) at 1 kHz) was taken into consideration when selecting a suitable solvent.

3.3.4 Electrochemical Characterisation

Macroporous CP microelectrodes were compared against conventional CPs and gold microelectrodes to determine how the macroporous structure influences electrochemical properties. The influence of polymerisation method, i.e. galvanostatic vs potentiostatic, on electrochemical properties of the CP coatings was also investigated. The microelectrodes were characterised for CSC_c and effective electrochemical radius using cyclic voltammetry (CV), CIL using voltage transient measurements (VTM) and impedance using electrochemical impedance spectroscopy (EIS). CV, VTM and EIS measurements were performed using a conventional three electrode setup with a VSP-300 electrochemical workstation. The microelectrode to be tested was used as the working electrode, an embedded central gold electrode on the MEA was used as the counter electrode and an Ag/AgCl electrode served as the reference electrode.

3.3.4.1 Cyclic Voltammetry

To estimate CSC_c in physiologically relevant media and theoretically calculate the microelectrode electrochemical surface area, CV scans were carried out in both 0.1 M PBS and 5 mM ferri-ferrocyanide, respectively. Potential limits for PBS CV scans were set within the water window at -0.9 V and 0.6 V with a scan rate of 100 mV s⁻¹ [43]. CSC_c was defined as the time integral of the cathodic current. CVs carried out in the ferri-ferrocyanide couple were scanned between 0 V and 0.4 V at 100 mV s⁻¹ and the rate limiting anodic current was used to calculate the effective radius of the microelectrode sample under test. For both methods, microelectrodes were cycled twice in the respective media and the third cycle was used for analysis.

3.3.4.2 Voltage transient measurements

VTM was carried out in 0.1 M PBS to mimic physiologically relevant media. A cathodic first, biphasic, charge balanced rectangular current pulse of 1 ms phase⁻¹, and a frequency of 50 Hz was applied. Cathodic first pulsing followed by an anodic reversal phase is commonly used to reduce the incidence of irreversible faradaic reactions [34]. The current density was increased until the measured voltage drop at the electrode/electrolyte interface, termed maximum cathodic potential (E_{mc}), reached the water window at a value of -0.9 V vs Ag/AgCl. E_{mc} is made up of several elements and can be calculated by subtracting the access voltage (V_a) from the voltage transient observed in response to the cathodic current pulse (ΔV). V_a is defined as the voltage change at the onset of the current pulse and describes the ohmic voltage drop across the electrolyte [8, 43].

3.3.4.3 Electrochemical Impedance Spectroscopy

Impedance measurements were performed in 0.1 M PBS to mimic physiologically relevant media. A sinusoidal excitation signal of 10 mV in a frequency range of 1 Hz — 10 kHz was applied and measurements were taken at 9 points per decade (in a logarithmic scale). Impedance magnitude ($|Z|$) was first analysed and represented using a bode plot to obtain an overall understanding on the influence of electrode coatings. In-depth analysis was then carried out by fitting an equivalent circuit to the Nyquist plot enabling quantification of microelectrode and solution properties within the 1 Hz to 10 kHz bandwidth. An equivalent circuit proposed by Bobacka et al. [111] demonstrated good fit with our results ($\chi^2 \approx 0.02$) and was used to study capacitance, charge transfer and ion diffusion processes of the macroporous and conventional PEDOT films. The model incorporates a solution resistance (R_s), finite-length Warburg diffusion element (Z_D) – which is characterised by a diffusional time constant (τ_D) and diffusional pseudocapacitance (C_D) – and capacitance (C_d). Finally, impedance data was used to estimate thermal noise to gain an appreciation of how impedance spectra predict microelectrode recording performance. Real impedance values at each frequency ($Z'(f)$) were used to calculate the power spectral density ($S_{v_n v_n}$) of thermal noise according to *Equation 3.1*. Where T is temperature in Kelvin and k_B is Boltzmann's constant (1.38×10^{-23} J K⁻¹) [112].

$$S_{v_n v_n}(f) = 4k_B T [Z'(f)] \quad (3.1)$$

The root mean square (RMS) thermal noise ($V_{RMS(th)}$) value within our frequency range of interest ($f_1=10$ kHz, $f_2=1$ Hz) was then calculated through integration of the power spectral density as described in *Equation 3.2*

$$V_{RMS(th)} = \sqrt{\int_{f_1}^{f_2} S_{v_n v_n}(f) df} \quad (3.2)$$

Thermal noise was represented as a peak-to-peak noise value, within a 99.99% confidence interval, through multiplication of the resulting $V_{RMS(th)}$ value by 6.6.

3.3.5 Morphological Characterisation

Relevant CP structures were characterised for morphology using scanning electron microscopy (SEM); samples were coated with a thin layer of platinum then imaged with a scanning electron microscope (Philips XL30 S-FEG, Netherlands). The secondary electron detector was utilised at an accelerating voltage of 5.0 kV and a spot size of 2.

3.3.6 Performance Stability

To assess stability under biologically relevant stimulation conditions the CP coatings were subjected to 2.31 million charge balanced, biphasic, current pulses continuously using a VSP-300 electrochemical workstation. A three electrode setup was used as described above and stimulation was carried out in 0.1 M PBS. Stimulation conditions comprised a charge density of 3 mC cm^{-2} with a phase width (P_w) of 1 ms and a pulse frequency (P_f) of 50 Hz (*Figure 3.5*).

The total cathodic (I_c) and anodic (I_a) currents injected equate to $9.42 \mu\text{A phase}^{-1}$ based on a microelectrode diameter of $20 \mu\text{m}$. A charge density of 3 mC cm^{-2} is at the higher end of threshold requirements for neuronal activation [43] and was selected to assess CP coatings under rigorous conditions. The VSP-300 was programmed to perform EIS at 13 intervals during the stimulation experiment (at pulse number 15×10^3 , 30×10^3 , 60×10^3 , 90×10^3 , 120×10^3 , 150×10^3 , 510×10^3 , 870×10^3 , 1230×10^3 , 1590×10^3 , 1950×10^3 and 2310×10^3) to monitor impedance and indicate whether coating delamination had occurred. Delamination was noticed to occur when the % change in impedance magnitude

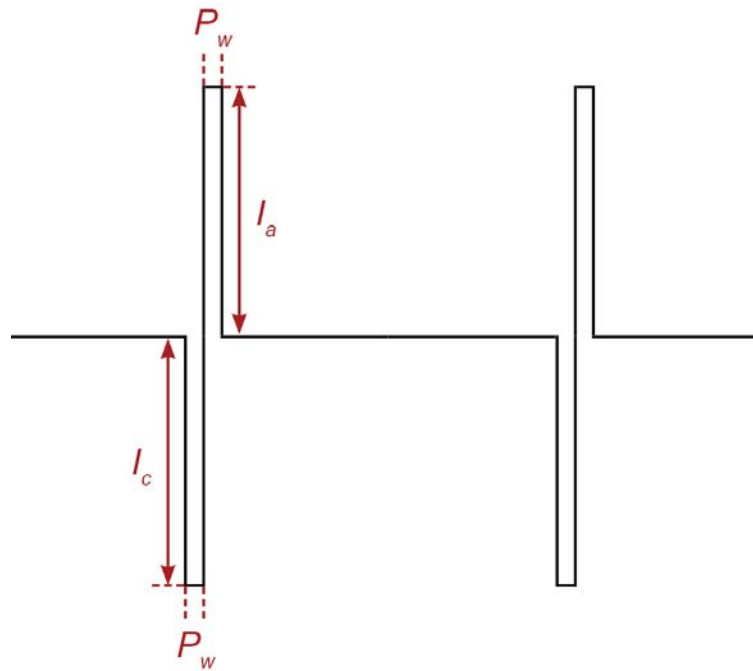


Figure 3.5: A typical current pulse waveform utilised for performance stability testing of the CP coatings. Cathodic (I_c) and anodic (I_a) currents of $9.42 \mu\text{A}$ were used with a phase width (P_w) of 1 ms. The pulse frequency (P_f) was set at 50 Hz meaning a pulse occurred every 20 ms.

at 100 Hz ($|Z|_{100\text{Hz}}$) exceeded 100% and this metric was used to indicate coating failure.

3.3.7 Biocompatibility

Primary hippocampal neurons were cultured for 16 days on the MEA devices to assess biocompatibility of the system. As the MEA devices comprised a number of components, biocompatibility assessment on each of these components was carried out. The substrates used in this study comprised:

1. **Positive control:** A coverslip routinely used for neuronal culture was utilised as a positive control.
2. **MEA:** MEAs detailed above were used. The MEA was cut down to 4 cm^2 using a diamond scribe.
3. **Gold:** A 4 cm^2 gold coated glass slide (DRLI).

4. **Conventional PEDOT/PSS (PEDOT/PSS (C))** was electrodeposited potentiostatically onto a 4 cm² gold coated glass slide (DRLI) at a deposition charge density of 127 mC cm⁻².
5. **Macroporous PEDOT/PSS (PEDOT/PSS (MP))** was electrodeposited potentiostatically over a PS-COOH bead template on a 4 cm² gold coated glass slide (DRLI) at a deposition charge density of 127 mC cm⁻². The template was selectively etched in DMF for 30 minutes.
6. **SU-8**: A 4 cm² clear glass slide was coated with SU-8 using identical parameters for MEA insulation fabrication. SU-8 2005 was spun on at 500 rpm for 10 seconds, then 2900 rpm for 30 seconds (acceleration of 300 rpm s⁻¹ both steps). Soft baking was performed at 95 °C for 2 minutes followed by exposure to UV light for 10 seconds at 11 mW cm⁻². Post exposure baking was performed at 95 °C for 3 minutes followed by development in PGMEA for 45 seconds. The slides were then rinsed with isopropanol and dried with N₂.

Following preparation, each substrate was placed in an individual 35 mm well of a 6-well plate (Thermo Scientific, USA), containing 3 mL MilliQ water, for 24 hours — the water was replaced 3 times during this period. This process was necessary to leach out aqueous contaminants on the surface, introduced during microfabrication and polymerisation processes. MilliQ water was then replaced with 100% ethanol on the day of culture to leach out organic contaminants and sterilise the substrates.

3.3.7.1 Primary Hippocampal Neuron Culture

Primary hippocampal neurons from Wistar rats were cultured at postnatal day zero using established techniques [113,114]. The substrates were transferred to a new, sterile, 6-well plate and washed with 100% ethanol three times, followed by exposure to UV light for 1 hour.

The substrates were then coated with poly-D-lysine ($10 \mu\text{g mL}^{-1}$ in 0.1 M PBS) and left overnight at 37 °C. Wistar pups were decapitated and hippocampi removed and placed in sterilised ice cold Hanks' Balanced Salt solution (HBSS) buffer. The hippocampal neurons were enzymatically dissociated with papain in 5 mL HBSS and incubated at 37 °C for 15 minutes. Enzyme inactivation solution (4.5 mL Minimum Essential Medium + 0.5 mL Fetal Bovine Serum) was added to the neurons after removal of papain to stop the dissociation process. Neurons were then titrated with Neural Basal Media (NBM) until a homogenous cell mixture was formed. The resulting cell suspension was plated onto the substrates at a density of 50,000 cells cm^{-2} . The substrates were then placed in a 5% CO_2 incubator (ThermoFisher Scientific, USA) at 37 °C for 16 days. Half the NBM was replaced at days *in-vitro* 1 (DIV 1) and a quarter replaced at DIV 7 and 14.

3.3.7.2 *In vitro* Neurite Outgrowth and Viability Assays

Viability of the cultured neurons was tested using a Neurite Outgrowth Staining Kit. The kit allows for simultaneous fluorescent analysis of both (i) neuronal viability by means of a cell-permeable viability indicator dye which is converted by live cells to emit green fluorescence and (ii) neurite outgrowth which is monitored via a bright orange-red staining of outer cell membrane surfaces, enabling tracing and measurement of neurite length.

Live-cell staining was carried out at DIV 16. The kit comprised stock solutions of cell viability indicator and cell membrane stain dyes at a concentration of 1000x, and a background suppression dye at 100x. A 1x working stain solution was prepared by diluting 12 μL of the stock dye solutions into 12 mL HBSS containing magnesium and calcium (14025-076, Thermo Fisher). The working stain solution was incubated at 37 °C for 20 minutes prior to use. Cultures were removed from the incubator at DIV 16 and culture media was replaced with 2 mL working stain solution. The stain immersed cultures were then incubated at 37 °C for 20 minutes. Following staining incubation the working stain solution was removed and cultures were washed with 0.1 M PBS twice. A 1x background suppression dye was prepared by a 100-fold dilution of the stock solution in HBSS containing magnesium and calcium. Three mL of the suppression dye was added to each sample prior to imaging.

Images were obtained using a DM RXA2 (Leica, Germany) microscope, fitted with a DS-Fi2 (Nikon, Japan) colour camera using a 10x water immersion objective. I3 and N21 filter cubes were used to visualise the cell viability indicator and cell membrane stain, respectively. All acquisition settings were identical across the samples imaged with binning applied at 2x2 and sensor gain at 2. Exposure of 60 ms was used for the cell viability indicator and 20 ms for the cell membrane stain.

Cell Viability Analysis The presence of green fluorescence within the cell body indicated neuronal viability. Data are presented as the number of viable cells per cm^{-2} on each substrate. Viable cells were counted manually within the calibrated acquired image (area = 0.006 cm^2) using the ImageJ cell counter plug-in.

Neurite Outgrowth Analysis Individual neurites were traced and the calibrated length was calculated using ImageJ (NIH), with Neurite Tracer plugin. Neurites lengths were traced from the tip to the junctions between the cell body and neurite base [115]. Neurites were included in the analysis when the length of the projection exceeded a single body length of the cell from which it extended. [116].

3.3.8 Statistical Evaluation

For electrochemical and stability characterisation the respective tests were performed on three individually prepared microelectrodes polymerised under the same parameters, yielding triplicates for each parameter tested (i.e. 3x conventional PEDOT/PSS polymerised potentiostatically at 318 mC cm^{-2}). For biocompatibility studies, each substrate type was assessed on three different culture days resulting in biological triplicates.

Results were reported as a mean \pm standard deviation. Statistical significance was determined by a p value which was calculated through a paired, two-tailed t-test. A maximum p value of 0.05 was used to indicate significance.

3.4 Results and Discussion

3.4.1 MEA Fabrication

MEA substrates consisted of clear borosilicate glass coated with a titanium adhesion layer (40 nm) and gold (100 nm) coating. Metallic coating processes were either done in-house (using NANO 36 metal deposition system) or commercially (purchased from Deposition Research Lab Inc). *Figure 3.6* shows that commercial deposition of Ti/Au produced higher quality metallic coatings which were resistant to peeling. The tendency for in-house coated films to delaminate may be due to inadequate cleaning processes, leading to poor adhesion of the overlying metallic coating to the substrate. Although films were thoroughly cleaned with detergent, organic solvents (isopropanol and acetone) followed by 24-hour immersion in piranha solution, a further cleaning step using oxygen plasma may have produced more favourable results. Commercial coating of glass substrates was chosen as the preferred method due to the reproducibility and stability of the resulting metallic coating.

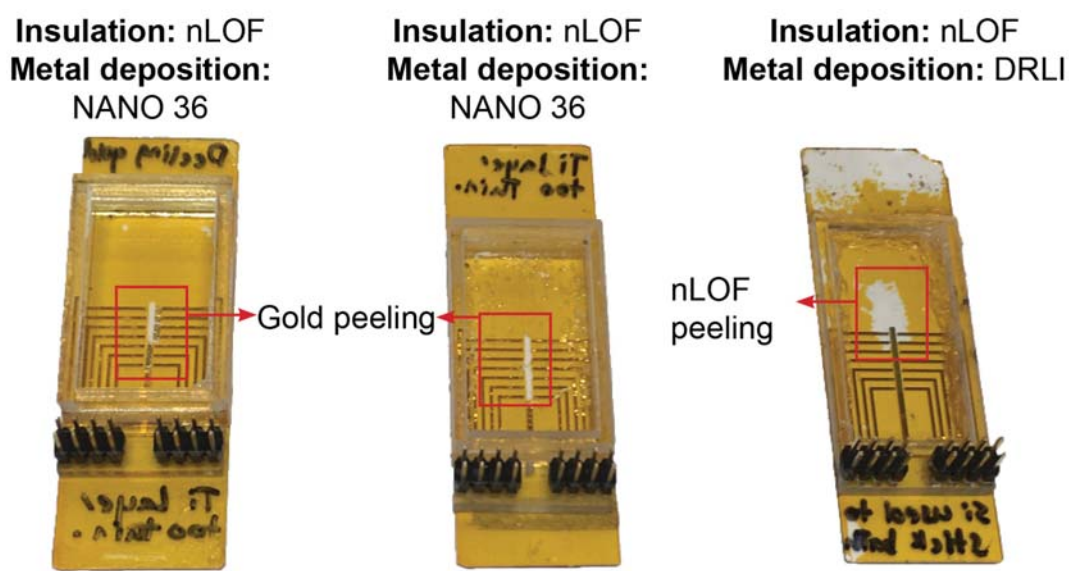


Figure 3.6: Patterned MEA slides with Ti/Au sputtered in-house (NANO 36) or commercially (DRLI) using nLOF as an insulation layer.

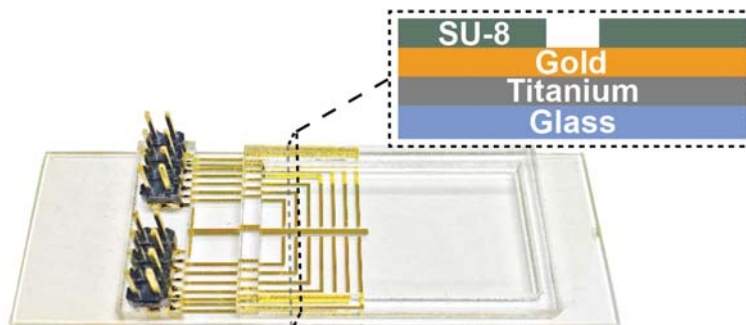


Figure 3.7: Custom multi-electrode array, inset detailing layer properties (not to scale)

Metallic coatings were successfully patterned using conventional photolithographic techniques (*Figure 3.7*). Wet metal etching protocols using I_2/KI and HCl successfully removed gold and titanium layers, respectively. Two photoresists were trialled as an insulating layer for the MEA devices. nLOF produced a yellow coating which could be easily removed with organic solvents; this would be problematic due to the need for sterilisation of these devices with ethanol prior to cell culture. *Figure 3.6* shows nLOF peeling in areas after exposure to ethanol. SU-8 produced a clear, permanent, insoluble film on the surface of the slide (*Figure 3.7*) which was better suited for use as an insulation layer on the MEA devices.

Two methods were used to form electrical connections between PCB pins and gold pads on the MEA devices; (i) pins were securely fastened using a PMMA mount and conductive silver epoxy and (ii) pins were soldered onto the pads using solder paste.

Both methods produced mechanically stable connections, note that the soldered pins were mechanically stable without the need for PMMA mount support. CV curves (*Figure 3.8*) showed redox peaks occurring within the same potential ranges for both methods; however, the solder method displayed a slightly larger area within the curve. This could be attributed to the lower electrical resistivity of solder ($1.45 \times 10^{-5} \Omega \cdot \text{cm}$) vs conductive epoxy ($6 \times 10^{-3} \Omega \cdot \text{cm}$). Note that this curve was swept from 0.8 V to -0.6 V vs $Ag/AgCl$ — this was done at

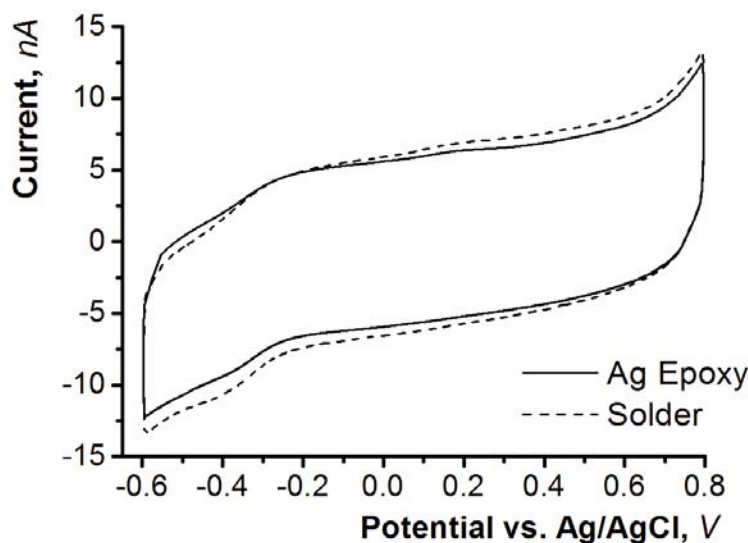


Figure 3.8: CV curve of PEDOT/PSS polymerised at 318 mC cm^{-2} . Solid black curve illustrates PCB pins connected via silver epoxy whereas dashed black curve illustrates PCB pins connected using solder paste.

an early experimental stage and CV sweeps were standardised at 0.6 V to -0.9 V vs Ag/AgCl after this. The silver epoxy method failed mechanically when exposed to organic solvents, such as DMF or ethanol (common solvents used for macroporous CP synthesis and sterilisation), due to weakening of the double sided tape holding the PMMA mount. The solder method showed no difference in mechanical strength when exposed to organic solvents and was selected to form connections between PCB pins and gold pads for later experiments.

In order to contain test media and cultured cells around the area of electrodes, a well had to be constructed. The two materials trialled were PMMA with double sided tape and PDMS which was sealed onto the slide using nitrogen plasma activation (*Figure 3.3*) or medical grade silicone. PMMA wells were only suitable for work not requiring the use of organic solvents, such as electrochemistry in aqueous solutions. The use of PDMS (either RIE or silicone bound) was suitable for all scenarios due to its stability in organic and aqueous solvents. PDMS was also ideal for cell culture work due to its biocompatibility [117], which was maintained with both methods of adhesion.

3.4.2 Conventional and Macroporous PEDOT/PSS Deposition

PS-COOH Deposition: A method for depositing PS-COOH beads into microelectrode cavities was developed in order to fabricate macroporous CP structures. The optimisation of parameters was essential in achieving reproducible coating of MEAs with the PS-COOH bead template. Two parameters critical to the success of coating these MEA devices were; (i) sonication of PS-COOH suspension prior to deposition, this would serve to reduce aggregates and ultimately improve coating uniformity, (ii) immersion of MEA into a surfactant solution, such as 0.1 M PSS, prior to deposition. It was hypothesised that this improved hydrophilicity of the underlying SU-8 coating and in turn promoted bead adhesion (*Figure 3.9*). FTIR analysis of the slides with and without immersion in PSS displayed slight spectral differences (*Figure 3.10*). A wide peak was observed around 3500 cm^{-1} after immersion which is likely attributed to a hydroxyl group from the PSS structure [118, 119]. This indicates surface modification of the underlying SU-8 through adsorption and is the likely cause of improved coating of the hydrophilic PS-COOH beads. The pump rate of 1 mL min^{-1} and curing temperature of $95\text{ }^{\circ}\text{C}$ were used and worked well for PS-COOH bead deposition on the MEAs.

Electrochemical Deposition of PEDOT/PSS Both conventional and macroporous PEDOT/PSS were selectively deposited on the microelectrodes using galvanostatic and potentiostatic electrochemical polymerisation. The resulting polymers appeared as black opaque coatings on the exposed microelectrodes when observed under a light microscope.

During potentiostatic polymerisation the current evolved gradually increased for both conventional (*Figure 3.11A*) and macroporous (*Figure 3.11B*) CP coatings as time progressed. The final current was similar for both coating methods

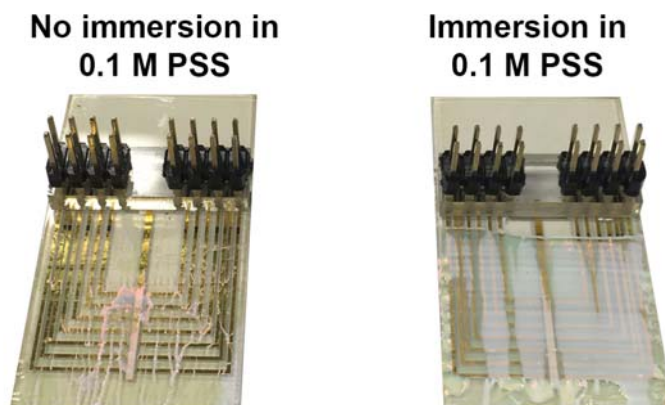


Figure 3.9: The influence of immersing MEA devices into 0.1 M polystyrene sulphonate solution on PS-COOH coating uniformity. No immersion resulted in 'streaky' deposition of PS-COOH beads, whereas immersion resulted in a more uniform layer

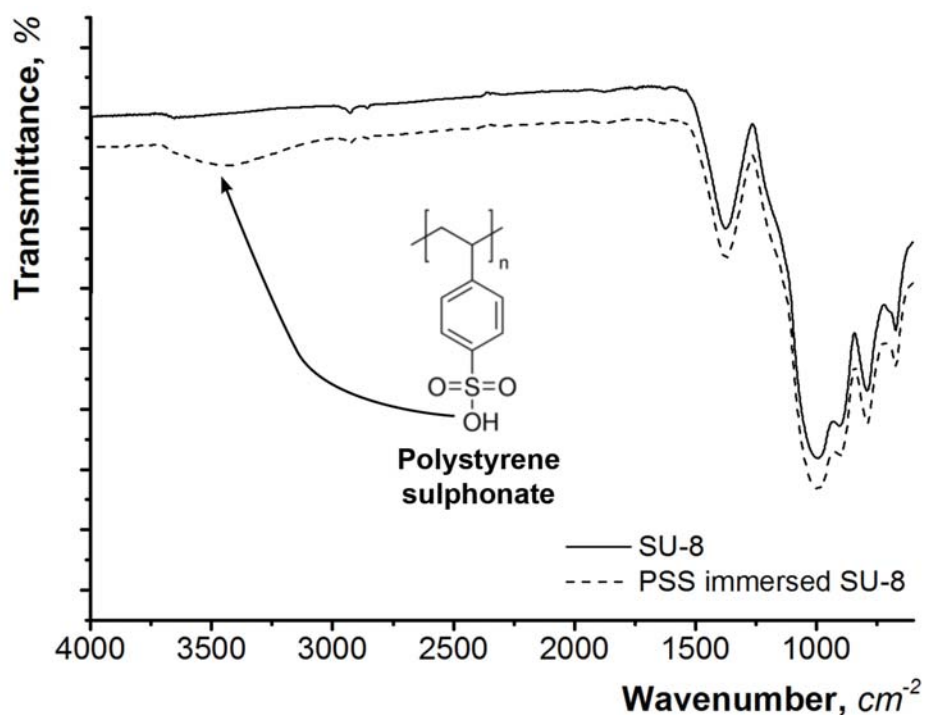


Figure 3.10: FTIR spectra of a SU-8 coated microscope slide (—) and SU-8 coated slide immersed in PSS (- - -).

at approximately 6 nA, however the macroporous coating displayed a slightly different trend during the polymerisation process. The current vs time curve for macroporous coatings reveals slight bumps throughout the polymerisation process which was thought to arise from the presence of PS-COOH beads on the microelectrode surface. For galvanostatic polymerisation an applied current of 6.28 nA for pre-defined time points resulted in a voltage of approximately 0.9 V vs Ag/AgCl for conventional (*Figure 3.11C*) and macroporous (*Figure 3.11D*) CP coatings. The macroporous CP coating showed similar bumps in the potential vs time curve. The bumps could indicate macroporous layer formation as the CP grows in thickness.

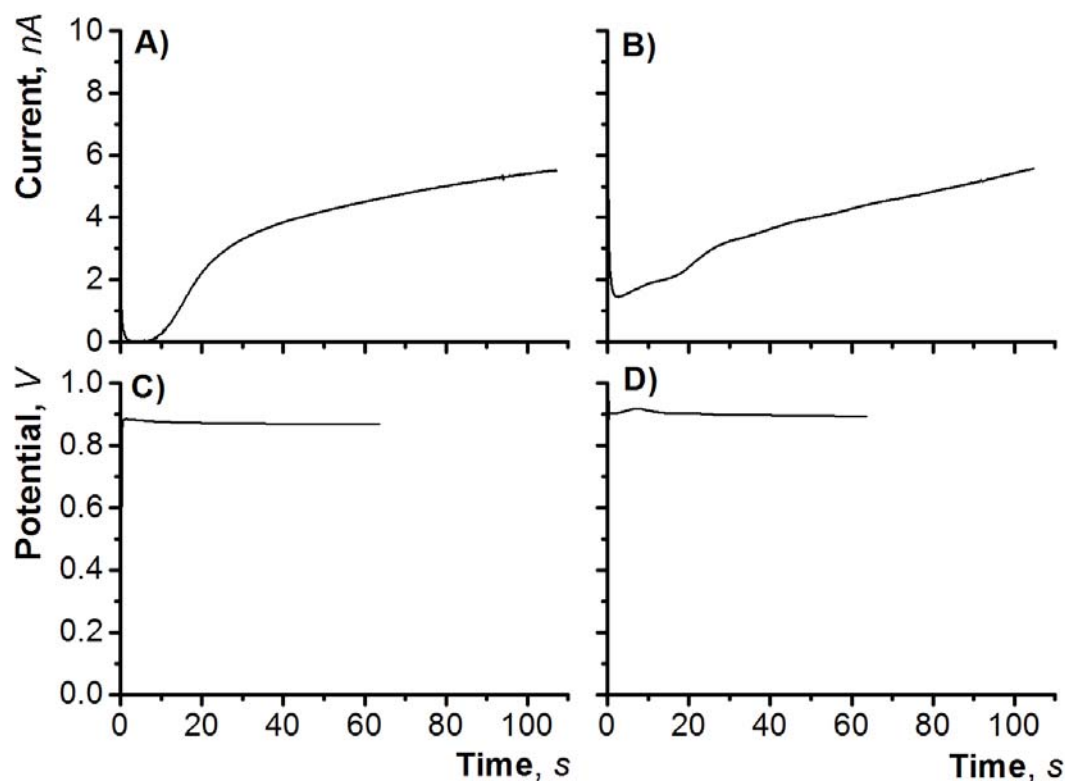


Figure 3.11: Representative plots illustrating the corresponding current response of A) conventional PEDOT/PSS and B) macroporous PEDOT/PSS polymerised potentiostatically (applied potential = 0.9 V) and voltage response of C) conventional PEDOT/PSS and D) macroporous PEDOT/PSS polymerised galvanostatically (applied current density = 2 mA cm^{-2}). All CPs had a deposition charge density of 127 mC cm^{-2} .

Selective PS-COOH Etch Selective removal of the PS-COOH bead template was trialled with one of three organic solvents (listed in order of increasing polarity); (i) tetrahydrofuran (THF) (ii) toluene and Acetone (1:3 v/v) for 24 hours and (iii) dimethylformamide (DMF).

PS-COOH solubility is highly dependent on intermolecular attractive forces and occurs when intermolecular forces are similar between solvent and PS-COOH beads — ‘like dissolves like’. SEM images were used to confirm dissolution of the template and select electrochemical tests to discern CSC_c and impedance magnitude ($|Z|$) at 1 kHz (parameters important for neuronal recording and stimulation) were undertaken to investigate the influence of solvent selection on electrochemistry. SEM images revealed that DMF was the most effective in etching the PS beads from the polymer structure, requiring only 0.5 hours (*Figure 3.12*). This was then followed by acetone/toluene at 24 hours and THF at 48 hours (notice PS-beads on the surface of the CPs at THF 24 hours).

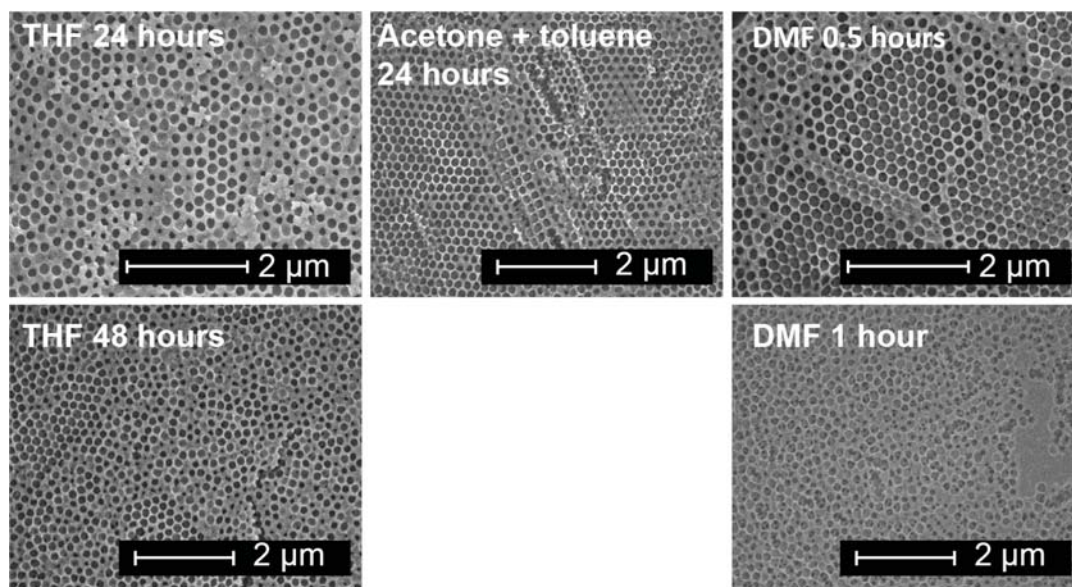


Figure 3.12: The influence of three organic solvents; tetrahydrofuran (THF), a mixture of acetone/toluene (ace/tol) and dimethylformamide (DMF) on PS-COOH bead removal at different time points. Different solvents and time points were used to screen for appropriate parameters for PS-COOH bead removal. Images are of macroporous PEDOT/PSS polymers polymerised potentiostatically at 127 mC cm^{-2} . DMF was the most effective, requiring only half an hour to fully etch PS-COOH beads.

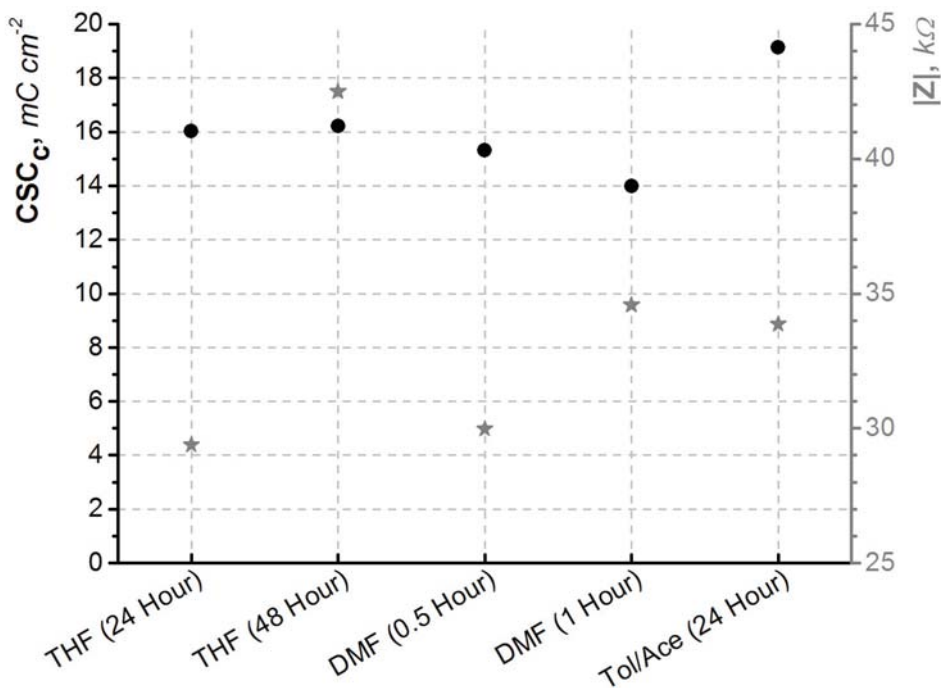


Figure 3.13: CSC_c and $|Z|$ of macroporous PEDOT/PSS polymerised potentiostatically at $127\ mC\ cm^{-2}$ treated with different solvents.

The effect of solvent treatment on electrochemical values is highlighted in *Figure 3.13*. There was no major difference in CSC_c values which ranged from $14\ mC\ cm^{-2}$ to $19\ mC\ cm^{-2}$ for macroporous PEDOT/PSS polymerised at $127\ mC\ cm^{-2}$. Acetone/toluene treatment yielded the highest CSC_c whereas DMF at 1 hour yielded the lowest. $|Z|$ at 1000 Hz showed preference to THF (24 hour) and DMF (0.5 hour), with THF (48 hour) having the highest value at $42\ k\Omega$. Notice that longer immersion in the same solvent (THF or DMF) resulted in higher $|Z|$ values, which is likely due to SU-8 damage [120]. An SEM image of the SU-8 edge for microelectrodes immersed in DMF for 1 hour reveals that the SU-8 coating started to collapse onto the CP structure (*Figure 3.14*). Based on data from SEM images and preliminary electrochemical investigations, the solvent selected was DMF at 30 minutes. This was due to its ability to rapidly etch the PS-COOH beads and its low impact on impedance modulus and CSC_c .

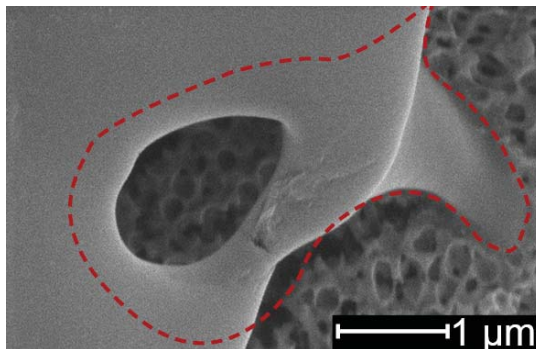


Figure 3.14: SU-8 collapse observed after 1 hour immersion in DMF to remove PS-COOH beads. The encircled area highlights an area of damage where the SU-8 appears to have dissolved and solidified onto the underlying macroporous PEDOT/PSS coating.

3.4.3 Electrochemical characterisation

Electrochemical characterisation of prepared samples was carried out using CV, EIS and VTM to obtain CSC_c , impedance spectra, CIL and effective electrochemical radius. These properties are essential when characterising microelectrodes intended to interface with neurons as they indicate recording performance (impedance) and stimulation efficacy (CSC_c and CIL). The results presented consist of 4 different groups;

1. *Conventional* PEDOT/PSS prepared **potentiostatically**
2. *Macroporous* PEDOT/PSS prepared **potentiostatically**
3. *Conventional* PEDOT/PSS prepared **galvanostatically**
4. *Macroporous* PEDOT/PSS prepared **galvanostatically**

Discussions between all four groups may become confusing, therefore, polymers polymerised potentiostatically are discussed first, followed by a comparison with galvanostatic groups.

3.4.3.1 Cyclic Voltammetry

Potentiostatically prepared samples: CV curves in PBS for both conventional (—) and macroporous (o) PEDOT/PSS prepared potentiostatically are shown in *Figure 3.15A*. CP deposition onto the gold microelectrodes showed improvement in CSC_c , as indicated by the enclosed area of the CV scan, which was further improved as more polymer was deposited. This behaviour has been reported previously [48,55,68] and is likely to arise from a larger electrochemical surface area as CP is deposited and at increasing deposition charge densities. *Figure 3.15B* displays calculated CSC_c values, indicating the expected increasing trend for both conventional and macroporous PEDOT/PSS. Surprisingly, no significant differences ($p > 0.05$) were observed for CSC_c between conventional and macroporous PEDOT/PSS.

CSC_c was used to identify the amount of charge available in the cathodic region of the CV sweep [43]. It should be kept in mind that CSC_c only gives an indication of charge storage and cannot be directly extrapolated to calculate the amount of charge available during sub-millisecond neuronal stimulation pulses. It was hypothesised that the macroporous CP structures would possess higher CSC_c values due to the increase in available surface area, however, this was not observed. Lack of penetration of the electrolyte solution into the lower layers of the macroporous CP structures could provide an explanation for similar CSC_c values between the coating types. As only the surface of the macroporous CP is interfacing with the electrolyte. These data could also indicate the inherent porosity of electrochemically deposited PEDOT/PSS where solution penetration throughout the CP bulk occurs with or without the macroporous template.

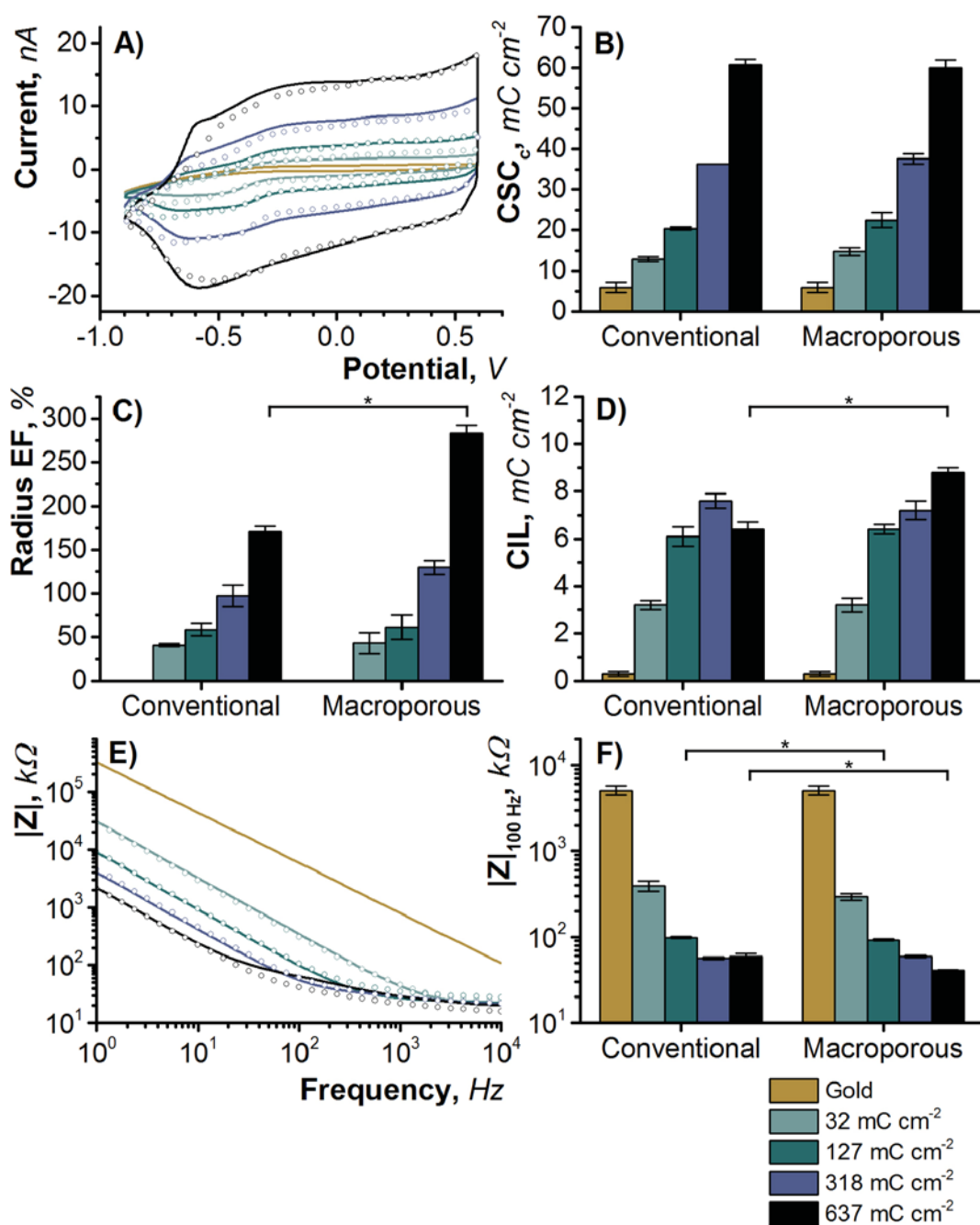


Figure 3.15: A summary of electrochemical tests for conventional (—) and macroporous (○) PEDOT/PSS polymerised *potentiostatically* at increasing deposition charge densities. The cathodic region of A) CV curves was integrated to yield B) CSC_c which displayed an increasing trend as deposition charge density increased. Both conventional and macroporous PEDOT/PSS significantly improved the C) electrochemical radius of bare gold microelectrodes. The D) charge injection limit increased with increasing deposition charge density highlighting favourable stimulation properties of CP coatings. The E) bode plot shows CP coatings successfully reduced impedance magnitude over all frequencies with F) comparing $|Z|$ at 100 Hz. Data plotted as mean \pm standard deviation, groups coupled together and marked with a star were significantly different to each other ($p < 0.05$).

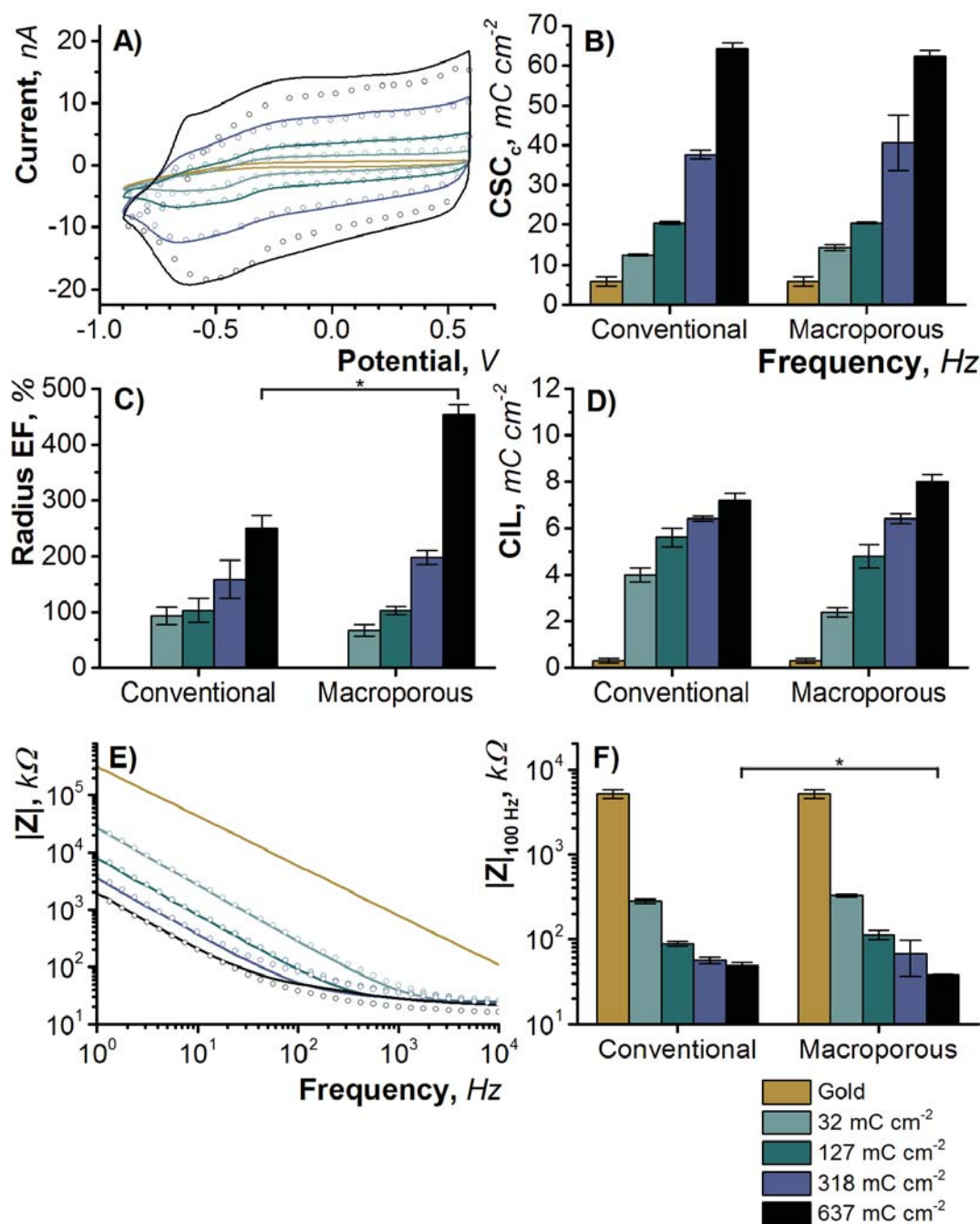


Figure 3.16: A summary of electrochemical tests for conventional (—) and macroporous (o) PEDOT/PSS polymerised *galvanostatically* at increasing deposition charge densities. The cathodic region of A) CV curves was integrated to yield B) CSC_c which displayed an increasing trend as deposition charge density increased. Both conventional and macroporous PEDOT/PSS significantly improved the C) electrochemical radius of bare gold microelectrodes. The D) charge injection limit increased with increasing deposition charge density highlighting favourable stimulation properties of CP coatings. The E) bode plot shows CP coatings successfully reduced impedance magnitude over all frequencies with F) comparing |Z| at 100 Hz. Data plotted as mean ± standard deviation, groups coupled together and marked with a star were significantly different to each other ($p < 0.05$).

CV scans in the ferri-ferro-cyanide redox couple were undertaken to calculate the electrochemical radius of the CP coatings through *Equation 3.3*. This equation is used to model steady state current at a disk microelectrode [121]. Although the electrodes presented within this work are located at the bottom of a recess, the time scale for establishing a steady state diffusion profile is fast (~ 25 ms for a $5 \mu\text{m}$ recess), therefore it can be modelled as a disk microelectrode.

$$I_s = 4nFc^*Da \quad (3.3)$$

Rearranging *Equation 3.3*, the effective radius (a) can be calculated, where n is the electron number, F is Faraday's constant ($96485.33 \text{ C mol}^{-1}$), c^* is the bulk concentration of the electroactive species ($5 \times 10^{-6} \text{ mol cm}^{-3}$), D is the diffusion coefficient of the electroactive species (taken as $0.62 \times 10^{-5} \text{ cm}^2 \text{ s}^{-1}$) and I_s is the steady state current (in amps) taken as the plateau in the anodic region of the CV scan (I vs V). The electrochemical radii were calculated for each sample and represented as a radius enlargement factor (radius EF, *Equation 3.4*), using the electrochemical radius of gold as the reference point (R_o) (*Figure 3.15C*).

$$\text{RadiusEF} = (R_{\text{sample}} - R_o) / R_o * 100 \quad (3.4)$$

An initial increase of $40 \pm 2\%$ and $43 \pm 12\%$ was observed as 32 mC cm^{-2} of conventional or macroporous CP was deposited, respectively. The enlargement factor increased as more polymer was deposited for both conventional and macroporous CPs, complimenting CSC_c results discussed above. Macroporous PEDOT/PSS deposited at 637 mC cm^{-2} displayed a significantly larger radius than conventional PEDOT/PSS ($p = 0.002$), however, the remaining 3 samples showed no significant difference ($p > 0.05$). Insufficient electrolyte penetration in macroporous CPs or inherent porosity of conventional CPs could again explain the similarity between the two coating methods.

Galvanostatically prepared samples: *Figures 3.16A & B* represent data for galvanostatically prepared conventional and macroporous PEDOT/PSS. The same trends described in potentiostatic polymerisation were noticed for galvanostatic polymerisation, with no significant difference between conventional and macroporous CPs ($p > 0.05$). There was also no significant difference between conventional or macroporous PEDOT/PSS prepared potentiostatically and samples prepared galvanostatically ($p > 0.05$). Electrochemical radius enlargement (*Figure 3.16C*) also displayed similar trends to potentiostatically prepared samples, with no significant difference between galvano- and potentiostatic groups ($p > 0.05$).

Comparison between potentiostatic and galvanostatic polymerisation was carried out to identify whether polymerisation method would influence CSC_c values of conventional and macroporous PEDOT/PSS. A study by Zhou et al. highlighted an improvement in CSC_c from 38.9 mC cm^{-2} to 202.9 mC cm^{-2} between potention- and galvanostatically polymerised PEDOT/MWCNT, respectively [5]. Lack of this observation in our studies could be due to either differences in dopant used and/or architecture of the microelectrode. Zhou et al. utilised a flat disc electrode (diameter $100 \mu\text{m}$) which allowed for electrolyte access to the sides and top of the CP electrode. Zhou et al. reported that galvanostatic polymerisation produced an ‘open structure’ film with tendency to grow in the longitudinal direction whereas potentiostatic polymerisation produced densely packed films which spanned the diameter of the electrode (transverse growth). It was this 3D longitudinal growth (alongside the open microstructure) which was theorised to improve CSC_c values of galvanostatic PEDOT/MWCNT. The electrode coatings in our study were located at the bottom of a recess therefore the electrode/electrolyte boundary existed only at the top surface of the electrode (and any penetration that occurred through microcracks or macropores). Due to the absence of significant differences between potentiostatic and

galvanostatic groups ($p > 0.05$), it is reasonable to assume surface morphology is similar in both polymerisation methods.

3.4.3.2 Voltage Transient Measurements

Potentiostatically prepared samples: The charge injection limits for both conventional and macroporous PEDOT/PSS polymerised potentiostatically were determined through voltage transient measurements (*Figure 3.15D*). Conventional PEDOT/PSS displayed a substantial increase in CIL ($3.2 \pm 0.2 \text{ mC cm}^{-2}$ vs $0.3 \text{ mC cm}^{-2} \pm 0.1$) at the lowest deposition charge density of 32 mC cm^{-2} which was followed by gradual increases as more polymer was deposited. Macroporous PEDOT/PSS displayed a more gradual increase in CIL, however, the largest value of 8.8 mC cm^{-2} was attributed to macroporous PEDOT/PSS polymerised at 637 mC cm^{-2} . A high CIL is beneficial for stimulating electrodes as it reduces the incidence of irreversible faradaic reactions preventing damage to the electrode and surrounding tissue [34]. Comparisons between obtained experimental values and values in the literature (*Figure 2.1*) reveal that a value of 8.8 mC cm^{-2} is significantly larger than traditional planar electrodes such as Pt and electrode coatings such as IrOx or CNT.

Galvanostatically prepared samples: Minimal differences were observed between samples polymerised using potentiostatic or galvanostatic methods (*Figure 3.16D*). Overall, potentiostatic deposition seemed to result in slightly higher CIL values, with the highest value still attributed to macroporous PEDOT/PSS polymerised potentiostatically at 637 mC cm^{-2} .

3.4.3.3 Electrochemical Impedance Spectroscopy

Potentiostatically prepared samples: *Figure 3.15E* represents a Bode plot which displays impedance magnitude ($|Z|$) against frequency. This plot is important when characterising electrodes for neuronal recordings due to the frequency dependant nature of neuronal signals. Depending on the technique used, neuronal signals reside within different frequency bands [37]. For example, local field potentials are often recorded at less than 300 Hz whereas extracellular spike potentials reside between 300 and 3000 Hz [37]. *Figure 3.15E* shows that both conventional and macroporous PEDOT/PSS coatings were successful in reducing impedance magnitude of uncoated gold microelectrodes over all frequency values. Commonly, $|Z|$ is taken at 1000 Hz as a representative figure for neuronal signals, however, samples polymerised at a charge density greater than 127 mC cm^{-2} were dominated by access resistance at this frequency. Therefore, comparisons between samples were made at 100 Hz, where $|Z|_{100\text{Hz}}$ refers to impedance magnitude at 100 Hz.

Figure 3.15F shows $|Z|_{100\text{Hz}}$ for all PEDOT/PSS coatings prepared potentiostatically. A large initial decrease from $5104 \pm 600 \text{ k}\Omega$ to $393 \pm 53 \text{ k}\Omega$ and $293 \pm 24 \text{ k}\Omega$ for conventional and macroporous CP coatings can be seen at a deposition charge density of 32 mC cm^{-2} , respectively. Further deposition of polymer resulted in a less drastic, steady decrease in $|Z|_{100\text{Hz}}$. This behaviour has previously been reported by a number of research groups and is thought to arise from increasing electrochemical surface area associated with more pronounced nodular structures [65, 66, 88]. Comparisons between the two polymer coating groups reveals that there was no statistically significant difference in $|Z|_{100\text{Hz}}$ at polymerisation charge densities of 32 mC cm^{-2} and 318 mC cm^{-2} ($p > 0.05$). However, macroporous polymers deposited at 127 mC cm^{-2} and 637 mC cm^{-2} displayed a statistically significant reduction in $|Z|_{100\text{Hz}}$ ($p = 0.04$ and 0.02 , respectively) with the lowest $|Z|_{100\text{Hz}}$ value of $40.7 \pm 0.5 \text{ k}\Omega$ attributed to

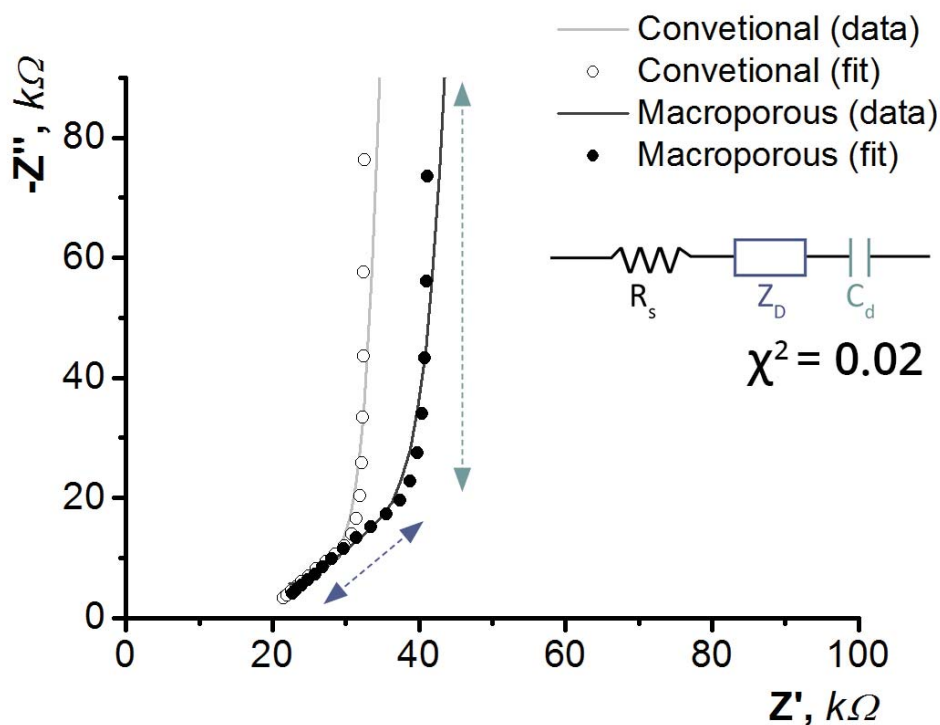


Figure 3.17: Nyquist plot of EIS data for representative CP electrode coatings (polymerised at 318 mC cm^{-2}) illustrating the fit of the RZC model. The graph shows where constituent elements of the model are found on the Nyquist plot.

macroporous PEDOT/PSS polymerised at 637 mC cm^{-2} .

An alternative method of representing microelectrode impedance spectra is through a Nyquist diagram which plots the imaginary (capacitive) Z component (Z'') against real (resistive) Z component (Z'), within the frequency range analysed (*Figure 3.17*). The Nyquist diagram allows for equivalent circuit modelling of the microelectrodes to quantify solution and microelectrode properties such as ionic diffusion, solution resistance and electrode capacitance. The circuit chosen to fit this data was taken from Bobacka et al. which models PEDOT films in aqueous electrolyte solutions as it was found to have good fit with our data ($\chi^2 \approx 0.02$) [111] (*Figure 3.17*). *Table 3.1* lists all modelled parameters with corresponding values for conventional and macroporous PEDOT/PSS polymerised either potenti- or galvanostatically.

The solution resistance, R_s , was found to be similar for both coating methods with the exception of samples polymerised at 637 mC cm^{-2} , which displayed lower values. *Equation 3.5* shows that R_s is proportional to solution resistivity (ρ), and inversely proportional to the electrochemical radius (r) [122].

$$R_s = \frac{\rho}{4r} \quad (3.5)$$

The electrochemical radius modelled above using the ferri-ferrocyanide couple (*Figure 3.15C*) correlates with the observed solution resistance. For conventional PEDOT/PSS coatings at deposition charge densities of 32, 127 and 318 mC cm^{-2} there was no significant difference in their modelled electrochemical radius ($p > 0.05$) and hence, no significant difference observed in R_s for these deposition charge densities ($p > 0.05$). For macroporous PEDOT/PSS coatings at deposition charge densities of 32, 127 and 318 mC cm^{-2} , a significant increase was observed at 318 mC cm^{-2} (when compared to 32 and 127 mC cm^{-2}) and correlates with the decrease in R_s from $23 \pm 1 \text{ k}\Omega$ to $19 \pm 1 \text{ k}\Omega$. Both conventional and macroporous PEDOT/PSS coatings deposited at 637 mC cm^{-2} displayed a significant increase in electrochemical radius when compared to lower deposition charge densities and this correlates with the significant drop in R_s from approximately $20 \text{ k}\Omega$ to $16 \pm 1 \text{ k}\Omega$ and $14 \pm 1 \text{ k}\Omega$ for conventional and macroporous PEDOT/PSS, respectively. The only significant difference between conventional and macroporous PEDOT/PSS coatings was at 637 mC cm^{-2} , where macroporous PEDOT/PSS significantly reduced R_s from $16 \pm 1 \text{ k}\Omega$ to $14 \pm 1 \text{ k}\Omega$.

There was no obvious trend for diffusional resistance, R_D , however an overall decrease in R_D was noticed as more polymer was deposited in both conventional and macroporous PEDOT/PSS. Significantly lower R_D values were noticed for macroporous PEDOT/PSS polymerised at 127 mC cm^{-2} and 637 mC cm^{-2} (p

= 0.04 and 0.03, respectively). In contrast, macroporous PEDOT/PSS polymerised at 32 mC cm⁻² appeared to increase R_D , illustrating that the pores were not effective in reducing R_D for thin CP coatings ($p = 0.002$).

The trend for τ_D was similar for both CP coatings where a decrease in τ_D from 32 mC cm⁻² to 318 mC cm⁻² was observed, after which, a slight increase was seen for PEDOT/PSS polymerised at 637 mC cm⁻². The diffusional time constant is proportional to the diffusion length (L) and inversely proportional to the diffusion coefficient (D) (Equation 3.6) [70, 111].

$$\tau_D = \frac{L^2}{D} \quad (3.6)$$

An assumption can be made that L is proportional to film thickness and subsequently, the polymerisation charge density (thicker films as polymerisation charge is increased) – therefore an increasing τ_D is expected as polymerisation charge density is increased. The apparent decrease in τ_D for conventional and macroporous films may arise due to a more pronounced nodular and porous structure at higher deposition charge densities, respectively. Such a structure may decrease the diffusion length due to penetration of electrolyte within the pores of the CP – resulting in faster ion diffusion [111]. Interestingly, macroporous PEDOT/PSS coatings only significantly reduced τ_D at a deposition charge density of 127 mC cm⁻² ($p = 0.02$), when compared to conventional PEDOT/PSS. This observation further suggests the intrinsic porosity of conventional PEDOT/PSS due to its inherent nodular morphology.

The electronic capacitance, C_d , increased with polymerisation charge density for both conventional and macroporous coatings. Macroporous PEDOT/PSS coatings offered a significant increase in C_d at a deposition charge density of 127 mC cm⁻², however, conventional PEDOT/PSS was superior at the deposition charge density of 637 mC cm⁻². Ionic capacitance, C_D , did not show the same

trend and was observed to decrease with polymerisation charge density for both conventional and macroporous PEDOT/PSS coatings. The total capacitance showed a similar trend to C_d and increased as polymerisation charge density increased for both CP structures. This increasing trend can be explained by a more pronounced capacitive double layer which forms as a result of larger electrochemical surface area as deposition charge density increases [111]. C_{tot} was found to be similar for both conventional and macroporous PEDOT/PSS coatings ($p > 0.05$). Note that C_{tot} is dominated by the electronic capacitance at lower polymerisation charge densities and by the ionic capacitance at higher charge densities for both deposition methods.

Impedance spectra can further be used to estimate microelectrode noise contributions when used for neuronal recordings through the calculation of thermal noise, allowing for an appreciation of the impact of microelectrode impedance on recording signal quality. The Johnson-Nyquist thermal noise relation states that thermal noise is directly proportional to the resistive impedance component (Z') and an RMS noise value can be calculated, within a given frequency band, by inputting experimental Z' values into the equation (*Equation 3.2*). (*Figure 3.18*) shows both conventional and macroporous PEDOT/PSS successfully lowered thermal noise amplitudes of gold from $35 \pm 3 \mu V_{p-p}$ to $18 \pm 9 \mu V_{p-p}$ and $14 \pm 1 \mu V_{p-p}$, respectively, at the lowest deposition charge density of 32 mC cm^{-2} . Further deposition of polymer at 127 and 318 mC cm^{-2} produced no significant reduction in predicted thermal noise for both macroporous and conventional PEDOT/PSS. At the highest deposition charge density of 637 mC cm^{-2} macroporous PEDOT/PSS significantly reduced thermal noise of conventional PEDOT/PSS from $12.6 \pm 0.3 \mu V_{p-p}$ to $10.5 \pm 0.6 \mu V_{p-p}$ ($p = 0.03$). Low thermal noise is ideal for recording electrodes as it reduces the noise floor and allows for improved detection of neuronal activity.

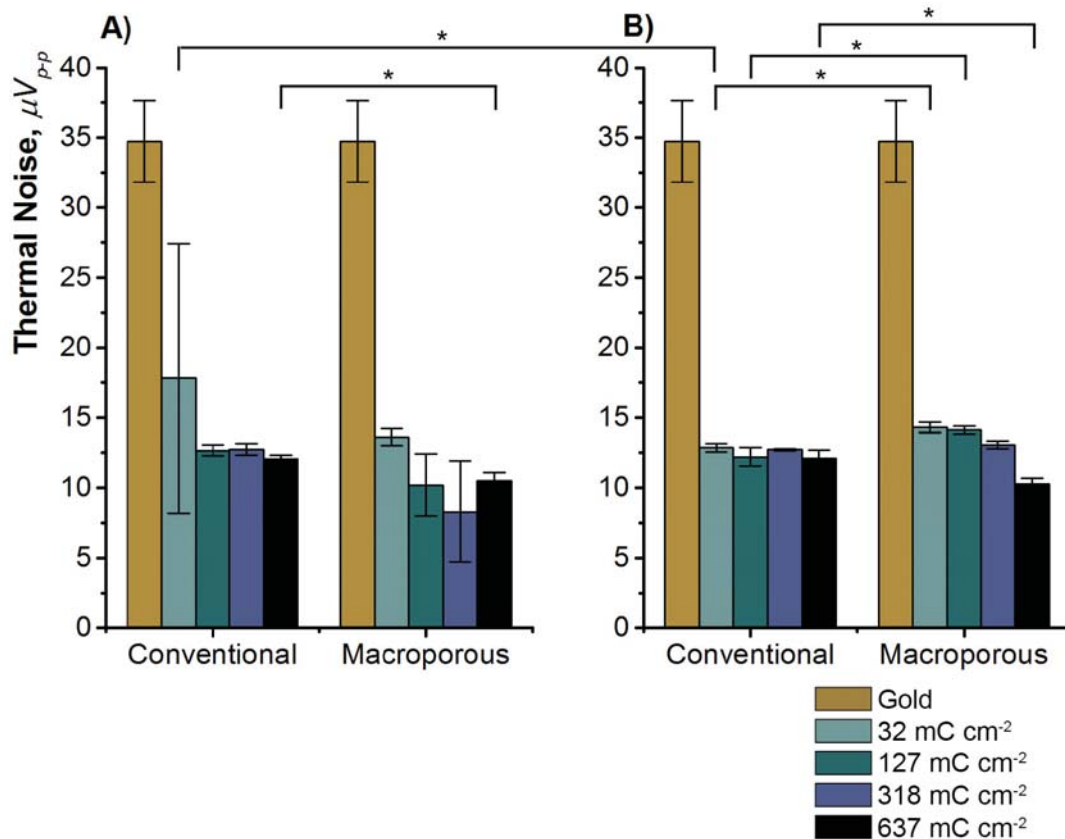


Figure 3.18: Predicted thermal noise values of gold, conventional PEDOT/PSS and macroporous PEDOT/PSS polymerised either A) potentiostatically or B) galvanostatically. Thermal noise of the microelectrode can be used to predict its noise amplitude during neuronal recording. Data plotted as mean \pm standard deviation, groups coupled together and marked with a star were significantly different to each other ($p < 0.05$).

Galvanostatically prepared samples: Galvanostatically prepared samples displayed identical trends to potentiostatically polymerised samples and data of significant difference were scarce. For conventional PEDOT/PSS, a significant increase in C_D and C_{tot} was observed for polymers polymerised galvanostatically at 318 mC cm^{-2} as compared to potentiostatically prepared polymers. This may have resulted from a larger electrochemical surface area and correlates with slightly larger radius EF values of $158 \pm 34\%$ for galvanostatically polymerised PEDOT/PSS vs $136 \pm 15\%$ for potentiostatically polymerised. For macroporous PEDOT/PSS, a significant increase in R_D was observed for galvanostatically polymerised samples at 32 mC cm^{-2} and C_{tot} at 318 mC cm^{-2} .

Although these values differed, no deviations from the trends described in potentiostatically polymerised PEDOT/PSS were observed. Predicted thermal noise values (*Figure 3.18B*) showed a similar trend to potentiostatically polymerised polymers, where a drastic decrease was seen at the lowest deposition charge density — followed by gradual changes. The only significant difference between potentiostatic and galvanostatic groups was noticed at 32 mC cm^{-2} .

Table 3.1: Modelled impedance parameters for both conventional and macroporous PEDOT/PSS polymerised either potentiostatically or galvanostatically at different deposition charge densities ($n = 3$, mean \pm standard deviation). Conventional PEDOT/PSS values highlighted gray were significantly different to corresponding values for macroporous PEDOT/PSS (within the same polymerisation group i.e. potentiostatic or galvanostatic). Circled cells were significantly different to corresponding values in the opposite polymerisation group (i.e. potentiostatic conventional PEDOT/PSS vs. galvanostatic conventional PEDOT/PSS).

Sample	Charge density (mC cm ⁻²)	R _s (kΩ)	R _D (kΩ)	τ _D (ms)	C _d (nF)	C _D (nF)	C _{tot} (nF)
Potentiostatically Prepared Samples							
Conventional PEDOT/PSS	32	21 ± 1	106 ± 16	128 ± 6	6 ± 1	1179 ± 301	5.4 ± 1
	127	23 ± 2	139 ± 45	26 ± 7	16 ± 2	201 ± 69	15 ± 1
	318	20 ± 2	42 ± 2	2 ± 1	130 ± 42	52 ± 4	37 ± 1
	637	16 ± 1	85 ± 7	7 ± 1	1318 ± 419	85 ± 1	80 ± 1
Macroporous PEDOT/PSS	32	22 ± 1	180 ± 15	133 ± 12	5 ± 1	743 ± 114	5 ± 1
	127	23 ± 1	22 ± 2	3 ± 1	21 ± 1	130 ± 58	18 ± 2
	318	19 ± 1	47 ± 12	3 ± 1	84 ± 32	68 ± 20	35 ± 1
	637	14 ± 1	55 ± 4	8 ± 1	143 ± 25	140 ± 22	69 ± 2
Galvanostatically Prepared Samples							
Conventional PEDOT/PSS	32	21 ± 1	153 ± 37	121 ± 11	6 ± 1	742 ± 257	6 ± 1
	127	22 ± 3	110 ± 17	22 ± 4	17 ± 4	202 ± 69	16 ± 4
	318	19 ± 1	58 ± 27	4 ± 2	123 ± 4	65 ± 2	43 ± 1
	637	17 ± 2	87 ± 9	10 ± 1	283 ± 28	110 ± 8	80 ± 3
Macroporous PEDOT/PSS	32	22 ± 1	507 ± 104	132 ± 14	6 ± 1	267 ± 59	6 ± 1
	127	19 ± 1	114 ± 50	3 ± 2	65 ± 26	26 ± 6	18 ± 1
	318	18 ± 1	174 ± 13	14 ± 2	85 ± 5	78 ± 11	41 ± 2
	637	13 ± 1	57 ± 6	10 ± 2	138 ± 9	170 ± 24	76 ± 6

3.4.3.4 Summary of Electrochemical Results

Potentiostatically Prepared PEDOT/PSS All tests revealed an improvement in electrochemical properties (higher CSC_c , CIL, lower $|Z|_{100Hz}$ and lower thermal noise) as deposition charge density increased for both conventional and macroporous PEDOT/PSS. CV results displayed no significant difference in CSC_c between conventional and macroporous PEDOT/PSS. CIL values favoured macroporous structures with the highest value (8.8 mC cm^{-2}) attributed to macroporous PEDOT/PSS at a charge density of 637 mC cm^{-2} . The lowest $|Z|_{100Hz}$ value of $40.7 \pm 0.5 \text{ k}\Omega$ was also attributed to macroporous PEDOT/PSS at a charge density of 637 mC cm^{-2} , however, no significant difference between conventional and macroporous structures existed at lower deposition charge densities. The thermal noise of gold decreased by a factor of three after application of conventional and macroporous PEDOT/PSS coatings at a deposition charge density of 127 mC cm^{-2} , further deposition of CP did not significantly alter thermal noise for both coating methods.

Galvanostatically Prepared PEDOT/PSS The trends observed in potentiostatically prepared PEDOT/PSS (both conventional and macroporous) were also observed in the galvanostatically prepared coatings.

Due to similarities in electrochemical results between potentiostatic and galvanostatic polymerisation, further morphology, performance stability and biocompatibility tests were carried out on potentiostatically prepared conventional and macroporous samples only.

3.4.4 Morphological characterisation

Conventional CP structures displayed a typical slightly nodular rough surface morphology which became more pronounced with higher charge densities (*Figure 3.19*). This increasing nodularity suggests a larger electrochemical surface area and confirms results observed for CSC_c , CIL , $|Z|$, τ_D and C_{tot} . The imaging of the macroporous CP structures revealed a well-ordered porous morphology, with pore sizes in close agreement with the PS-COOH beads used for templating (ca. 230 nm). Large circular cavities can be seen in the macroporous CP structures at charge densities of 318 mC cm^{-2} and 637 mC cm^{-2} ; these defects are possibly due to contamination of the PS-COOH solution which resulted in deposition of large particles into the microelectrode recess. Cracks are likely to have occurred as an artefact of the vacuum used during SEM imaging [103].

Figure 3.19 shows the growth and thickness of the macroporous CP is dependent on the charge passed during polymerisation. At the lowest charge density of 32 mC cm^{-2} , a thin layer of CP can be seen on the surface of the electrode with depressions evident from the PS-COOH colloids. Despite the colloids coating the MEA a continuous PEDOT/PSS film formed over the gold which implies weak adsorption forces between the PS-COOH beads and microelectrode, allowing the CP to grow under the colloidal template displacing it from the surface of the gold microelectrode. Further deposition of CP results in multiple porous layers at 127 mC cm^{-2} , as indicated by higher magnification images where openings are seen at the bottom of pores revealing a lower layer. Up to and including a charge density of 127 mC cm^{-2} a face-centred cubic (fcc) lattice is evident within the macroporous structure, this is characteristic of PS-COOH deposition and shows that CP growth was highly influenced by the sacrificial colloidal structure [103, 110]. At higher charge densities of 318 mC cm^{-2} and 637 mC cm^{-2} , the fcc structure starts to diminish, which could be associated with the arrangement of PS-COOH beads in the cavity. It is possible that a

highly ordered template exists at the bottom of the microelectrode recess and this order fades at the top of the recess due to differences in elevation on the MEA device.

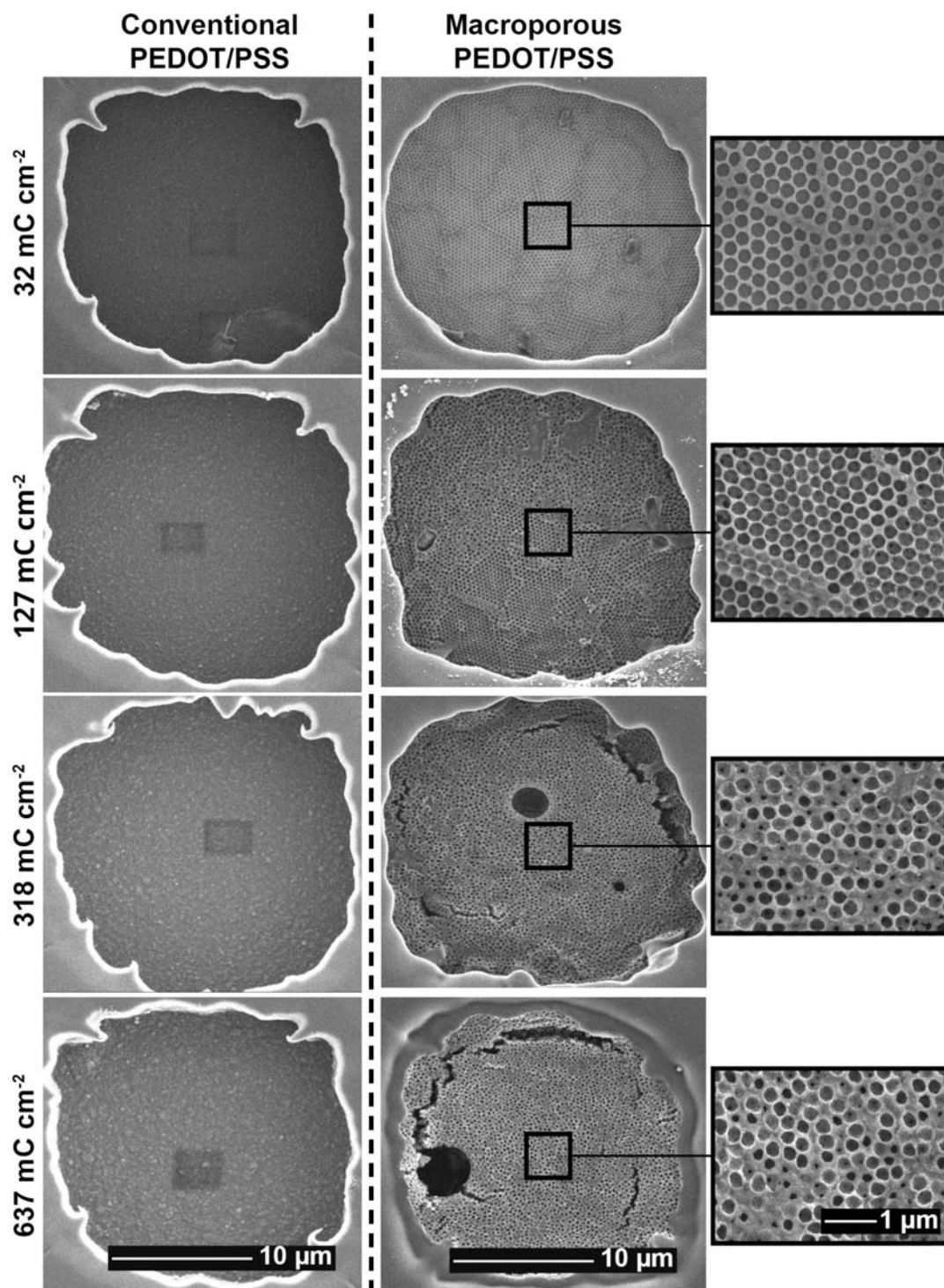


Figure 3.19: SEM images of conventional and macroporous PEDOT/PSS structures potentiostatically polymerised. SEM images were taken with a secondary electron detector at an accelerating voltage of 5.0 kV and a spot size of 2. The left hand panel shows conventional PEDOT/PSS with a scale bar of 10 μm. The middle and right hand panels show macroporous PEDOT/PSS with a scale bar of 10 μm and 1 μm, respectively.

3.4.5 Performance Stability

Performance stability of the CP coatings was tested through application of a biphasic, charge balanced current pulse with a charge density of 3 mC cm^{-2} (*Figure 3.5*). $|Z|$ was monitored throughout the experiment and allowed for the assessment of electrode integrity as a function of pulse number. Here we define electrode failure, or delamination, as a 100% change in the impedance magnitude at 100 Hz. *Figure 3.20* displays the % change in impedance as a function of pulse number. For conventional PEDOT/PSS, polymers deposited at 32 mC cm^{-2} delaminated within 15×10^3 pulses were excluded from the graph. Conventional PEDOT/PSS coatings deposited at 127 mC cm^{-2} performed slightly better and were found to delaminate after 90×10^3 pulses. At higher deposition charge densities of 318 and 637 mC cm^{-2} , conventional CP coatings lasted for up to 1590×10^3 pulses. These results indicate a dependence of performance stability on deposition charge density, with thicker coatings being less prone to electrode delamination.

For macroporous PEDOT/PSS, polymers deposited at 32 mC cm^{-2} , as well as those deposited at 127 mC cm^{-2} delaminated within 15×10^3 pulses and were also excluded from the graph. At higher deposition charge densities of 318 and 637 mC cm^{-2} , macroporous CP coatings lasted for up to 870×10^3 and 1000×10^3 pulses, respectively. A similar dependence of performance stability on deposition charge density was observed. In contrast to conventional coatings, macroporous coatings displayed an improvement in $|Z|_{100\text{Hz}}$ of up to 30% within the first 500×10^3 pulses. This may have resulted from electrolyte penetration further down the macroporous structure as a result of continuous polymer contraction and expansion.

Overall, conventional PEDOT/PSS coatings were less prone to delamination than macroporous PEDOT/PSS. A promising aspect of macroporous coatings

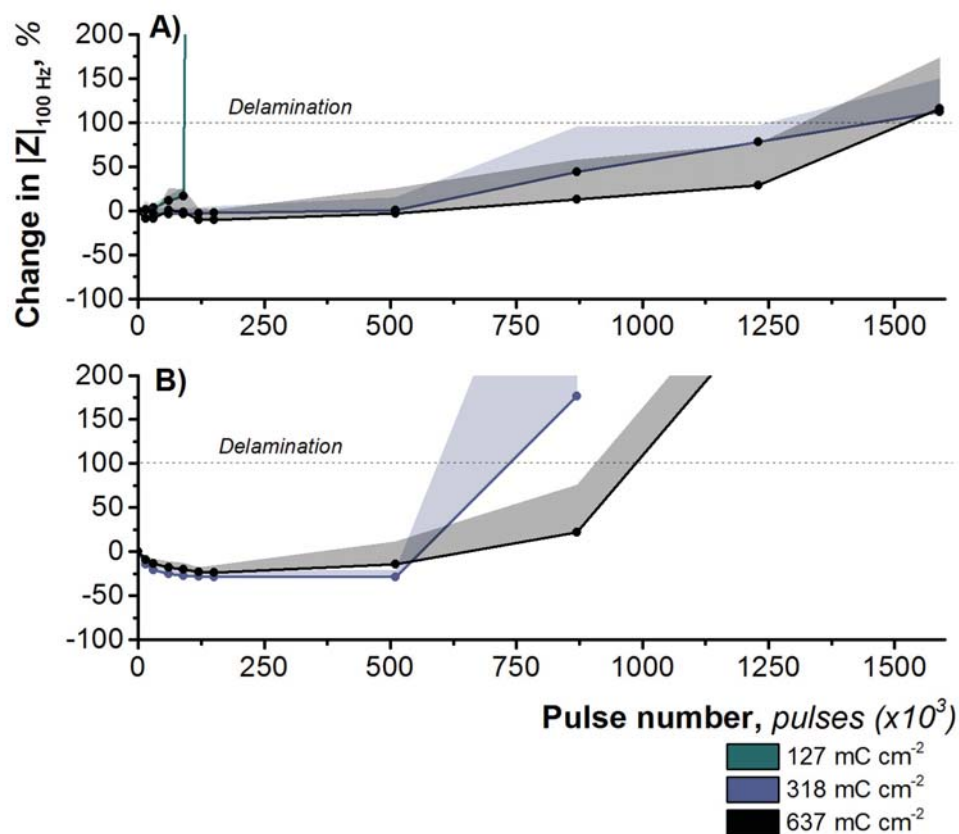


Figure 3.20: Performance stability of A) conventional PEDOT/PSS and B) macroporous PEDOT/PSS coatings when subject to biphasic, charge balanced current pulses at an amplitude of $9 \mu\text{A phase}^{-1}$ and pulse frequency of 50 Hz. The plot show change in $|Z|_{100\text{Hz}}$ as a function of pulse number. Delamination was observed to occur when the change in $|Z|_{100\text{Hz}}$ exceeded 100%, as indicated by the dashed line on the graph. Data points indicated the mean and shaded sections indicate the positive standard deviation ($n = 3$).

is the improvement of $|Z|$, however, its porous nature seems to limit its use due to poor coating adhesion to the underlying substrate. Previous research has demonstrated the dependence of coating adhesion on dopant type and underlying substrate morphology, such as roughed platinum [55, 63, 87, 123]. Experimentation with different dopants and/or different substrates could result in a promising stimulating electrode material based on this macroporous structure.

3.4.6 Biocompatibility

Biocompatibility assays revealed primary hippocampal cells were able to be grown on all substrates tested. *Figure 3.21* shows typical composite images of neurons stained with both the neurite outgrowth (orange/red) and viability (green) indicators at DIV 16. Viable neuronal growth was validated by the presence of green fluorescence within the cell bodies and the vast extension of neuronal processes over the substrates. Neurite outgrowth is frequently used to demonstrate substrate biocompatibility [124, 125] and was quantified using tracing algorithms in ImageJ.

Figure 3.22 plots the length of neurites supported per cm^2 and number of viable cells per cm^2 , for all substrates tested. A significant increase in neurite length for neurons cultured on MEA devices was observed when compared to control slides ($p = 0.03$). Gold, conventional PEDOT/PSS, macroporous PEDOT/PSS and SU-8 coated slides revealed similar values to the control slide, with no significant differences apparent between the groups ($p > 0.05$). The similarity of each substrate compared with control conditions indicate sufficient biocompatibility of the substrates for primary neuronal culture and re-affirms the usability of our constructed MEA devices for neuronal studies. A comparison between conventional and macroporous PEDOT/PSS revealed no significant difference in neurite outgrowth. Previous reports have highlighted the importance of surface roughness on neuronal attachment and outgrowth [65, 67]. Although the porous structure is thought to be inherently rougher than conventional counterparts, the lack of difference suggests that conventional PEDOT/PSS possess a similar degree of surface roughness in the form of nodules rather than pores.

Figure 3.22 showed no significant difference in the number of viable neurons between control slides and the 5 test substrates ($p > 0.05$), however, in contrast to neurite outgrowth assays, the absolute mean value of the control was

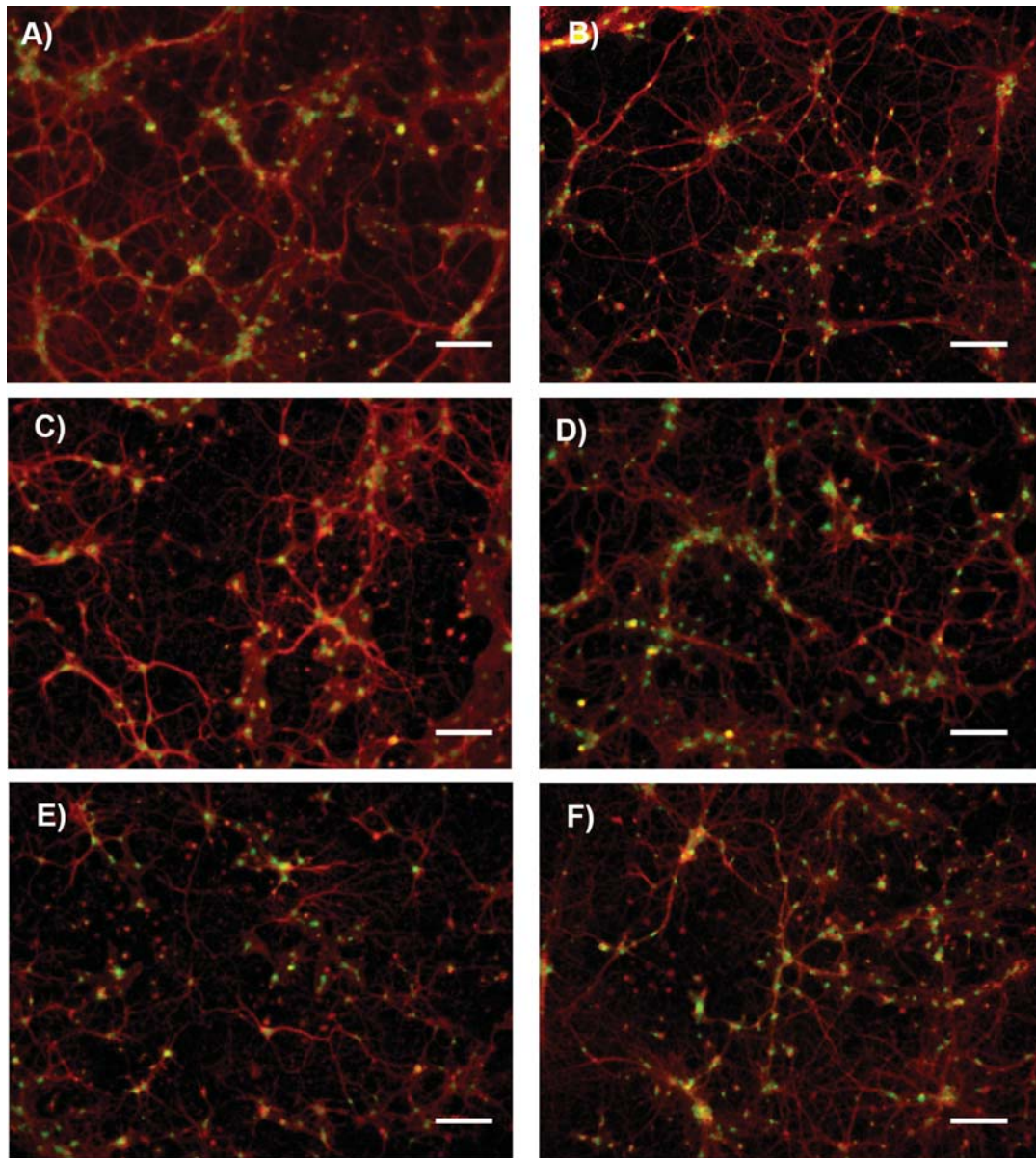


Figure 3.21: Representative composite images of primary hippocampal neurons grown on A) control slides, B) MEA, C) Bare gold, D) conventional PEDOT/PSS, E) macroporous PEDOT/PSS and F) SU-8 at DIV 16. Neurons were stained with cell viability and neurite outgrowth indicators present in the Molecular Probes neurite outgrowth kit. Scale bars represent 100 μm .

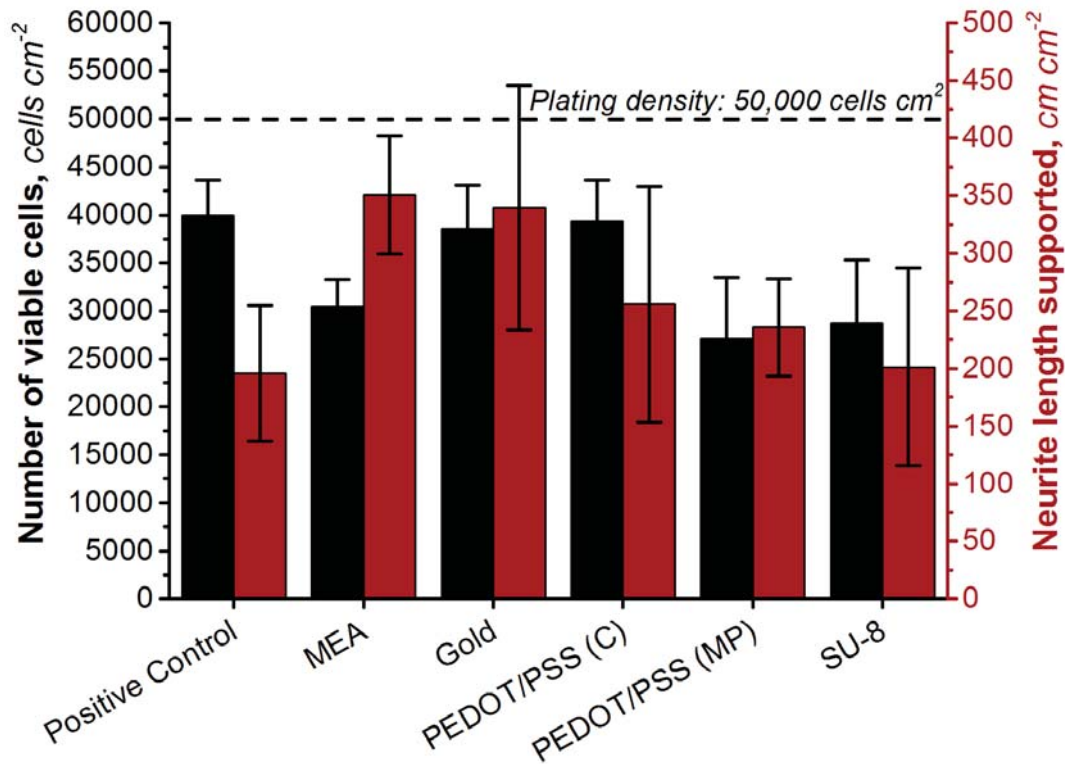


Figure 3.22: Bar graph indicating the number of viable cells per cm⁻² and total neurite length supported on each substrate. The dotted line represents the initial plating density (50,000 cells cm⁻²). Data was plotted as the mean with error bars indicating standard deviation ($n = 3$)

slightly higher than most substrates (excluding gold). A higher number of viable cells were observed on conventional PEDOT/PSS than macroporous PEDOT/PSS coatings suggesting that cell viability was improved on conventional PEDOT/PSS.

Although primary neurons are likely to interact with SU-8 on the MEA devices predominantly, biocompatibility characterisation of all components was necessary to illicit whether any materials antagonised neuronal growth and viability.

3.5 Conclusions

Customised MEA devices were successfully fabricated to allow for the study of CP surface coatings on electrochemical properties relevant to neuronal recording and stimulation. A reproducible method to deposit macroporous PEDOT/PSS was outlined and justified via electrochemical characterisation and SEM imaging. Initial immersion in a surfactant solution such as PSS and selective etching of PS-beads using DMF for 30 minutes resulted in the successful fabrication of macroporous PEDOT/PSS structures.

Conventional and macroporous PEDOT/PSS polymerised potentiostatically both improved electrochemical properties of bare gold microelectrodes through an increase in CSC_c and CIL and decrease in $|Z|_{100Hz}$ and thermal noise. Comparisons between potentiostatically polymerised conventional and macroporous PEDOT/PSS coatings revealed no significant difference in CSC_c . Macroporous PEDOT/PSS improved the electrochemical radius, CIL, $|Z|_{100Hz}$ and thermal noise of conventional PEDOT/PSS at the highest deposition charge density of 637 mC cm^{-2} , otherwise, no significant differences were noticed at lower deposition charge densities. Galvanostatic polymerisation produced no additional improvement in electrochemical properties over potentiostatic polymerisation and similar trends were noticed between galvanostatically prepared conventional and macroporous PEDOT/PSS.

Performance stability highlighted a dependence of deposition charge density on substrate adhesion for both conventional and macroporous PEDOT/PSS coatings. Overall, conventional PEDOT/PSS displayed better stability, however, the macroporous structure exhibited interesting improvements in $|Z|$ below 500×10^3 pulses. The improvement in $|Z|$ provides a promising application for macroporous coatings as long-term stimulating electrodes, however, their poor adhesion to the underlying substrate must first be addressed. Biocompatibility

assays confirmed the ability of MEA devices to support the growth and viability of primary hippocampal neurons. Comparable results to control coverslips were seen across all the substrates tested.

These data suggest that macroporous electrode coatings are beneficial for neuronal recording and stimulation at a deposition charge density of $> 318 \text{ mC cm}^{-2}$. However, macroporous structures are limited by poor substrate adhesion and more work towards improving the stability of these structures is required for long term applications.

Chapter 4

Development of a Bioamplifier and Acquisition System for Neuronal Recording Through MEA Devices

4.1 Introduction

In order to record neuronal signals from microelectrode arrays (MEAs), an electrophysiology system capable of amplifying and digitising signals from the extracellular microelectrodes was required. Ideally, these systems would consist of multi-channel, low noise amplifiers which serve to bring microelectrode potentials within levels adequate for the resolution of an analog to digital converter (ADC). The ADC would then sample the amplified signals from multiple channels simultaneously at an adequate sampling rate which fulfils the Nyquist sampling criterion [126]. Nyquist sampling criterion states that the minimum sampling rate should be twice the maximum component frequency of the function being sampled. The importance of amplifier design is highlighted in many papers [38, 42, 127–132] and is one of the main determinants of noise in extracellular neuronal recordings — with the other being microelectrode design [41].

Systems for recording from MEA slides are available commercially, however, cost and the inability to customise hardware/software for specific purposes may present as limiting factors for some users. Here, we detail schematics for a simple system capable of low-noise neuronal amplification, combined with an ADC from National Instruments. This system provides a flexible, low-cost (US\$21 for the first channel + US\$11 for each additional channel), low-noise approach to acquisition of neuronal signals from MEA devices.

Parameters for amplifier and ADC specifications were informed by the nature of neuronal signals and microelectrode characteristics. Voltage spikes associated with extracellular neuronal recordings typically range between 50 and 500 μV peak to peak [40], meaning a gain of at least 1000 had to be used to bring voltage levels within the resolution of the ADC. Signal pulse duration is typically between 1 and 4 ms [40, 41], meaning a sampling rate of at least 2000 S s^{-1} is required to fulfil Nyquist criterion. The waveform is biphasic in nature, with

an initial negative phase, associated with neuronal depolarisation, followed by a positive repolarisation phase. Therefore, the designed amplifier should be capable of amplifying negative voltages, as well as positive.

Microelectrodes have high impedance (*Chapter 3*), typically ranging between 10 k Ω and 10 M Ω in the frequency range of 1 to 10,000 Hz. The input impedance of the amplifier front end should therefore be sufficiently larger than the electrode impedance to avoid signal reduction at the input. A DC offset is noticed when the microelectrodes are immersed in solution as a result of capacitive charging at the electrode/electrolyte boundary. This DC offset should be rejected to prevent saturation at subsequent stages of amplification.

To facilitate low noise recording, power supply and connections to the amplifier front end should introduce as little noise as possible. A connection method between MEA and the amplifier front end should be sufficiently shielded to ensure low interference from surrounding electromagnetic noise. Furthermore, the use of a DC power source, such as a battery, is ideal to prevent further interference from AC mains power supplies. Ultimately, the constructed amplifier should possess an intrinsic noise value of $< 45\%$ that of microelectrode thermal noise to enable efficient recording from MEA devices [37].

4.1.1 Aims & Objectives

In this chapter, we hypothesise that the construction of a low noise amplification system will compliment microelectrode modification strategies in order to produce a low noise, highly sensitive recording set-up. The aim of this chapter was to construct a low noise amplification system, fulfilling the design criteria mentioned above, coupled with an ADC capable of capturing neuronal activity. As the expected thermal noise of conducting polymer (CP) coatings is significantly lower than unmodified gold microelectrodes (*Chapter 3*), the constructed

amplifier should be capable of meeting the lower intrinsic noise threshold. The specific objectives for this chapter were to:

1. Design an amplification system based on design criteria identified. The amplifier should; (i) operate within a frequency band of 1 Hz to 10,000 Hz, (ii) have sufficient input impedance, (iii) remove DC offsets, (iv) be capable of amplifying biphasic μV signals within the resolution of the selected ADC and (v) have an intrinsic noise level of 45% (or less) of the microelectrodes thermal noise value.
2. Construct and assemble the amplification system into a metal box which shields from environmental electromagnetic interference.
3. Couple the amplification system with an ADC capable of simultaneous sampling from 14 channels at 2000 S s^{-1} or more.
4. Characterise the recording instrumentation (amplifier + ADC) for intrinsic noise and noise when connected to gold microelectrodes on MEA devices. Assess whether the constructed amplifier meets the 45% intrinsic noise threshold required for efficient recording from MEA devices.

4.2 Methods

4.2.1 Chemicals & Materials

Calcium chloride (CaCl_2), D-glucose, HEPES buffer, magnesium chloride (MgCl_2), potassium chloride (KCl) and sodium chloride (NaCl) were all purchased from Sigma Aldrich and used as received.

Table 4.1: Amplifier parts list

Description	Part Number	Manufacturer
Integrated circuit (IC) voltage regulator	LT3032EDE-5#PBF	Linear Technology, USA
IC operational amplifier	LT1167CS8#PBF	Linear Technology, USA
IC instrumentation amplifier	LT1678CS8#PBF	Linear Technology, USA
IC voltage reference (2.5 V)	REF5025AIDR	Texas Instruments, USA
Surface mount resistor (47 Ω)	RC1608F470CS	Samsung Electro-Mechanics, USA
Surface mount resistor (470 Ω)	RC1005F471CS	Samsung Electro-Mechanics, USA
Surface mount resistor (1 k Ω)	RC1005J102CS	Samsung Electro-Mechanics, USA
Surface mount resistor (10 k Ω)	RC0603F103CS	Samsung Electro-Mechanics, USA
Surface mount resistor (47 k Ω)	RC1005J473CS	Samsung Electro-Mechanics, USA
Surface mount resistor (220 k Ω)	RC1608J224CS	Samsung Electro-Mechanics, USA

Continued on next page

Table 4.1 – continued from previous page

Description	Part Number	Manufacturer
Surface mount resistor (470 k Ω)	RC1608F474CS	Samsung Electro-Mechanics, USA
Ceramic capacitor 1000 pF, 16 V	CL05B102KO5NNNC	Samsung Electro-Mechanics, USA
Ceramic capacitor 0.1 μ F, 16 V	CL05B104KO5NNNC	Samsung Electro-Mechanics, USA
Ceramic capacitor 1 μ F, 16 V	CL05A105KO5NNNC	Samsung Electro-Mechanics, USA
Ceramic capacitor 4.7 μ F, 16 V	CL21B475KOFNNNE	Samsung Electro-Mechanics, USA
Ceramic capacitor 10 μ F, 16 V	CL21B106KOQNNNEC	Samsung Electro-Mechanics, USA

4.2.2 Amplifier Design

The amplifier circuits were designed using Altium Designer and manufactured at CircuitLabs (Auckland, New Zealand). Printed through hole (PTH) boards were constructed with a thickness of 1.6 mm and a Cu weight of 1 oz. A green solder mask was applied on the top and bottom of the boards for protection against oxidation and prevention of solder bridges forming between solder pads. Each board consisted of 8 channels and empty areas on the boards were occupied by metal veneers which served as the ground plane — this was done to reduce interference from environmental electromagnetic noise. The boards were then assembled and tested in-house.

4.2.2.1 Power Supply

A 9 V battery was used as a DC voltage source with the positive terminal labelled V_{cc} and the negative terminal connected to ground (GND). V_{cc} and GND were decoupled using a 10 μF capacitor (C1) to filter out voltage spikes from the DC power source. An ultra-low noise, linear regulator (LT3042) (Linear Technology, USA) was used to set the supply voltage for the circuit at +5 V (*Figure 4.1A*). The LT3042 uses a current reference to set the output voltage, this reduces noise levels which result from voltage referencing in conventional linear regulators [133]. An output voltage of +5 V at the OUT pin was set by a 50 k Ω resistor (R5) at the SET pin, which can be calculated via $V_{SET} = I_{SET}R_{SET}$. Where V_{SET} is the desired output voltage, I_{SET} is the source current of the SET pin (100 μA) and R_{SET} is the value of the resistor used [133]. The +5 V output from the linear regulator is again decoupled to GND using a 4.7 μF capacitor (C4) - stabilising power supply to the circuit (as recommended by the manufacturer).

4.2.2.2 Reference Voltage

A mid point reference voltage (REF) was used to create the 2.5 V offset necessary for amplification of both negative and positive going voltages *Figure 4.1B*. REF was set using a voltage divider consisting of two 10 k Ω resistors (R7 and R8) connected in series (*Figure 4.1B*). An operational amplifier (LT1678) (Linear Technology, USA) set at a gain of 1 was used to buffer the reference voltage signal, this prevents current being drawn from the voltage divider (which can result in reference voltage fluctuations). This circuit architecture provides flexibility in the reference voltage set point through adjustment of the +5 V supply voltage, resistor values and amplifier gain.

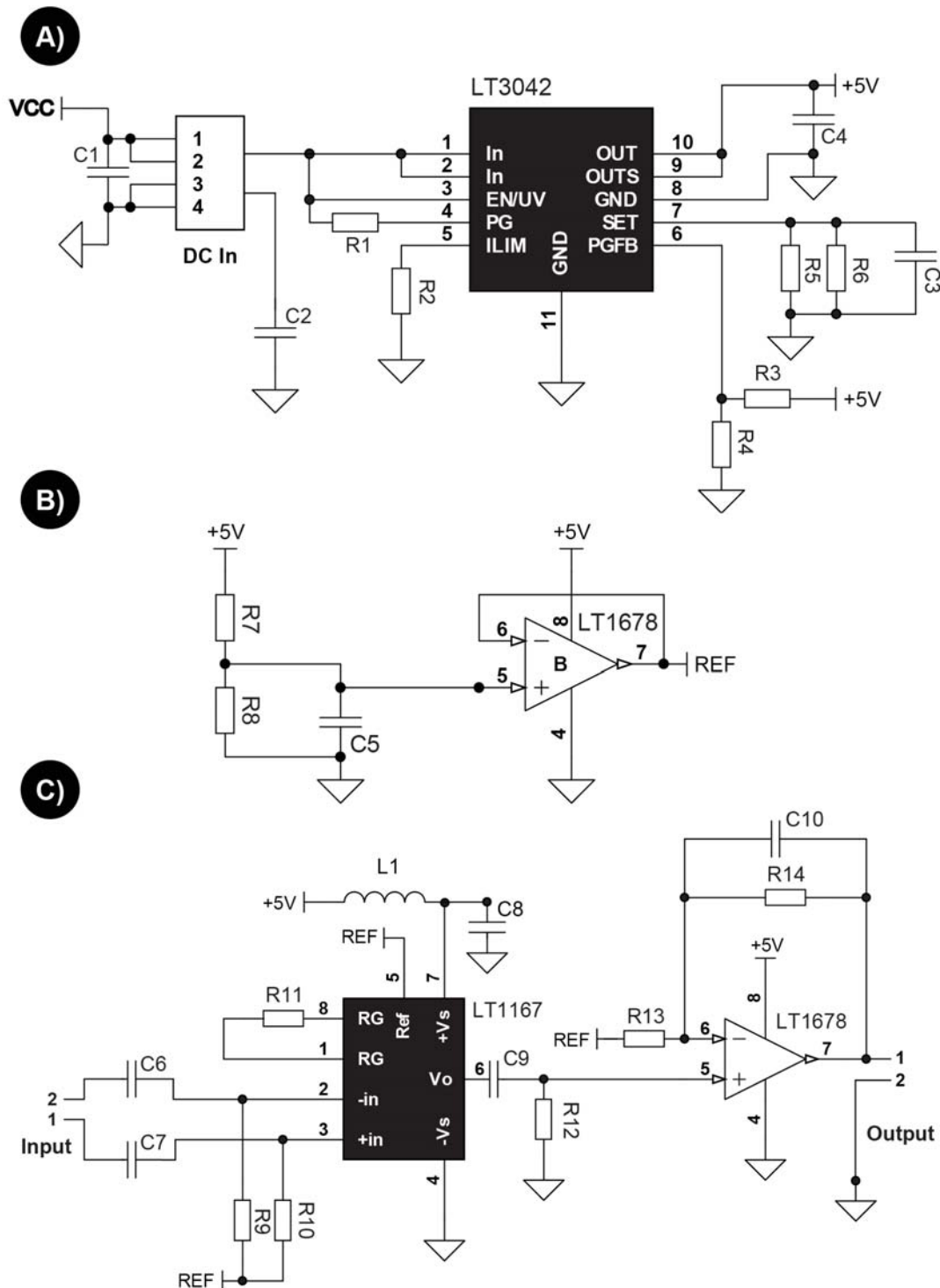


Figure 4.1: The amplifier comprised A) a power supply circuit which generated +5 V (labelled +5V) to power the amplifiers B) a reference circuit which generated a reference output (REF) to be used at the amplifier inputs and C) the amplification circuit consisting of an instrumentation amplifier and an op amp.

4.2.2.3 Amplifier architecture

The amplifier circuit comprised two stages of amplification, the first stage being an instrumentation amplifier (LT1167) (Linear Technology, USA), and the second, a two channel operational amplifier (LT1678) (Linear Technology, USA). Signals from the MEA microelectrodes were connected to the circuit board via a two pin header (labelled input), with 1 corresponding to the non-inverting input and 2 corresponding to the inverting input (*Figure 4.1C*). Inverting and non-inverting inputs were AC coupled using C6/R9 and C7/R10, respectively — this meant DC signals were filtered with a high pass cut off frequency set at 7 Hz. R9 and R10 were also essential as discharge paths for input bias currents — this stops capacitor charging at C6 and C10 and subsequently prevents voltage bias drifts at the input which can lead to errors and amplifier saturation. LT1167 instrumentation amplifier was chosen at the first stage of amplification due to its low noise operation ($7.5 \text{ nV}/\sqrt{\text{Hz}}$ at 1000 Hz), high common mode rejection ratio (125 dB at a gain of 100x), low input bias current and high input impedance (200 G Ω) which allows the use of high impedance sources without additional offset voltage errors. The high common mode rejection ratio ensures that the desired differential signal is amplified and unwanted common mode signals are attenuated. The +5 V power source from the linear regulator was used at the positive rail of the amplifier and the negative rail was tied to GND. An inductor (L1) was connected in series with the positive rail, alongside a decoupling capacitor (C8) — this was used as a strategy to further reduce noise at the supply line. A single resistor (R11, 500 Ω) set the gain at 99.8 according to *Equation 4.1*:

$$G = \left(\frac{49.4k\Omega}{R_G} \right) + 1 \quad (4.1)$$

Where R_G is the value of resistor used in $k\Omega$ and G is the gain. The common

mode voltage is removed from the original signal by the instrumentation amplifier and results in a single-ended output voltage referenced to the voltage on the REF pin (2.5 V). A second high pass filter after the first stage of amplification was used to further filter out background biological noise [40] with a cut-off frequency set at 15.9 Hz through C9/R12. The signal is then amplified at a second stage with reference to 2.5 V using the operational amplifier (LT1678) with gain set at 20 via a non-inverting feedback loop using R12/R11. An active low pass filter was also included in the design through C10 and R14 to set the upper band of the amplifier. Output signals were connected to female RCA sockets which were accessible to the ADC input cables.

4.2.3 MEA to amplifier interface

An interface board was handmade using an experimental, pre-drilled PCB (HP9540) (JayCar Electronics, NZ) (*Figure 4.2B*). Input to the board consisted of two 8-pin, double row female headers which were positioned to connect onto the male headers present on the MEA slides. Output from the board comprised 14x 2-pin male headers with each pair consisting of a pin tied to the board input (addressing one microelectrode on the MEA) and the other tied to a common Ag/AgCl reference immersed in solution. Two core cables were used between the interface board and amplifier front end where one core connected between the microelectrode and non-inverting input, and the other between the common Ag/AgCl reference and inverting input.

4.2.3.1 Shielding

The amplifiers were fit into an aluminium box to shield the boards from electromagnetic noise. Inputs to the amplifier were carried through a 2-core cable from the interface board to the amplifier through the aluminium shield. Holes

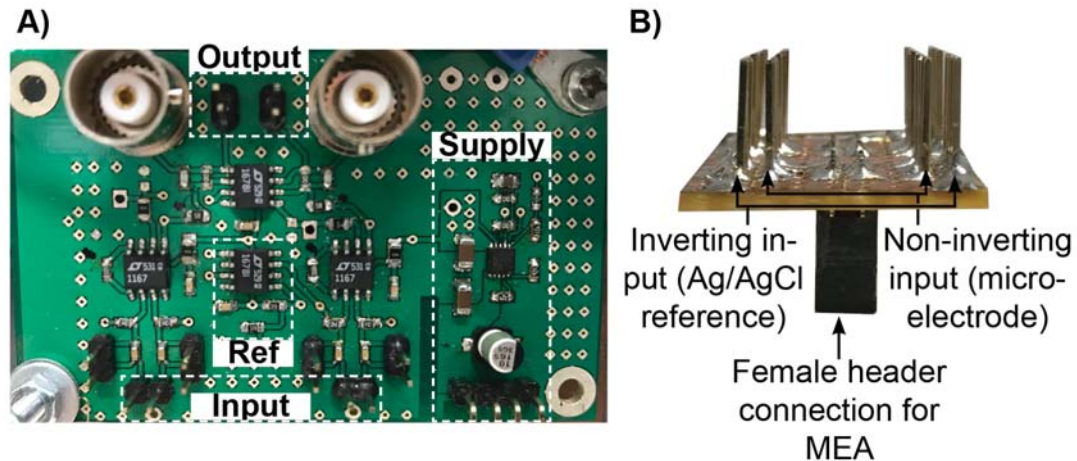


Figure 4.2: Photographs of the A) amplifier circuit and B) MEA to amplifier interface.

on the side were drilled and output RCA connectors were fitted into these holes to allow for connection between amplifier output and the ADC through RCA cables.

4.2.4 Acquisition System Design

ADCs capable of simultaneous sampling at a rate sufficient for neuronal action potentials were needed for digitising the amplified output signals. Two X series USB data acquisition systems were purchased from National Instruments (USB-6356) (National Instruments, USA). These devices comprised 8 simultaneous analog inputs with a maximum sampling rate of 1.25 MS s^{-1} per channel at 16-bit resolution, making them compatible for recording neuronal signals. Programmable resolution ranges were available from -1 to 1 V to a maximum of -10 to 10 V with absolute accuracy ranging from $291 \mu\text{V}$ to $2498 \mu\text{V}$, respectively.

Custom software was designed in LabVIEW (National Instruments, USA) to control data acquisition and logging from the two ADC devices. The program was designed to fulfil the following criteria:

1. Simultaneously acquire, display and log data during its operation.
 - (a) Acquisition and logging settings should be controlled by the user using a dialog box (or similar). Settings to be controlled should include hardware reference(s), the sampling rate, analog input resolution and a file path for logging.
 - (b) The logging file format should contain the digitised data, channel details and the sampling rate at which data was acquired.
 - (c) Data display should be in the form of multiple waveform charts (14 or more), each displaying data from individual channels on the ADC.
2. Be capable of sharing a master clock between two or more ADC's to ensure simultaneous acquisition across all devices.
3. Contain digital I/O settings to allow for control of external devices such as an external stimulator.
4. Be capable of responding to user input while data acquisition, display and logging functions are carried out. For example, pushing a trigger button to initiate an external stimulator.

To fulfil design these criteria, the software would require parallel operation of multiple sections of code to simultaneously acquire, visualise and log data whilst also responding to user input. A Continuous Measurement and Logging sample project which utilised producer/consumer architecture in the form of a queued message handler (QMH) was modified to suit our purposes. The QMH allows for parallel operation of multiple sections of code (loops) meaning that the program is responsive to user input whilst a process is running, such as data acquisition. The program was designed to executes five loops in parallel to enable a responsive user interface environment whilst data acquisition and logging were carried out. The five loops used comprised (i) a user interface event loop which responds to front panel (section where the user interacts with) events

and produces messages for (*Figure 4.3A*), (ii) a message handling loop (*Figure 4.3B*). The message handling loop then passes on commands to (iii) acquisition (*Figure 4.3C*) and (iv) logging loops (*Figure 4.3D*) which acquire and log data, respectively. The acquisition loop is a message handler which controls hardware resources (USB-6356) to acquire data using DAQmx subVI's. The acquired data is passed onto the logging loop, for data logging, as well as a (v) data display loop which streams the sampled data to an appropriate waveform chart on the front panel in real-time (*Figure 4.3E*). The general architecture of this program can be visualised through *Figure 4.4*.

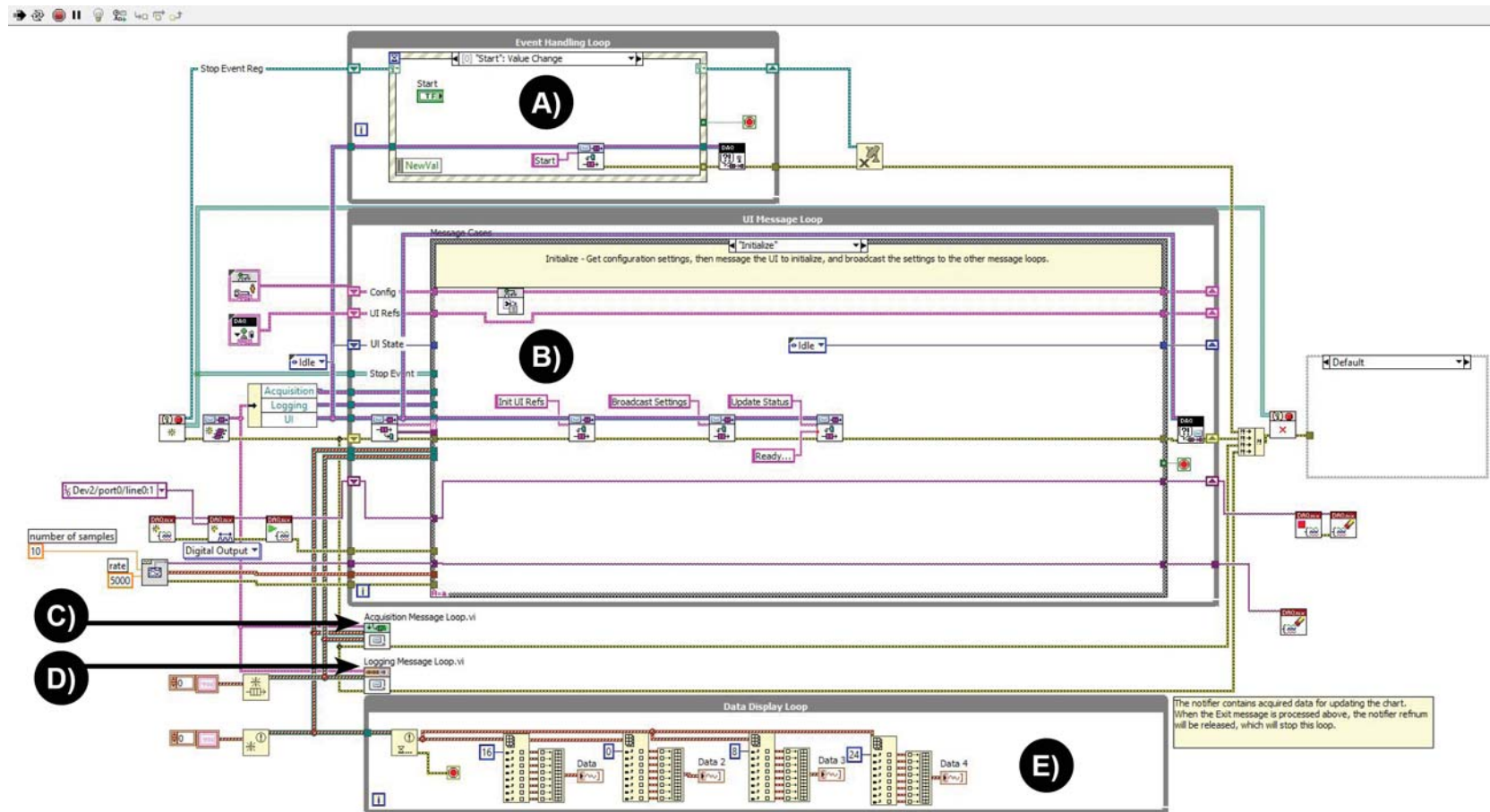


Figure 4.3: Block diagram of the data acquisition program showing 5 loops which operate in parallel. A) User interface event loop, B) User interface message handling loop, C) Acquisition loop, D) Logging loop and E) Data display loop.

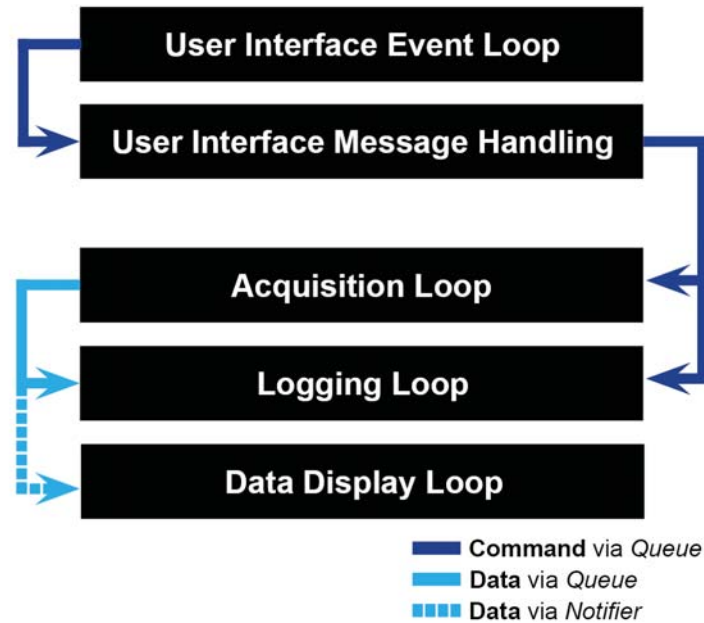


Figure 4.4: General architecture of the LabVIEW program.

Messages between loops and data to be logged were transmitted using queues due to its lossless nature. In contrast, a notifier was used to pass acquired data to the data display loop — although this method of data transfer is susceptible to data loss, the function of the data display loop is to give the user an indication of the waveform status. Therefore, a robust data transfer method is not needed.

4.2.4.1 Synchronisation of ADCs

In order to achieve simultaneous sampling between the two ADC's, start and sampling clocks from a 'master' ADC were shared with the 'slave' ADC (*Figure 4.5*). This had to be done both in software and through a physical connection between the devices. In software, the master sampling clock and start trigger were routed to programmable function interface (PFI) lines 9 and 8, respectively, using the DAQmx Export Signal subVI (*Figure 4.5A & B*). The clock and trigger on line 9 and 8 were then physically connected to PFI line 12 and 11 on the slave device, this meant that the clock and trigger of the master could be accessed by the respective PFI line on the slave. The sample clock and start trigger sources were then selected as PFI line 12 and 11 on the slave device

through DAQmx Timing and Trigger subVI's, respectively (*Figure 4.5C & D*). Finally, a flat sequence structure (*Figure 4.5E*) was used to enable the slave ADC before the master, to ensure it is ready to receive the sample clock and trigger as they come in. The result of this was that the slave device started at the same time and with the same timing as the master device, synchronising the two.

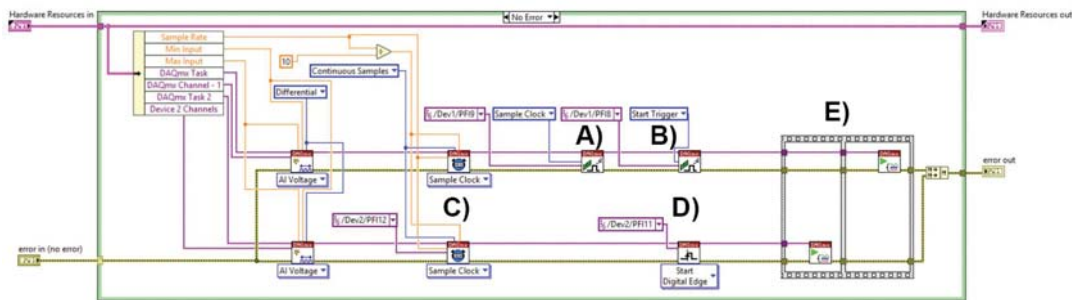


Figure 4.5: Block diagram for the synchronisation of two USB 6356 ADC's. The A) sample clock and B) start trigger of device 1 were exported to PFI lines 9 and 8, respectively, using DAQmx export signal subVI. Device 2' C) sample clock source was configured to run off device 1' sample clock which was routed to PFI line 12 using a physical connection. The start trigger from device 1 was routed to PFI line 11 and this was used as the D) start trigger for device 2. A E) flat sequence structure was used to enable device 2 first so that it could receive the clocks from device 1.

4.2.4.2 Digital I/O

A digital line on one of the ADC devices was utilised to send trigger signals to an external stimulator generator. The trigger signal was generated by first selecting the line to be used then pushing a boolean named 'trigger'. A user event was generated upon value change of the boolean button which sent a message to the user interface loop to open the trigger case. The trigger case contained DAQmx subVI's which switched the selected port state to high (1) followed by a 100 ms wait period, then returned the port state to its resting low value (0) (*Figure 4.6*).

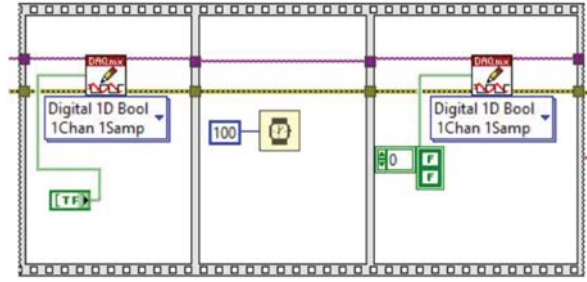


Figure 4.6: Block diagram for the generation of trigger signals to external devices from the program.

4.2.5 Intrinsic Noise Measurements

Intrinsic noise of the amplifier was measured by directly shorting the inverting and non-inverting inputs with copper wire. The ADC was used to sample amplifier output voltage at a sampling rate of 20 kS s^{-1} . A Fast Fourier Transform (FFT), utilising a Hanning window function, was performed on the measured output voltage to calculate the discrete Fourier Transform (DFT) of the signal between 1 Hz and 10,000 Hz (OriginPro graphing software).

4.2.5.1 RMS Noise Assessment

A python script was written in Jupyter Notebook to import TDMS data and perform root mean squared (RMS) analysis on the recorded noise levels. The script utilises the `nptdms` package to import National Instruments .TDMS file format. Data channels of interest were defined by `tdms_file.object` and `channel` commands of the `nptdms` package. A `detrend` function was performed on the imported data vector prior to RMS calculation, this was done to remove the 2.5 V offset. The RMS function was defined as `qmean` and returned the root mean square of the data vector, according to *Equation 4.2*. Peak to peak (V_{p-p}) values were then calculated by multiplying the resulting RMS value by 6.6 to obtain an estimate within a 99.99% confidence interval.

$$V_{RMS} = \sqrt{\frac{\sum_{i=1}^n V_i^2}{n}} \quad (4.2)$$

```

#import packages
    import nptdms
    import scipy
    from scipy import signal
    from nptdms import TdmsFile
    import matplotlib.pyplot as plt
    import numpy as np
    import scipy.fftpack
    import math

#Define Amplifier Gain
    gain = 2000

#Define Vrms Calculation
    from math import sqrt
        def qmean (num):
            return sqrt(sum(n*n for n in num)/len(num))

#import data from TDMS file
    tdms_file = TdmsFile("Filename")
    channel = tdms_file.object('Untitled', 'Dev1/ai2')
    data = channel.data
    time = channel.time_track()

#Remove 2.5V Offset
    detrend_data = signal.detrend(data)

#Perform Vrms Calculation
    Vrms = (qmean(detrend_data))/gain

```

4.2.6 Amplifier and Microelectrode Noise Assessment

Noise assessment of the amplifier boards during expected use was carried out by connecting the inputs to a bare gold microelectrode on the MEA device through the interface board. The microelectrodes were immersed in Tyrode's solution to mimic a physiologically relevant environment. Noise spectra and RMS voltage calculations were performed as detailed in *Section 4.2.5*.

4.2.6.1 Tyrode's Solution

Tyrode' solution is commonly used in electrophysiological recordings [134] and was utilised to mimic the end application of the amplification system. The solution comprised 119 mM NaCl, 2.5 mM KCl, 2 mM CaCl₂, 2 mM MgCl₂, 25 mM HEPES buffer and 30 mM D-glucose. Typically, 100 mL of fresh solution was made weekly using milliQ water, with the pH adjusted to 7.4 using 1 M NaOH.

4.3 Results

4.3.1 Amplifier Performance

Amplifier boards were successfully manufactured and assembled. An assessment of amplifier performance was carried out by shorting the inverting and non-inverting inputs to obtain intrinsic noise levels. Since the amplifier output was sampled using an ADC, noise contributions from the ADC had to be considered. According to the national instruments data sheet for USB-6356 ADCs, their contribution of noise equates to $1.5 \mu V_{RMS}$ at the range used (-10 V to 10 V). The presented values for **intrinsic** amplifier performance subtract this noise contribution from the total RMS value (comprising amplifier noise + ADC noise) through *Equation 4.3* to yield the amplifiers contribution to noise.

$$V_{RMS(Amp)} = \sqrt{V_{RMS(total)}^2 - V_{RMS(ADC)}^2} \quad (4.3)$$

Table 4.2: The calculated % of amplifier noise as compared to microelectrode thermal noise values taken from *Chapter 3*. The target % value was < 45%.

Coating	Thermal Noise (μV_{p-p})	Intrinsic Amplifier Noise (Input Shorted) (μV_{p-p})	% of Microelectrode Thermal Noise
Gold	34.7	9.9	28.5%
Conventional PEDOT/PSS (637 mC cm ⁻²)	12.1	9.9	81.8%
Macroporous PEDOT/PSS (637 mC cm ⁻²)	10.5	9.9	94.2%

The intrinsic amplifier RMS noise was found to be $1.5 \mu V_{RMS}$ and peak to peak values were $9.9 \mu V_{p-p}$. *Table 4.2* displays thermal noise values for gold and PEDOT/PSS coatings deposited at 637 mC cm⁻² calculated from *Chapter 3*. The

target intrinsic amplifier noise level was $< 45\%$ of the microelectrode thermal noise component. The constructed amplifier meets requirements assuming a gold microelectrode were to be used, however, it fails to meet requirements when PEDOT/PSS coatings are applied.

Figure 4.7A represents a digitised signal, from the ADC, of the amplifier when the inverting and non-inverting inputs were shorted. A close inspection reveals several issues, the first being that the offset REF voltage is not at the expected 2.50 V, rather, it was sitting slightly lower at approximately 2.46 V.

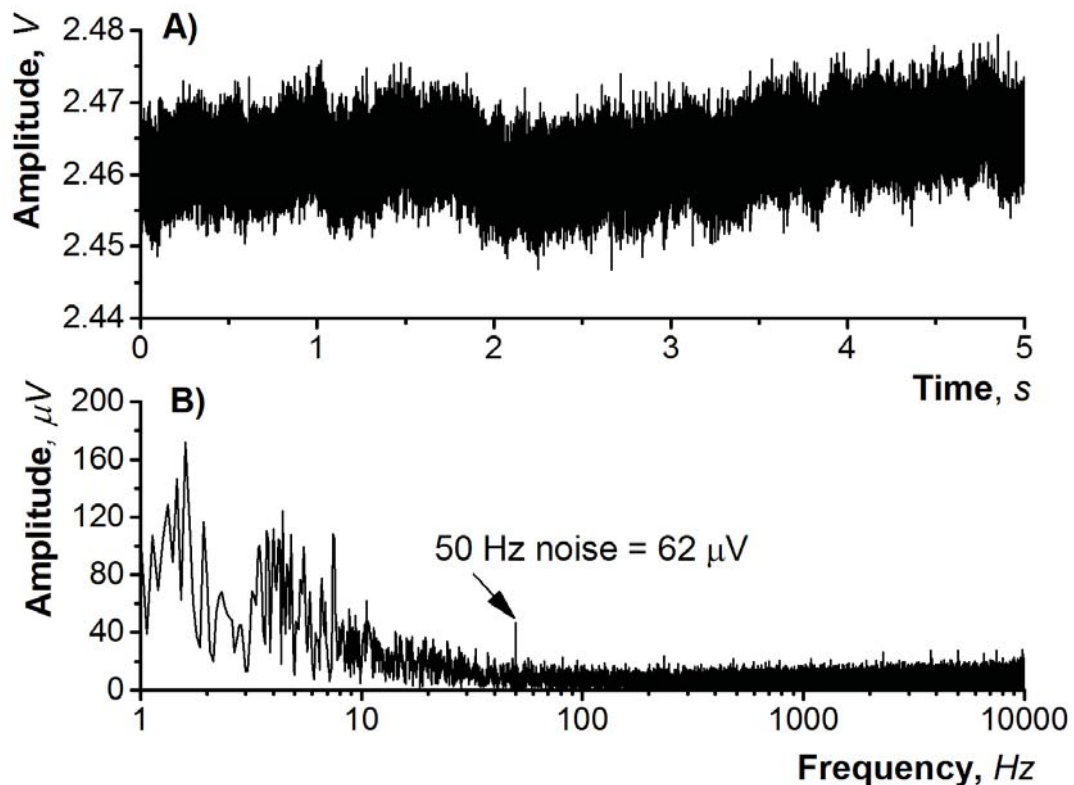


Figure 4.7: Assessment of intrinsic noise levels of the amplifier were carried out by A) sampling data at the output of the amplifier when the inverting and non-inverting inputs were shorted with copper wire. B) An FFT analysis was done using a Hanning window function to identify frequency bands with large noise components.

The second observation is that the baseline looks slightly unstable, with random fluctuations apparent. These effects are likely due to the reference voltage circuit architecture (Figure 4.1B). Since a voltage divider was used to obtain 2.5 V, the input voltage into the divider network becomes a large determinant in the

output reference voltage. Therefore, if fluctuations occur in the supply voltage, these will become apparent within the baseline of the amplifier. FFT analysis of the intrinsic noise waveform highlights the 10 kHz bandwidth of the amplifier and indicates a large amplitude of noise in the lower frequency band, (*Figure 4.7A*) with a prominent peak at 50 Hz at an amplitude of $62 \mu\text{V}$. This 50 Hz peak is likely a result of power line electromagnetic interference and suggests poor shielding at the amplifier front end.

An assessment of system noise when the amplifier inputs were connected to gold microelectrodes on the MEA (immersed in Tyrode's solution) through the interface board revealed larger peak to peak values (*Figure 4.8A*). The V_{RMS} increased 5 fold from the original intrinsic amplifier noise level to $10.1 \pm 0.8 \mu\text{V}$, with a calculated peak to peak value of $66.9 \pm 5.3 \mu\text{V}_{p-p}$ ($n = 3$). FFT analysis of the noise waveform (*Figure 4.8B*) showed a similar low frequency noise component but at a higher amplitude, with the 50 Hz amplitude rising to $161 \mu\text{V}$ and a new prominent peak at 100 Hz ($443 \mu\text{V}$). The increase in noise amplitude is expected due to high impedance of gold microelectrodes (as shown in *Chapter 3*) and can be attributed to both thermal noise at the electrode and environmental power line noise. This gives two avenues of noise reduction in the system where the first involves better shielding strategies from power line noise and the second comprises decreasing microelectrode impedance (as discussed in *Chapter 3*). In an attempt to further reduce the contribution of intrinsic amplifier noise, the amplifier circuit was modified to account for the results observed. The main points of focus within the redesigned board involved an improved approach to achieving the 2.5 V offset REF and reducing low frequency noise. The reduction of noise should comprise strategies to better shield the amplifier and a more professional approach towards the hand-made interface board.

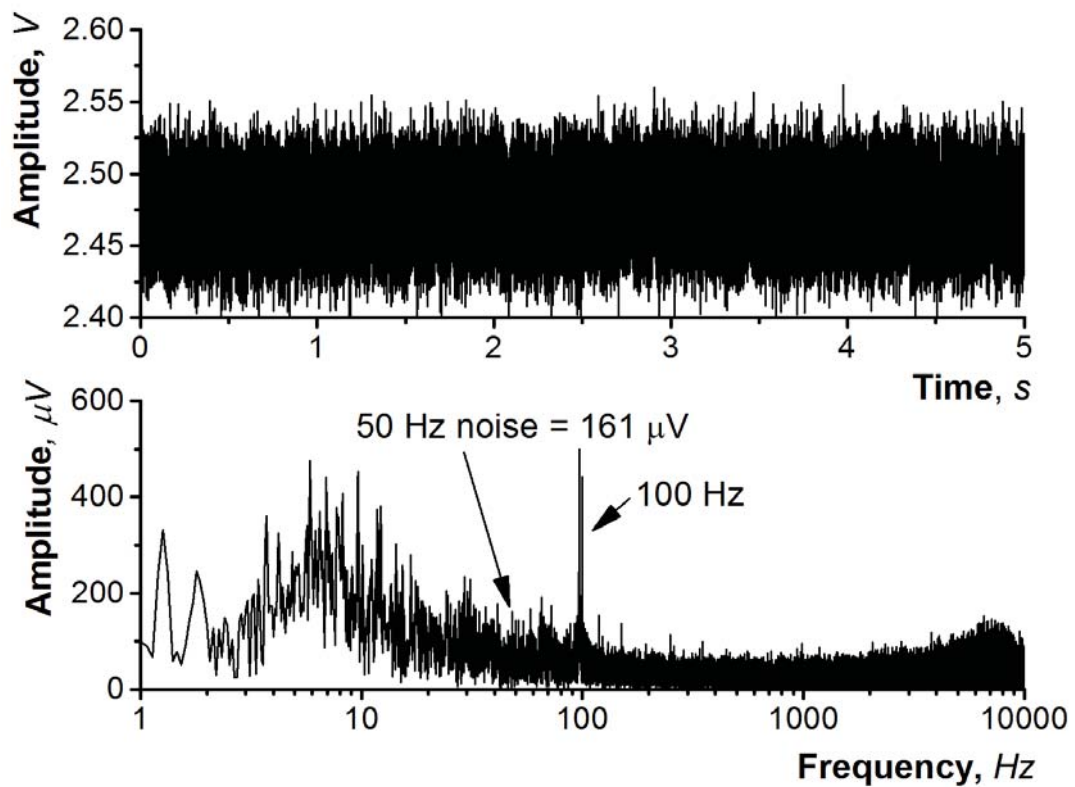


Figure 4.8: Assessment of noise levels when the amplifier is connected to gold microelectrodes on the MEA device. The microelectrodes were immersed in Tyrode's solution and A) amplifier output was sampled. B) An FFT analysis was done using a Hanning window function to identify frequency bands with large noise components. It is apparent that the majority of noise lies between 0-100 Hz with a large peak prominent at 100 Hz.

4.3.2 Modified Amplifier Architecture

The amplifier circuit was redesigned in Altium Designer and manufactured at CircuitLabs (Auckland, New Zealand) with similar specifications to the first board. The main point of difference in the second version was within the circuitry for the REF offset voltage. Rather than a voltage divider with a unity gain buffer amplifier, a low-noise ($3 \mu\text{V}_{p-p}/\text{V}$), low drift ($\pm 0.05\%$) precision voltage reference (REF5025) (Texas Instruments, USA) was used (*Figure 4.9B*). This was done to correct for fluctuations within the offset REF voltage and prevent recording errors associated with an unstable REF.

Small changes within the amplifier design consisted of lowering the high-pass cut off frequency to 0.7 Hz (through C15/R16 and C6/R17) — widening the bandwidth of the amplifier (*Figure 4.9C*). Amplifier gains were adjusted so that the instrumentation amplifier would comprise a large component of the total gain, at a value of 1000, due to its low noise operation, leaving the operational amplifier at a gain of 2.

4.3.3 Modified Interface Board

A modified interface board was designed in Altium Designer and constructed at CircuitLabs (Auckland, New Zealand) (*Figure 4.10*). Similar specifications to amplifier boards discussed above were utilised with the main difference being absence of the solder mask. The board was designed to comprise two 8 pin, double row female headers which were positioned to fit onto the male headers present on the MEA slides. Outputs from the board consisted of 14x 2-pin headers, with each pair consisting of a pin tied to a microelectrode on the MEA (connected to non-inverting input at amplifier) and the other to a common Ag/AgCl reference immersed in solution (connected to inverting input). The size of the interface board was increased to cover the length and width of the

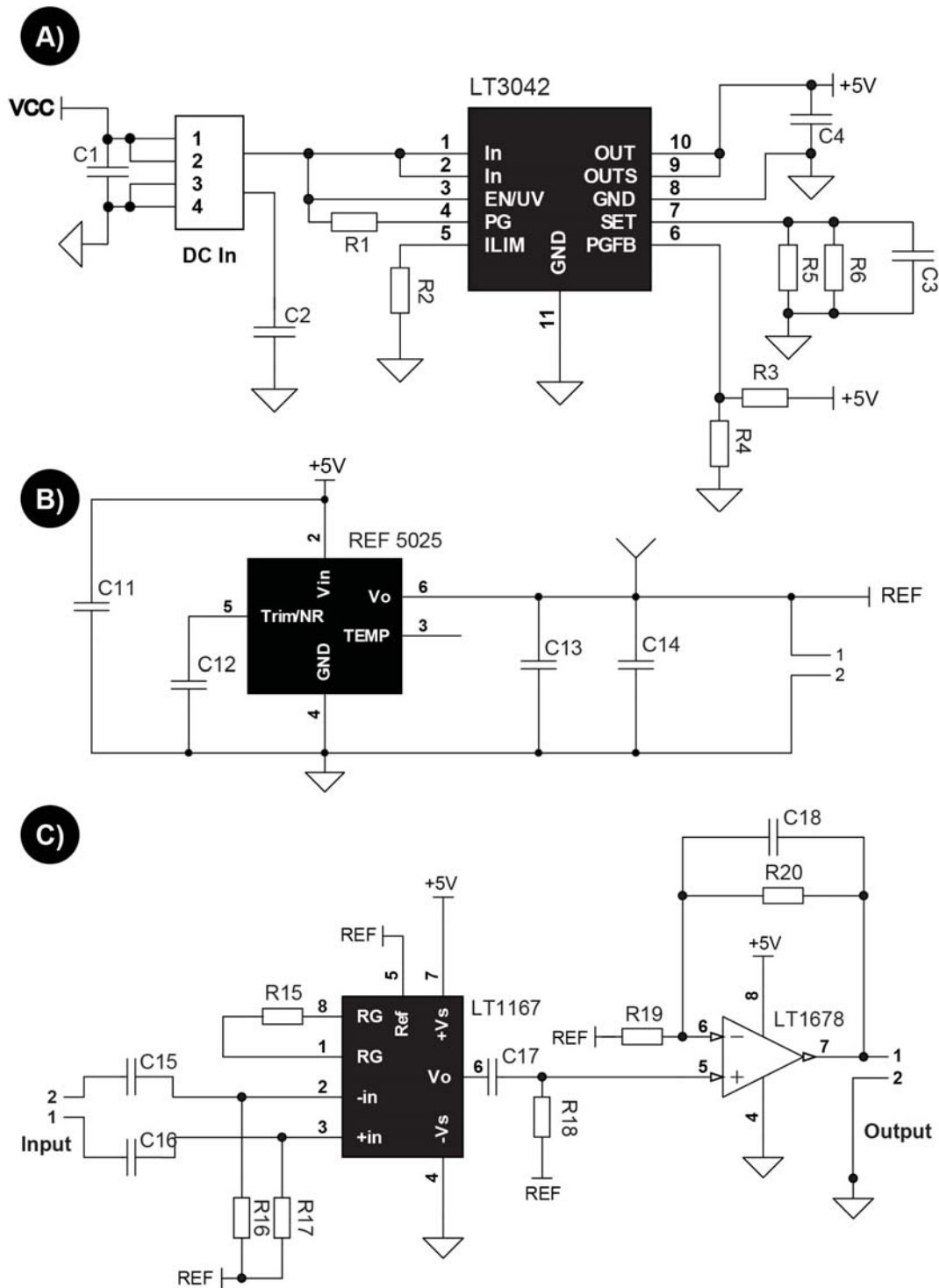


Figure 4.9: The second amplifier comprised A) a power supply circuit which generated +5 V (labelled +5V) to power the amplifiers B) a reference circuit which generated a reference output (REF) to be used at the amplifier inputs and C) the amplification circuit consisting of an instrumentation amplifier and an op amp.

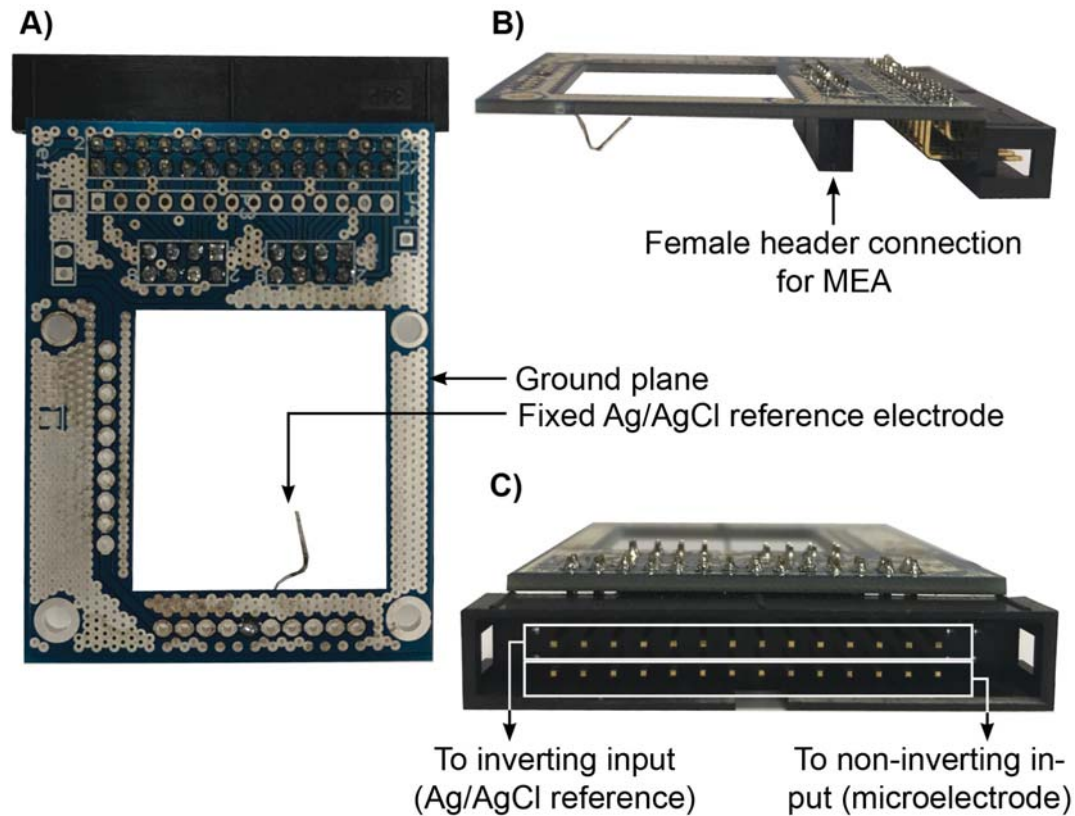


Figure 4.10: Photograph of the modified interface board showing A) top view, B) side view and C) front view.

MEA device (75 mm x 25 mm), with a window factored into the design over the MEA well to facilitate manipulation of the electrolyte solution. The added area was filled with exposed metal vanes which acted as a ground plane to shield the MEA device from environmental electromagnetic noise. The ground plane was connected to amplifier GND. Three core cables were used in this design to connect between the interface board outputs and amplifier front end. The cables comprised two cores (which connected a microelectrode and Ag/AgCl reference to non-inverting and inverting inputs, respectively), with the addition of a third shielding core comprising copper wire enclosed the other two cores. The shield was connected to the 2.5 V offset reference as a strategy to further reduce interference from environmental electromagnetic noise.

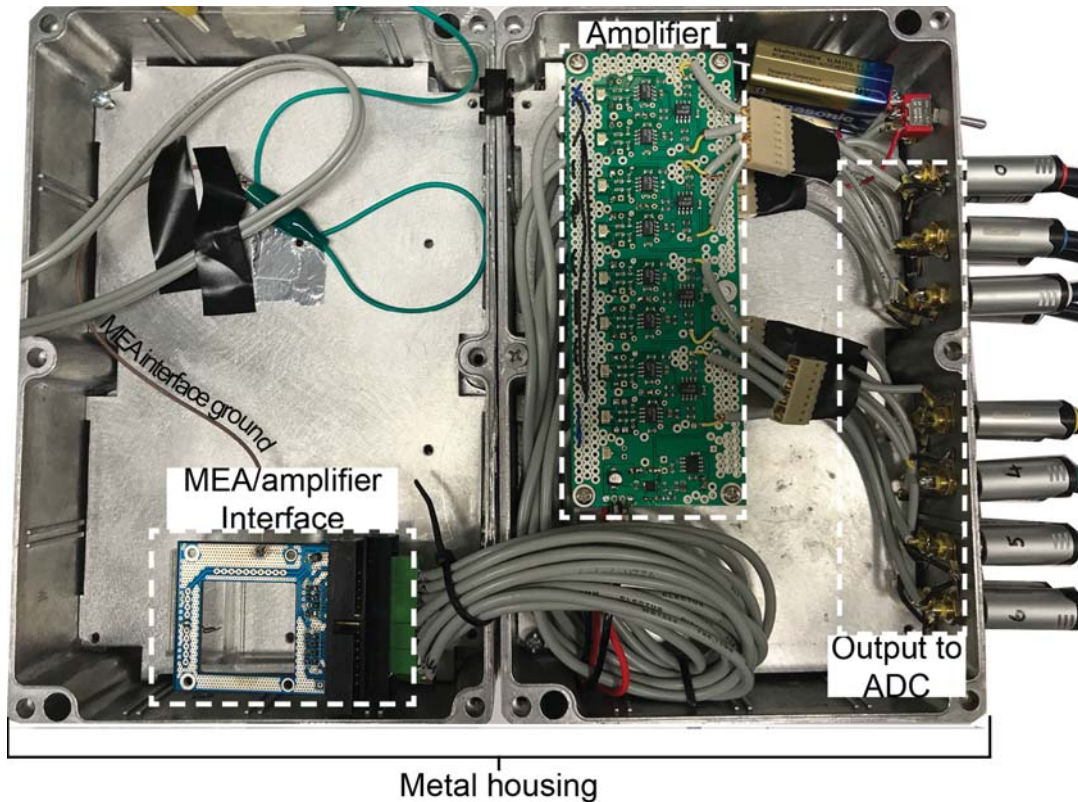


Figure 4.11: Photograph of the final amplifier set-up highlighting the MEA/amplifier interface connection, amplifier board and output connections to the ADC.

4.3.3.1 Modified Amplifier Performance

Calculated V_{RMS} and V_{p-p} values (after subtracting ADC noise contribution) of the modified amplifier were $0.7 \mu V_{RMS}$ and $4.6 \mu V_{p-p}$, respectively. Indicating a two-fold reduction in intrinsic amplifier noise. *Table 4.3* highlights the success of the modifications carried out, achieving the target of intrinsic amplifier noise being 45% of the microelectrode thermal noise for all microelectrode types.

Figure 4.12A represents a digitised signal, from the ADC, of the modified amplifier when the inverting and non-inverting inputs were shorted. A noticeable difference in the quality of the REF offset was observed with the voltage level, centred around 2.5 V, displaying a significant improvement in stability and accuracy. FFT analysis (*Figure 4.12B*) showed a significant reduction in noise amplitude at low frequencies as compared to the first design. Although the 50 Hz noise peak was still prominent, its amplitude reduced from $62 \mu V$ to $39 \mu V$.

Table 4.3: The calculated % of the modified amplifier intrinsic noise as compared to microelectrode thermal noise values taken from *Chapter 3*. The target % value was 45%.

Coating	Thermal Noise (μV_{p-p})	Intrinsic Amplifier Noise (Input Shorted) (μV_{p-p})	% of Microelectrode Thermal Noise
Gold	34.7	4.6	13.2%
Conventional PEDOT/PSS (637 mC cm^{-2})	12.1	4.6	38.0%
Macroporous PEDOT/PSS (637 mC cm^{-2})	10.5	4.6	43.8%

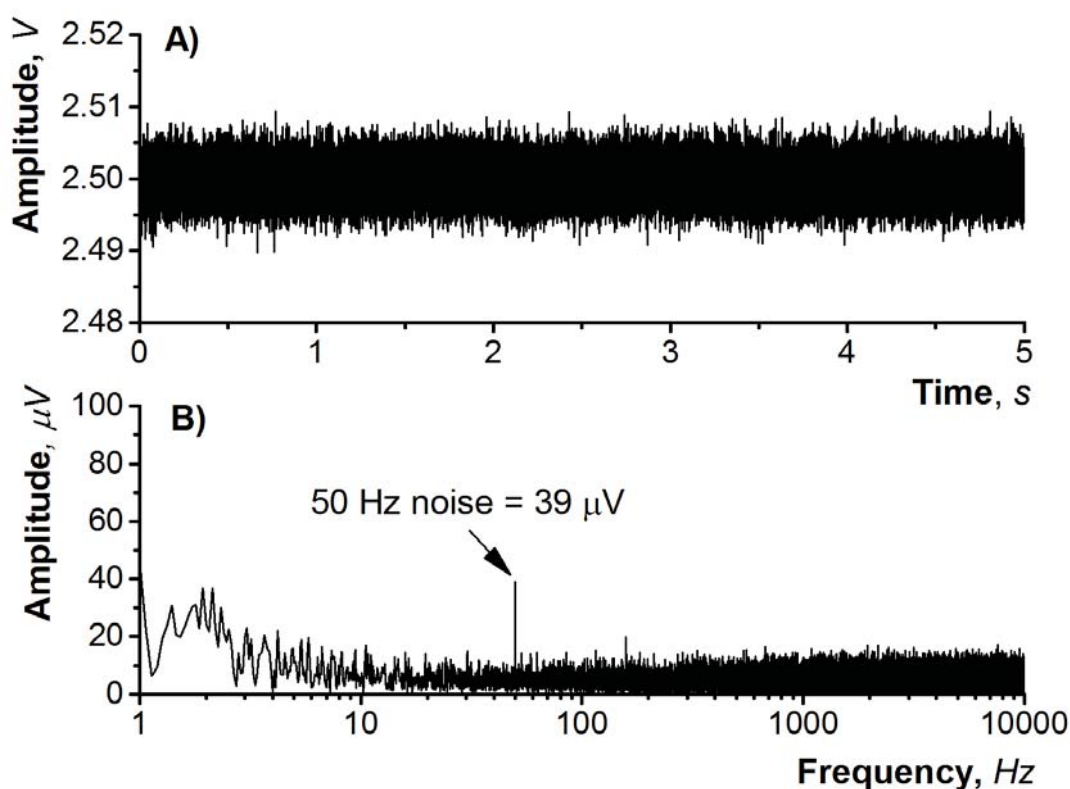


Figure 4.12: Assessment of intrinsic noise levels of the modified amplification system where A) shows sampled data at the output of the amplifier when the inverting and non-inverting inputs were shorted with copper wire. B) Represents FFT analysis using a Hanning window function to identify frequency bands with large noise components. An obvious reduction in noise amplitude was noticed in the lower frequency band, however, 50 Hz signals were still prominent.

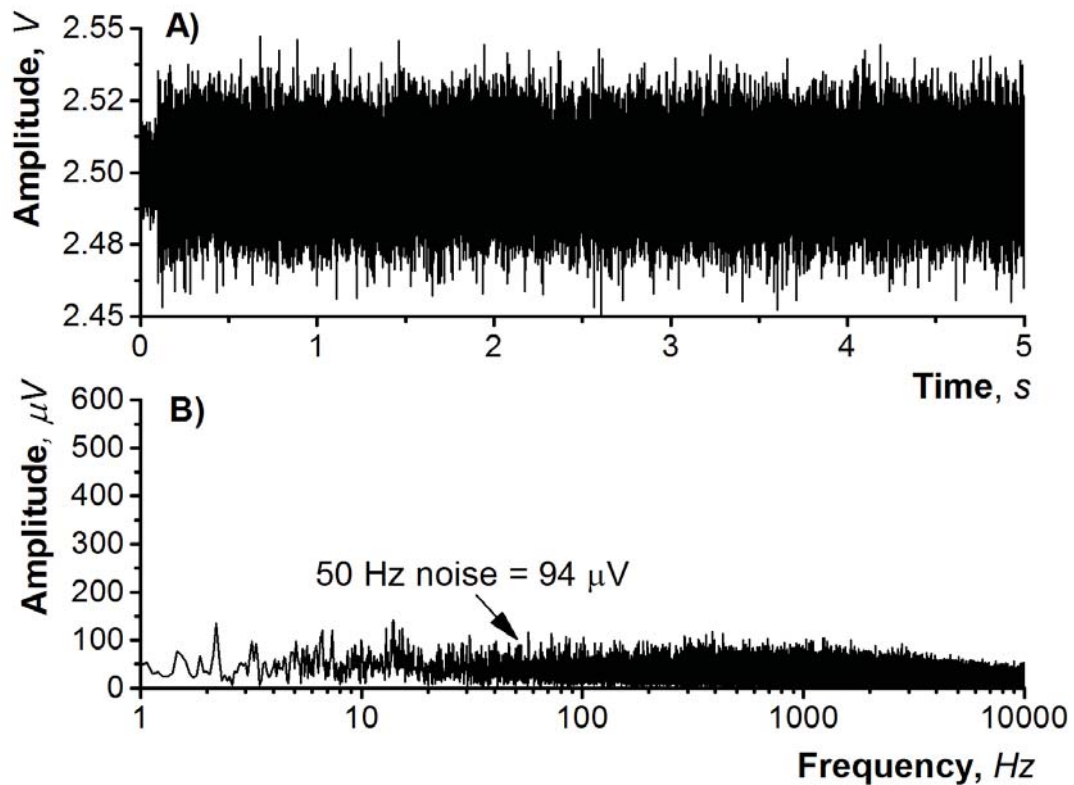


Figure 4.13: Assessment of noise levels for modified amplifier when connected to gold microelectrodes on the MEA device through neural interface board version 2. The microelectrodes were bathed in Tyrode’s solution and A) amplifier output was sampled at 20 kS s^{-1} . B) An FFT analysis was done using a Hanning window function to identify frequency bands with large noise components. The large noise signals prominent in the lower frequencies of the first amplifier can not be seen in this version.

System noise characterisation through the connection of a gold microelectrode immersed in Tyrode’s solution was then carried out to assess influence of the modified interface board on noise properties (*Figure 4.13*). Although the gold impedance values remained constant, a significant reduction ($p = 0.02$) in noise as calculated through V_{RMS} and V_{p-p} was observed at values of $6.1 \pm 0.2 \mu\text{V}$ and $40.2 \pm 1.3 \mu\text{V}$ ($n = 3$), respectively. FFT analysis (*Figure 4.13B*) revealed that the 50 Hz noise amplitude decreased from the original amplifier value of $161 \mu\text{V}$ to a value of $94 \mu\text{V}$, and the disappearance of the 100 Hz noise peak. Due to identical gold electrodes used when the two systems were tested, the improvement in noise properties can be attributed to enhanced amplifier design and shielding approaches.

Table 4.4: Summary of peak to peak values for intrinsic amplifier noise, amplifier + ADC noise and amplifier + ADC + microelectrode noise.

Amplifier	Test	Noise (μV_{p-p})
Initial Amplifier	Intrinsic amplifier noise	9.9
	Amplifier + ADC	13.9
	Amplifier + ADC + microelectrode	66.9
Modified Amplifier	Intrinsic amplifier noise	4.6
	Amplifier + ADC	8.6
	Amplifier + ADC + microelectrode	40.2

Table 4.4 summarises the findings from both amplifiers constructed, where ‘amplifier A’ refers to the first version and ‘amplifier B’ refers to the modified version.

4.3.4 Acquisition System

The waveforms shown above for noise analysis of the amplifiers were taken with the constructed LabVIEW program and USB 6356 ADC’s.

Figure 4.14 represents the front panel which the user interfaces with. It contains 4x 8 channel waveform charts side-by-side to enable visualisation of up to 36 channels simultaneously (Figure 4.14A). The bottom pane consists of boolean controls which perform various functions central to data acquisition, logging and digital I/O. A settings dialog box (Figure 4.14B) can be accessed by clicking the settings button in the general controls pane (Figure 4.14C). This dialog box contains essential hardware configurations such as the hardware references, sampling rate (maximum of $1.25 \text{ MS second}^{-1}$) and acquisition resolution (maximum of -10 to 10 V and minimum of -1 to 1 V). Synchronisation of two DAQ devices can be achieved through clicking the ‘Activate Second DAQ’ boolean — making device 1 the master device and device 2 the slave device. This is essential in order to synchronise the clocks of the two devices and maintain simultaneous

sampling. Logging configurations can also be accessed in the settings dialog box where the file path for acquired data can be set and options for triggered acquisition are available. Triggered acquisition refers to data logging when a threshold value (set in the ‘threshold’ numeric control) is met, this function can be overridden by selecting ‘always log’ or ‘force trigger’ in the settings dialog box or general controls pane, respectively. Other functions in the general controls pane include ‘Start’ and ‘Stop’ which initiate and terminate data acquisition. Digital I/O was integrated in MEA DAQ to allow for control of external devices (current generator and/or high speed camera) through a 5 V digital trigger signal. The digital controls pane (*Figure 4.14D*) allows for selection of the active trigger line as well as the ability synchronise DAQ and high speed camera start times. The ‘Stimulate’ boolean enables control of an external current generator which can be activated at anytime within the acquisition process. The status pane (*Figure 4.14E*) presents state information of the programme and allows for adjustment of the min and max Y-axis values of the display waveform charts in *Figure 4.14A*.

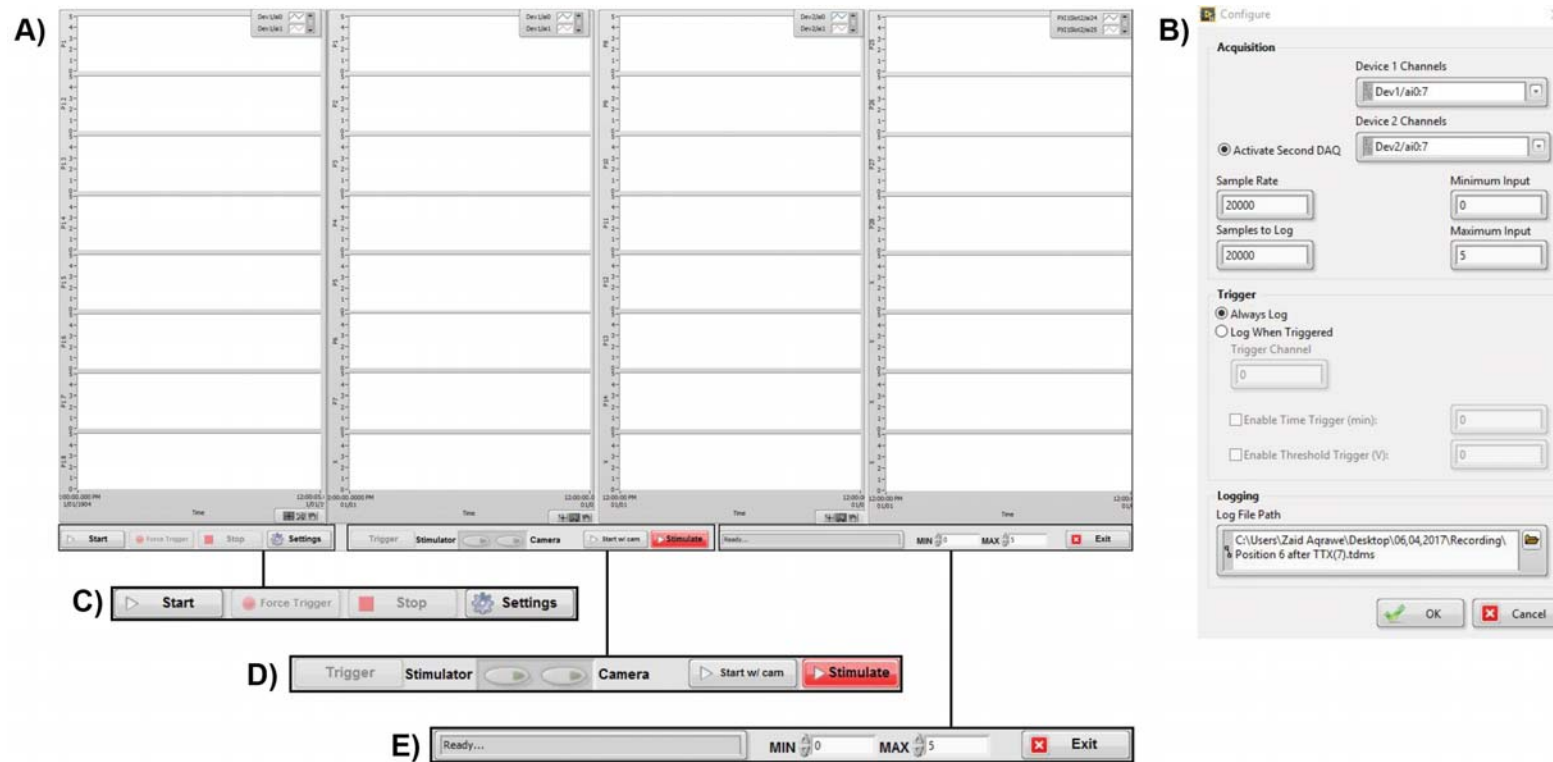


Figure 4.14: Front panel of acquisition program comprising A) waveform charts which display the acquired data in real time, B) a settings dialog box which allows for customisation of hardware used, sampling rate, number of samples to log, acquired signal resolution and trigger settings for the acquired data (file path for logged data can be specified too). The settings dialog box can be accessed through C) a boolean control on the front panel alongside other general controls which start/stop acquisition and force a trigger event to begin logging. A digital control panel D) allows for digital I/O to an external current generator for stimulation and a high speed camera for synchronised event triggering. The status of the programme is detailed in E) a status bar alongside numeric controls which define the y-axis scale of the waveform charts and a boolean control to terminate the programme.

4.4 Conclusions

An amplifier was successfully designed and coupled with an ADC from National Instruments to enable low noise amplification of neuronal signals. The first amplifier design operated within the required 10 kHz bandwidth, had a gain of 2000, removed DC voltages and had a 2.5 V offset voltage to allow for amplification of both positive and negative going signals. It had an intrinsic noise value of $9.9 \mu\text{V}_{p-p}$ but did not meet the required threshold of 45% of the thermal noise for all microelectrode types. Furthermore, the first design displayed an unstable offset voltage (REF) and it was made apparent that this was caused by the voltage divider network employed to set this voltage. FFT analysis of the first amplifier revealed large noise amplitudes in the low frequency region, with a distinct peak at 50 Hz suggesting poor shielding at the amplifier front end. The redesigned amplifier accounted for these observations and changes were made to the REF voltage circuitry and MEA/amplifier interface. These changes resulted in a two fold reduction of intrinsic noise, from $9.9 \mu\text{V}_{p-p}$ to $4.6 \mu\text{V}_{p-p}$. This new intrinsic noise level was well within the target of $< 45\%$ the microelectrode thermal noise for all microelectrode materials. Drastic reductions in FFT noise amplitudes across all frequencies were noticed and a stable offset voltage was observed. A program to acquire data from the ADC was also successfully constructed. The ADC used was capable of meeting sample rate requirements for neuronal action potentials, fulfilling sampling criteria set forth in the objectives.

This system was then used in *Chapter 5* to characterise *in-vitro* recording performance and stimulation efficacy of unmodified gold, conventional PEDOT/PSS and macroporous PEDOT/PSS.

Chapter 5

The Influence of Conventional and Macroporous Conducting Polymers on Neuronal Recording Performance & Stimulation Efficacy

5.1 Introduction

This chapter investigates the *in-vitro* recording performance and stimulation efficacy of unmodified gold, conventional PEDOT/PSS and macroporous PEDOT/PSS coatings developed in *Chapter 3*.

Recording neuronal activity through MEAs can be broken up into three segments to better understand the processes at work, (i) neuronal signal generation, (ii) signal propagation and (iii) signal transduction. In neuronal recordings, electrical signals (i.e. action potentials) are generated by neurons and involve the movement of ions across the cell membrane (mainly sodium and potassium) [23, 24]. This process creates a localised change in ionic concentrations which propagate to an electrode contact throughout an electrolyte, as described by the volume conduction theory (*Equation 5.1*) [25–27].

$$V(x, y, z) = \frac{I}{4\pi\sigma\sqrt{(x-x')^2 + (y-y')^2 + (z-z')^2}} \quad (5.1)$$

Where I is the transmembrane current source (action potential located at x' , y' , z') and V is the potential recorded at an electrode (located at x , y , z) in an infinite volume conductor with homogenous extracellular electrical conductivity (σ). The recording performance of microelectrodes is typically denoted as a signal to noise ratio (SNR) and calculated through *Equation 5.2*.

$$SNR(dB) = 20\log_{10}\frac{Sig_{p-p}}{Noise_{p-p}} \quad (5.2)$$

The noise floor ($Noise_{p-p}$) can be characterised simply and is usually taken as the mean peak to peak value of areas with no neuronal activity. The main determinants of noise in microelectrode arrays devices are (i) biological noise ($V_{RMS(bio)}$); which originate from action potentials of distant cells and ionic

activity associated with subthreshold potentials of nearby cells [37,135–138], (ii) electrode/electrolyte interface noise ($V_{RMS(th)}$); which is largely determined by thermal noise of the microelectrode (as investigated in *Chapter 3*) and is directly proportional to its impedance (*Equation 3.1*) [139,140] and (iii) instrumentation noise ($V_{RMS(inst)}$); introduced through the devices used to amplify and digitise the neuronal signals (as investigated in *Chapter 4*) [37]. The root mean square (RMS) values of these noise sources can be added in quadrature to estimate the total noise ($V_{RMS(tot)}$) performance of a MEA system through *Equation 5.3*:

$$V_{RMS(tot)} = \sqrt{V_{RMS(bio)}^2 + V_{RMS(th)}^2 + V_{RMS(inst)}^2} \quad (5.3)$$

The signal amplitude (Sig_{p-p}) is usually defined as the average peak to peak value of all recorded action potentials related to one neuron (also referred to as a ‘unit’). The recorded amplitude is dependent on (i) microelectrode impedance, which predicts the magnitude of signal lost to ground through shunt pathways [46] and (ii) the distance of the neuron from the microelectrode contact, according to *Equation 5.1*.

Stimulation efficacy describes the ability of a microelectrode to invoke neuronal activity following charge injection. The goal of stimulation through MEA devices is to safely and effectively stimulate neuronal cells with single unit spatial resolution. Safe stimulation refers to parameters which do not result in irreversible faradaic reactions, such as the hydrolysis of water, that are damaging to both the microelectrode and the surrounding neuronal cells [34,62,141,142]. A common safety range, termed the ‘water window’, is used to set the limits of stimulation amplitudes between 0.6 V and -0.9 V vs Ag/AgCl [34]. Efficacious stimulation refers to the ability of a microelectrode to illicit direct neuronal activity in response to a safe stimulation pulse [34,43]. A number of considerations must be made to achieve safe and efficacious stimulation; (i) the type of

electrode material and (ii) stimulating waveform characteristics.

Low impedance microelectrodes reduce the charge injection requirements to meet neuronal activation thresholds, which in turn reduces the risk of damaging irreversible faradaic reactions [6, 34, 44, 47]. Ohm's law (*Equation 5.4*) can be used to simplify the relationship between stimulating electrode safety/efficacy and impedance.

$$V = I|Z| \tag{5.4}$$

Where the voltage (V) created at the electrode/electrolyte interface is directly proportional to the stimulating current amplitude (I) and the microelectrodes impedance magnitude ($|Z|$) at the same frequency as the stimulating pulse. *Figure 5.1* lists commonly used waveforms for neuronal stimulation and their associated safety/efficacy profile. From this, it is apparent that a balance between microelectrode and waveform characteristics are required to achieve safe and efficacious neuronal stimulation.

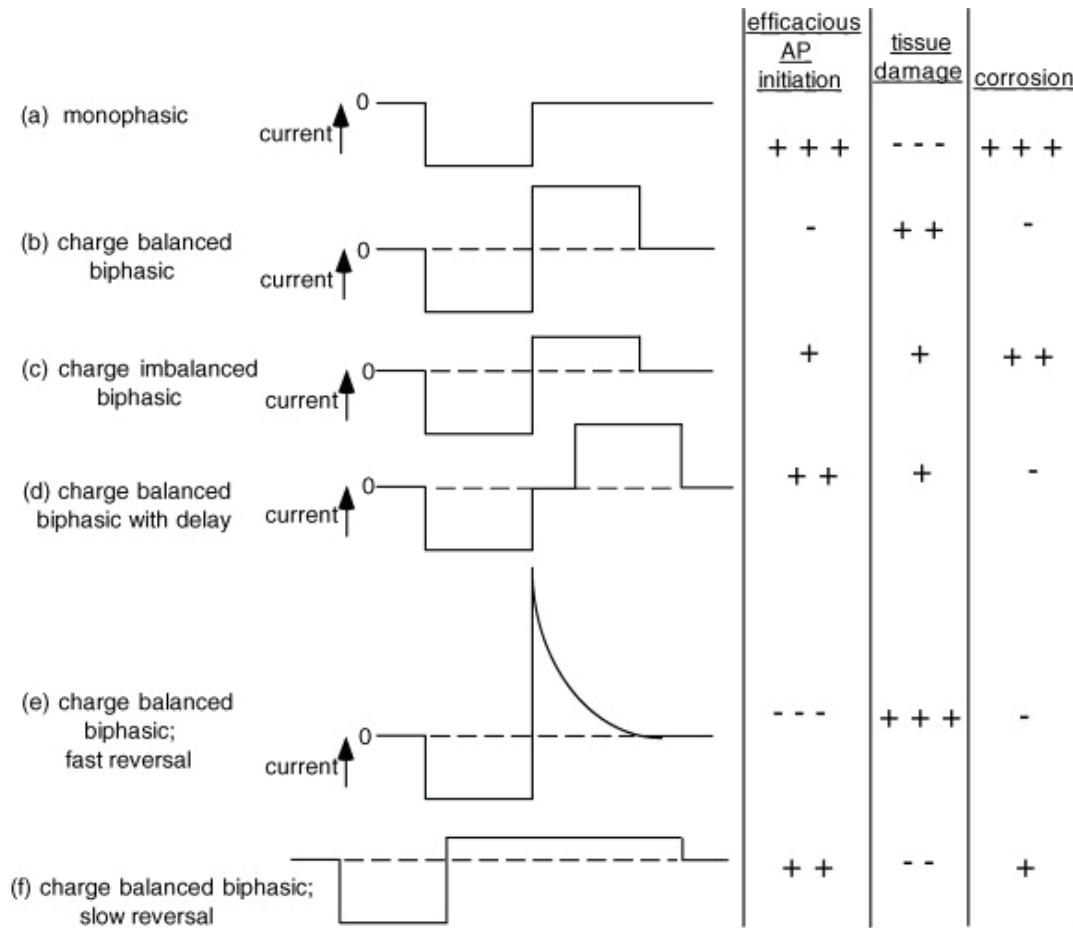


Figure 5.1: Comparison of stimulating waveforms. Six prototypical waveforms are rated for relative merit in efficacy and safety: ‘+++’ = best (most efficacious, least damaging to tissue or the electrode); ‘---’ = worst. Reproduced with permission from Elsevier [34].

5.1.1 Aims and Objectives

The overall aim of this chapter was to characterise the recording performance and stimulation efficacy of unmodified gold, conventional PEDOT/PSS and macroporous PEDOT/PSS microelectrodes. Based on electrochemical characterisation, we hypothesise that the macroporous coatings will perform similarly or better than conventional coatings. The specific objectives were to:

1. Characterise the noise floor of unmodified gold, conventional PEDOT/PSS and macroporous PEDOT/PSS coated electrodes pre- and post-culture.
2. Record spontaneous activity from primary hippocampal cells through unmodified gold, conventional PEDOT/PSS and macroporous PEDOT/PSS. Calculate Sig_{p-p} values and the respective SNR for each microelectrode material.
3. Record direct responses of neurons to biologically relevant voltage stimulation pulses through unmodified gold, conventional PEDOT/PSS and macroporous PEDOT/PSS.

5.2 Methods

5.2.1 Chemicals & Materials

Calcium chloride (CaCl_2), D-glucose, ethanol, HEPES buffer, magnesium chloride (MgCl_2), poly-D-lysine, potassium chloride (KCl) and sodium chloride (NaCl) were all purchased from Sigma Aldrich (Australia) and used as received. Hanks balanced salt solution (HBSS), minimum essential medium (MEM) and neural basal media (NBM) were all purchased from Gibco (USA). NBM was supplemented with B27 prior to use. Papain was purchased from Worthington (USA) and used as received. Fetal bovine serum was purchased from Moredgate Biotech (Australia) and used as received.

5.2.2 MEA Set-up

The components involved for this set-up included (i) a MEA device which contained the microelectrodes to be tested (described in *Chapter 3*), (ii) the bioamplifier which connected to the MEA device via neural interface board and (iii) the ADC which digitised data from the amplifier outputs (described in *Chapter 4*).

5.2.2.1 MEA Device

Gold coated glass slides (40 nm/100 nm, Ti/Au) were purchased from Deposition Research Laboratories Inc (DRLI, USA) and patterned using photolithographic techniques, as described in *Section 3.3.2*. The final MEA slides comprised a glass substrate, 14 individually addressable gold working electrodes and an SU-8 insulation layer which defined the diameter of the microelectrodes at 20 μm (*Figure 3.7*). A PDMS well was adhered onto the surface of the devices using medical grade silicone to allow for culture of neuronal cells on the MEA.

5.2.2.2 Microelectrode Materials

Each MEA device consisted of 4 bare gold microelectrodes, 5 conventional PEDOT/PSS and 5 macroporous PEDOT/PSS coated microelectrodes to enable comparison between different materials on the same substrate. Polymerisation conditions to fabricate different coatings on the same device were as follows;

Conventional PEDOT/PSS Conventional PEDOT/PSS coatings were deposited before coating 5 different electrodes with the macroporous template, this was because the PSS content in the monomer solution promoted carboxyl terminated polystyrene (PS-COOH) bead adhesion for the macroporous template. EDOT, 0.01 M, was added to an aqueous solution of 0.1 M PSS and stirred vigorously for one hour; the mixture was then purged with N₂ for 20 minutes. Conventional conducting polymers were deposited onto the 20 μm diameter gold working electrodes using potentiostatic polymerisation (Biologic VSP-300 electrochemical workstation) in a three electrode cell (as described in *Chapter 3.3.3*). An applied potential of 0.95 V to the working electrode was used until the total charge passed (calculated through integration of the resulting time vs current plot) reached 1000 nC — equating to 318 mC cm^{-2} .

Macroporous PEDOT/PSS PS-COOH beads were deposited as a sacrificial template on the MEAs using flow controlled vertical deposition (FCVD), as described in *Section 3.3.3.2*. CPs were polymerised around the PS-COOH template using potentiostatic methods described above for conventional conducting polymer films. Macroporous films were also polymerised at a charge density of 318 mC cm^{-2} followed by selective PS-COOH etching with dimethylformamide (DMF).

5.2.2.3 Data Acquisition

All microelectrode recordings from the MEA devices were amplified and digitised using the modified amplifier and acquisition set-up described in *Chapter 4*. The amplifier operated between 0 and 5 V with a 2.5 V reference offset. Total gain was set at 2000 within the bandwidth of 0.7 Hz to 10 kHz. Samples were acquired at a rate of 20,000 S s⁻¹ and all data was logged in National Instruments .TDMS binary format.

5.2.2.4 Primary Hippocampal Neuron Cultures

PDMS wells on the MEAs were filled with 6 mL milliQ water which was replaced every 6 hours, 24 hours prior to cell culture. This was done to remove aqueous contaminants on the surface of the MEA devices from polymerisation and microfabrication processes. MilliQ water was replaced with ethanol and slides were washed 3 times with 100% ethanol followed by 45 minutes of UV exposure to sterilise the MEA devices. Primary hippocampal neurons from Wistar rats, at postnatal day zero, were then cultured onto the MEA devices at a density of 50,000 cells cm⁻² using the methods outlined in *Section 3.3.7.1*. The MEA devices were then placed in a 5% CO₂ incubator (ThermoFisher Scientific, USA) at 37 °C for 28 days. Half the NBM was replaced at *days in vitro* 1 (DIV 1) and a quarter replaced at DIV 7 and DIV 14. Electrophysiological recording of neurons through the MEA were carried out at DIV 16 in Tyrode's solution. Neuronal stimulation was carried out at DIV 14 both DIV 7 and DIV 14 in cell culture media.

5.2.2.5 Noise Floor Characterisation

Noise Amplitude The noise floor of each microelectrode material was quantified pre- and post- culture in Tyrode’s solution. Pre-culture noise was defined as data acquired from the MEA devices through the bioamplifier and data acquisition system when no neurons were present on the slide. Post-culture noise was defined as acquired data regions containing no neuronal activity at DIV28. An RMS value was calculated for each data stream using the Python script detailed in *Section 4.2.5.1* and peak-to-peak values were estimated within a 99.99% confidence interval. The data was obtained from 3 different samples for each microelectrode material and represented as the mean \pm standard deviation.

Electrochemical Impedance Spectroscopy Pre- and post-culture impedance spectra were obtained to gain an understanding on how neuronal culture impacted microelectrode impedance properties. Rather than re-using impedance spectra from *Chapter 3* for pre-culture data, samples were re-analysed in Tyrode’s solution to allow for a direct comparison with post-culture samples. Measurement parameters were identical to those described in *Section 3.3.4*.

5.2.2.6 Confirmation of Neuronal Activity

Tetrodotoxin (TTX) (Alomone Labs) is an established potent and selective antagonist of TTX-sensitive sodium channels [143,144] and was used to confirm neuronal origin of the recorded signals. A 15.7 μ M stock solution was made by dissolving 50 μ g of powder in 10 mL milliQ water. TTX, 255 μ L, was then added to the Tyrode’s solution bathing the neurons achieving a final concentration of 1 μ M.

5.2.2.7 Neuronal Activity Recording

Spontaneous Neuronal Activity Cell culture media was replaced with 4 mL Tyrode's solution and spontaneous neuronal activity was recorded through the microelectrodes using the bioamplifier and data acquisition system detailed in *Chapter 4*. Following acquisition the time traces from each microelectrode were processed offline using a Matlab based program, `Wave_clus` [145]. The program first detects spikes from the data based on user input parameters, followed by feature extraction and super-paramagnetic clustering. For spike detection the input data is first filtered between 300 Hz and 3000 Hz using a 4th order IIR Butterworth filter to isolate for extracellular action potential data. A threshold for spike detection is then applied to the filtered data ($|x|$) at 4 times the estimated standard deviation of the noise floor (σ_n).

$$Threshold = 4\sigma_n \quad \sigma_n = median \left\{ \frac{|x|}{0.6745} \right\} \quad (5.5)$$

The standard deviation of the noise floor is calculated automatically through *Equation 5.5* which estimates noise based on the median rather than the mean to reduce interference from spike associated with neuronal activity [146]. `Wave_clus` then extracts spikes from the continuous data stream via automatic selection of wavelet coefficients chosen with a Kolmogorov Smirnov test of Normality [147], followed by a super-paramagnetic automatic clustering algorithm which groups together extracted spikes of similar shapes and associates them with a unit (one neuron) [148].

Results from spike sorting carried out by `Wave_clus` were then used to inform signal amplitudes for SNR measurements. The number of units for each microelectrode were determined and the average peak to peak amplitude of all spikes associated with that unit were used to calculate Sig_{p-p} . $Noise_{p-p}$ for the

same microelectrode was then calculated through $6.6 \times \text{RMS}$ of an area with no neuronal activity and SNR was calculated via *Equation 5.2*.

5.2.2.8 Stimulation Efficacy

Cell culture media was replaced with Tyrode's solution and neuronal activity was measured in response to stimulation pulses at different amplitudes. Neurons were tested at both DIV 7 & DIV 14. Younger cells were used in this experiment, compared to the recording experiment, to minimise spontaneous activity so that stimulation parameters could be tested. A voltage stimulator (Grass Medical Instruments, USA) was utilised as the voltage source and was controlled by digital triggers from the National Instruments ADC (*Section 4.2.4.2*). Unmodified gold, conventional PEDOT/PSS and macroporous PEDOT/PSS coatings were subject to either monophasic (cathodic) or biphasic (cathodic first) pulses of $100 \mu\text{s phase}^{-1}$ duration and amplitudes of 100 mV, 200 mV, 400 mV, 800 mV and 1000 mV. Each pulse amplitude was tested 3 times with an interpulse duration of 5 seconds.

The electrode used for stimulation was also used for recording direct responses. Stimulation efficacy was defined as the number of direct responses recorded after a stimulation pulse. Direct responses to the stimuli were taken as spikes that occurred within 20 ms post-stimulus, as defined by Wagenaar et al. [149]. The data was post-processed (4^{th} order, Butterworth) and thresholding at $4\sigma_n$ was again used for spike detection (*Equation 5.5*).

5.3 Results & Discussion

5.3.1 *In-vitro* Microelectrode Noise Characterisation

5.3.1.1 Pre-Culture

The absence of biological species predominantly eliminates sources of noise external to the recording instrumentation and microelectrode/electrolyte interface (assuming negligible power line interference due to shielding) [11, 36, 150, 151]. The total expected noise was calculated through quadratic addition of thermal RMS noise, estimated from the impedance spectra of each microelectrode, and amplifier RMS noise values obtained from *Chapter 4*. These values predicted that gold microelectrodes would possess the highest noise amplitude at $36 \pm 3 \mu\text{V}_{p-p}$, followed by conventional and macroporous PEDOT/PSS coatings at $15 \pm 1 \mu\text{V}_{p-p}$ and $11 \pm 3 \mu\text{V}_{p-p}$ (*Table 5.1*).

Table 5.1: Expected and recorded peak-to-peak noise (μV_{p-p}) values of gold, conventional PEDOT/PSS and macroporous PEDOT/PSS pre- and post-culture. CP coatings were polymerised at a charge density of 318 mC cm^{-2} . Measurements were taken in Tyrode’s solution, data represented as mean \pm standard deviation ($n = 3$)

Microelectrode	Expected Noise (μV_{p-p})	Pre-culture Noise (μV_{p-p})	Post-culture Noise (μV_{p-p})	% Change in Noise
Gold	36 ± 3	38 ± 4	45 ± 3	110 ± 9
Conventional PEDOT/PSS	15 ± 1	18 ± 1	32 ± 6	175 ± 37
Macroporous PEDOT/PSS	11 ± 3	19 ± 2	38 ± 2	198 ± 16

The recorded peak to peak values agreed with the predicted values where CP coatings displayed a significant improvement in noise amplitude from $38 \pm 4 \mu\text{V}_{p-p}$, for gold, to $18 \pm 1 \mu\text{V}_{p-p}$ and $19 \pm 2 \mu\text{V}_{p-p}$ for conventional and macroporous PEDOT/PSS, respectively (*Table 5.1*). The marked difference

in CP coated noise amplitudes as compared to bare gold microelectrodes are likely a result of more favourable impedance properties, as theorised in *Chapter 3*. Note the absence of a 50 Hz peak in the frequency domain, illustrating the success of the amplifier interface board and shielding design.

Figure 5.2 displays representative recorded noise spectra in the time and frequency domain prior to culture. Analysis of *Figure 5.2B* shows a noise spectrum similar to that of white noise between 100 and 2000 Hz, where the noise amplitude is consistent within the bandwidth analysed. At frequencies below 100 Hz noise amplitude rises and can be explained by a significantly higher resistive component at low frequencies — resulting in higher levels of thermal noise.

5.3.1.2 Post-Culture

Table 5.1 also lists peak to peak noise values 28 days after culture from the same group of microelectrodes analysed pre-culture. All microelectrodes showed increases in the recorded noise amplitudes, with gold microelectrodes still higher at $45 \pm 3 \mu\text{V}_{p-p}$ as compared to $32 \pm 6 \mu\text{V}_{p-p}$ and $39 \pm 2 \mu\text{V}_{p-p}$ for conventional and macroporous PEDOT/PSS, respectively.

When analysing the % change in noise it was apparent that the CP modified microelectrodes suffered higher increases in noise peak to peak values at $175 \pm 37\%$ and $198 \pm 16\%$ for conventional and macroporous PEDOT/PSS as compared to $110 \pm 9\%$ for gold. *Figure 5.3* displays representative recorded noise spectra in the time and frequency domain 28 days after culture. A similar spectral pattern was evident with the only difference being higher noise amplitudes across all frequencies.

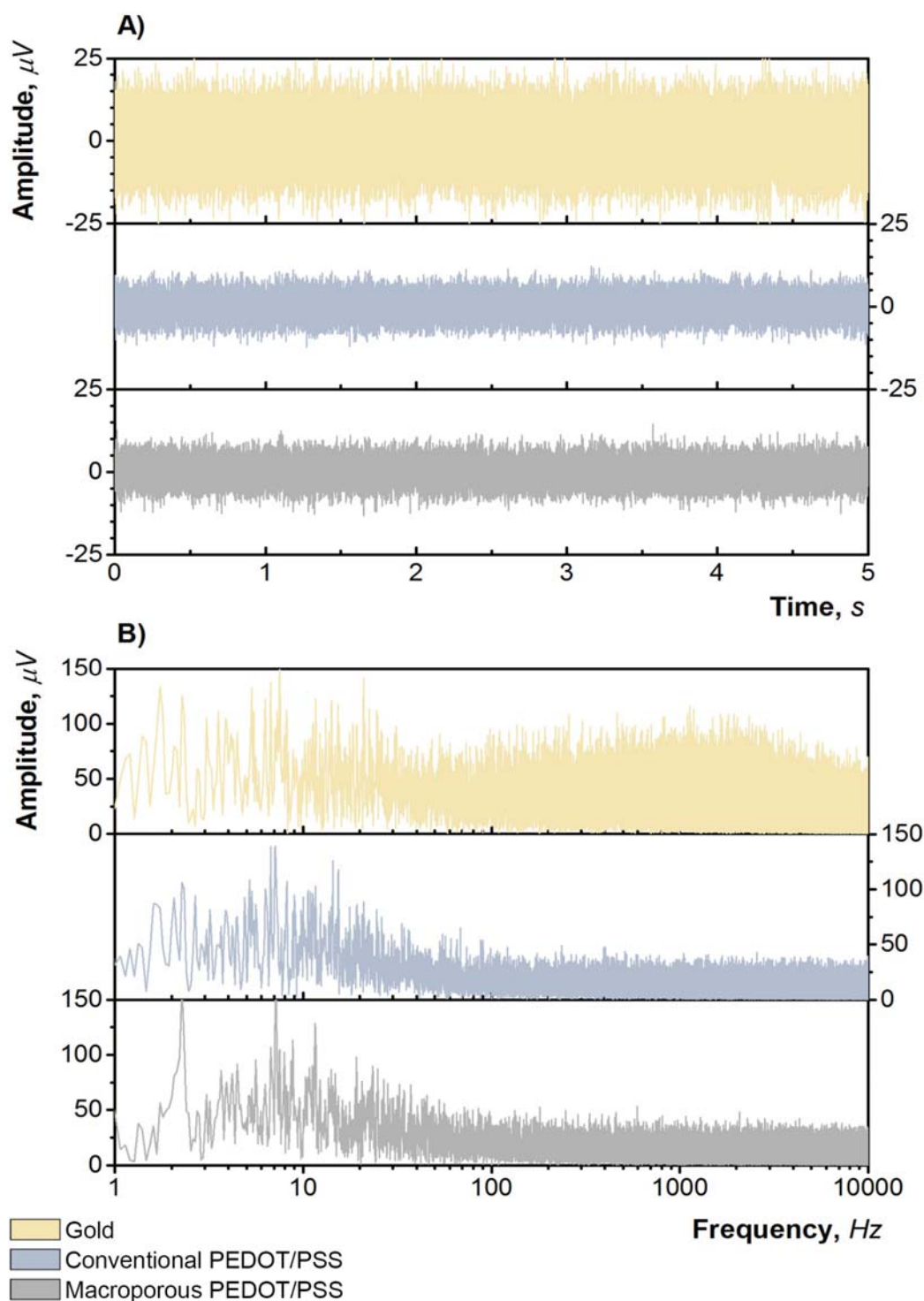


Figure 5.2: Representative noise spectra for gold, conventional PEDOT/PSS and macroporous PEDOT/PSS in the A) time and B) frequency domain pre-culture. A clear reduction in noise amplitude can be seen after modification of the gold micro-electrodes with either conventional or macroporous PEDOT/PSS.

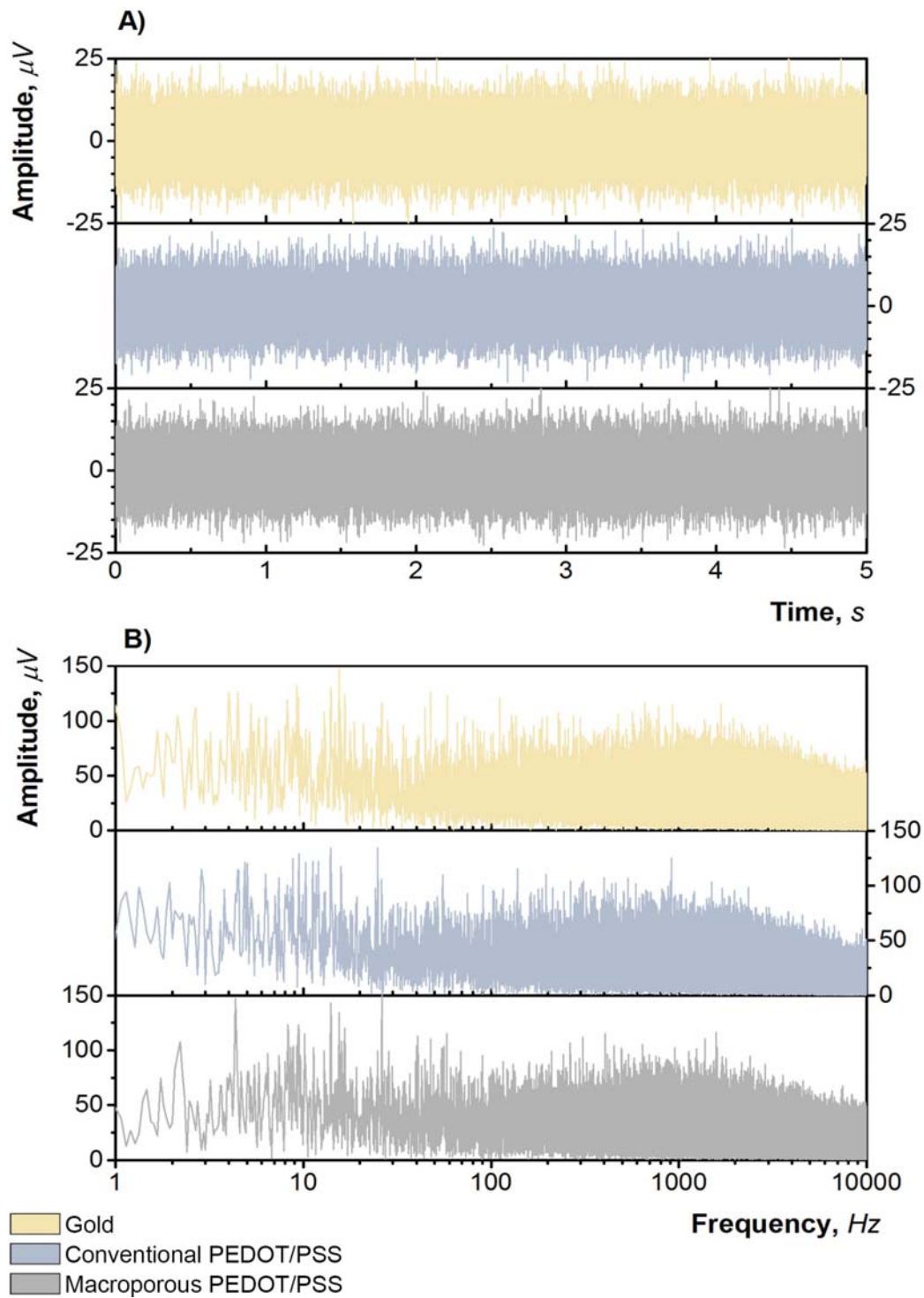


Figure 5.3: Representative noise spectra for gold, conventional PEDOT/PSS and macroporous PEDOT/PSS in the A) time and B) frequency domain post-culture. The noise amplitude increased for CP coated microelectrodes, indicating electrode biofouling.

To investigate the increase in noise, impedance spectra of CP coated microelectrodes were taken pre- and post-culture with results plotted as Nyquist diagrams (*Figure 5.4*). A larger mean resistive component and standard deviation post-culture, as compared to pre-culture, was noticed across all frequencies (observed as a rightward shift) for both conventional (*Figure 5.4A*) and macroporous PEDOT/PSS (*Figure 5.4B*). This would therefore introduce higher levels of thermal noise into the system and explains the increase in noise observed. An increase in resistance is likely a result of electrode biofouling, where biomolecules and cells present in the culture media adsorb to the electrode surface [152–154]. The higher change in peak to peak values for CP coated microelectrodes may be due to an increase in adsorption of biomolecules within the nodules and/or pores present within the CP structure. Nonetheless, CP coated microelectrodes still exhibited significantly lower noise amplitudes ($p < 0.05$) when compared to unmodified gold. No significant difference between conventional and macroporous PEDOT/PSS post-culture noise amplitudes were apparent ($p > 0.05$).

5.3.2 Spontaneous Neuronal Recording

5.3.2.1 Confirmation of Neuronal Activity

To confirm neuronal origin of the recorded spikes TTX was added to the recording media bathing the neurons. *Figure 5.5* displays a time trace of the recorded data before and after TTX addition. Large spikes can be seen prior to treatment with TTX, followed by clear signs of diminishing activity out to approximately 200 seconds post-TTX. TTX addition is a common test carried out in electrophysiology experiments to selectively block sodium channels on the neuronal membrane, its time course of action is usually around 5 minutes, correlating with the data seen in *Figure 5.5* [155].

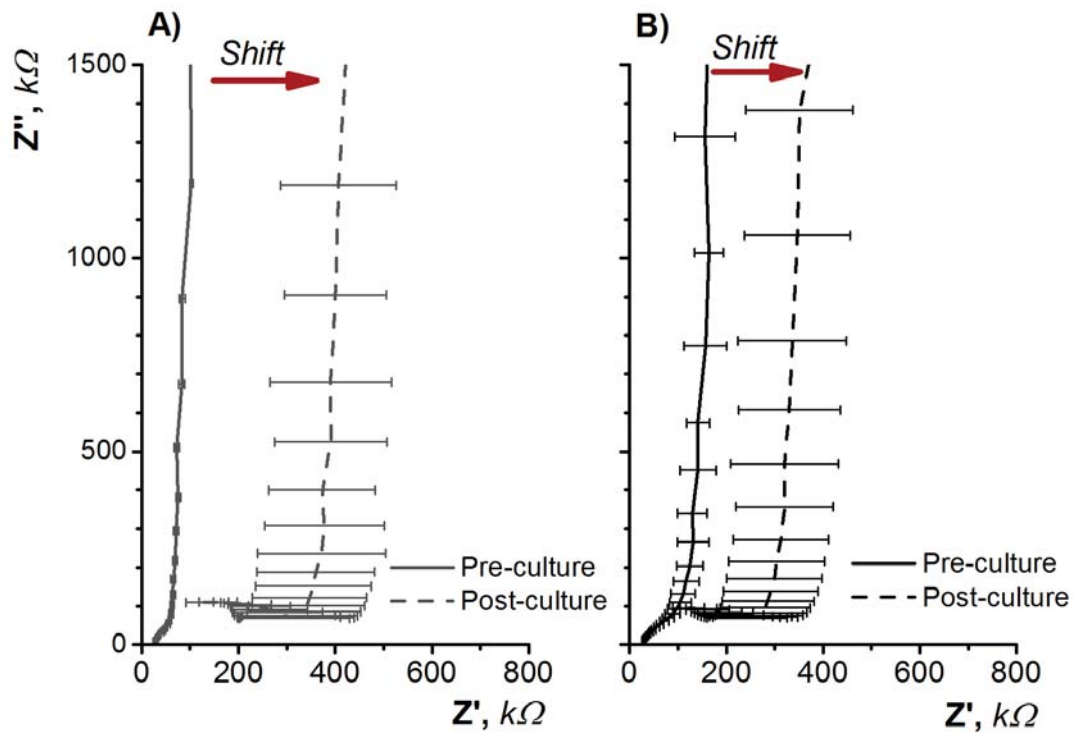


Figure 5.4: Nyquist plots of A) conventional and B) macroporous PEDOT/PSS before (—) and 28 days after (---) culture. A shift towards the right for post-culture samples indicates a larger resistive component (Z') which leads to higher levels of thermal noise. All measurements were carried out in Tyrode's solution and data was plotted as the mean with error bars representing the standard deviation ($n = 3$).

5.3.2.2 Signal to Noise Ratio

Spontaneous neuronal activity was recorded through the microelectrodes embedded on the microelectrode arrays. A total of three MEA devices were used in this experiment resulting in recordings from 12 gold, 15 conventional PEDOT/PSS and 15 macroporous PEDOT/PSS microelectrodes. Representative time traces of the acquired data (*Figure 5.6*) show recordings from the different microelectrode materials. Bursts of activity were observed followed by short pauses correlating with previously reported extracellular activity patterns [156]. Out of the microelectrodes tested 1/12 gold, 4/15 conventional PEDOT/PSS and 3/15 macroporous PEDOT/PSS displayed active recordings. Whilst the presence of recordings is heavily dependent on the distance of neurons from the

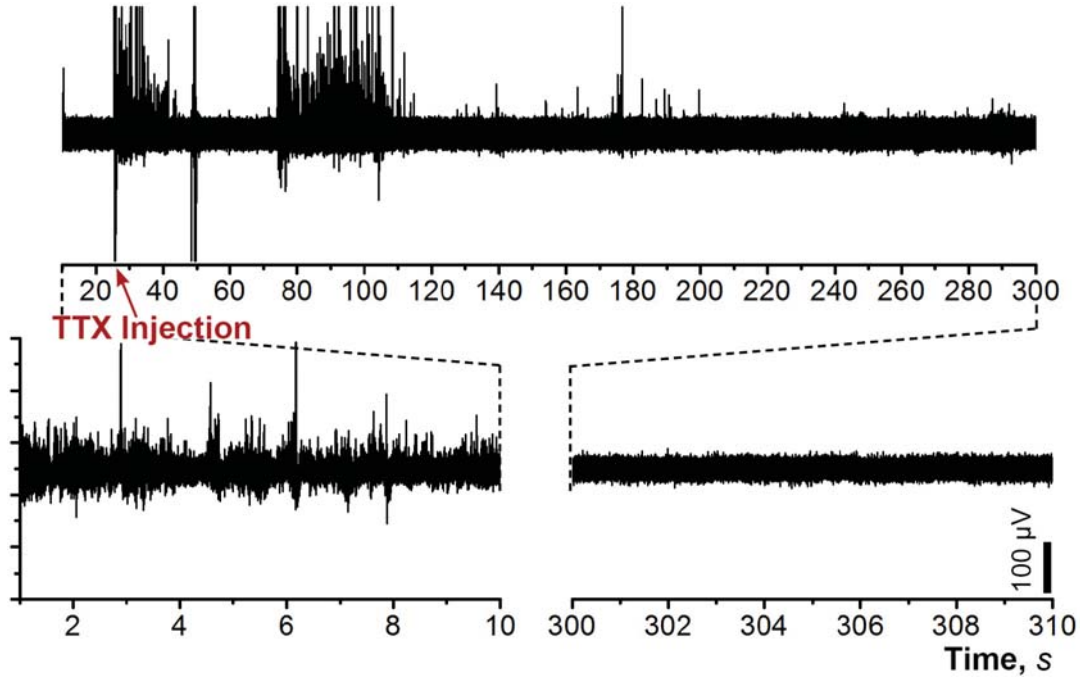


Figure 5.5: Time trace acquired from a conventional PEDOT/PSS modified microelectrode before and after addition of TTX. TTX was added 25 seconds into the recording and indicated by an arrow in the figure. Diminished activity is clear approximately 200 seconds after the addition of TTX confirming neuronal origin of the recorded spikes.

microelectrode, the larger noise floor of gold may make distinguishing this activity more difficult. Furthermore, higher impedance magnitudes of gold microelectrodes increases the amount of signal lost through shunt pathways, resulting in reduced signal amplitudes [46].

The recorded data traces were bandpass filtered (butterworth, 4th order) between 300 and 3000 Hz to discard local field potentials present within the low frequency band (1-200 Hz) and isolate for spikes associated with neuronal action potentials. Spikes were then extracted and clustered using `Wave_clus`, as described in *Section 5.2.2.7*. *Figure 5.7* shows the result of this process on the representative time traces in *Figure 5.6*. This process was carried out to attribute an average spike amplitude, Sig_{p-p} , to each unit and enable calculation of a SNR.

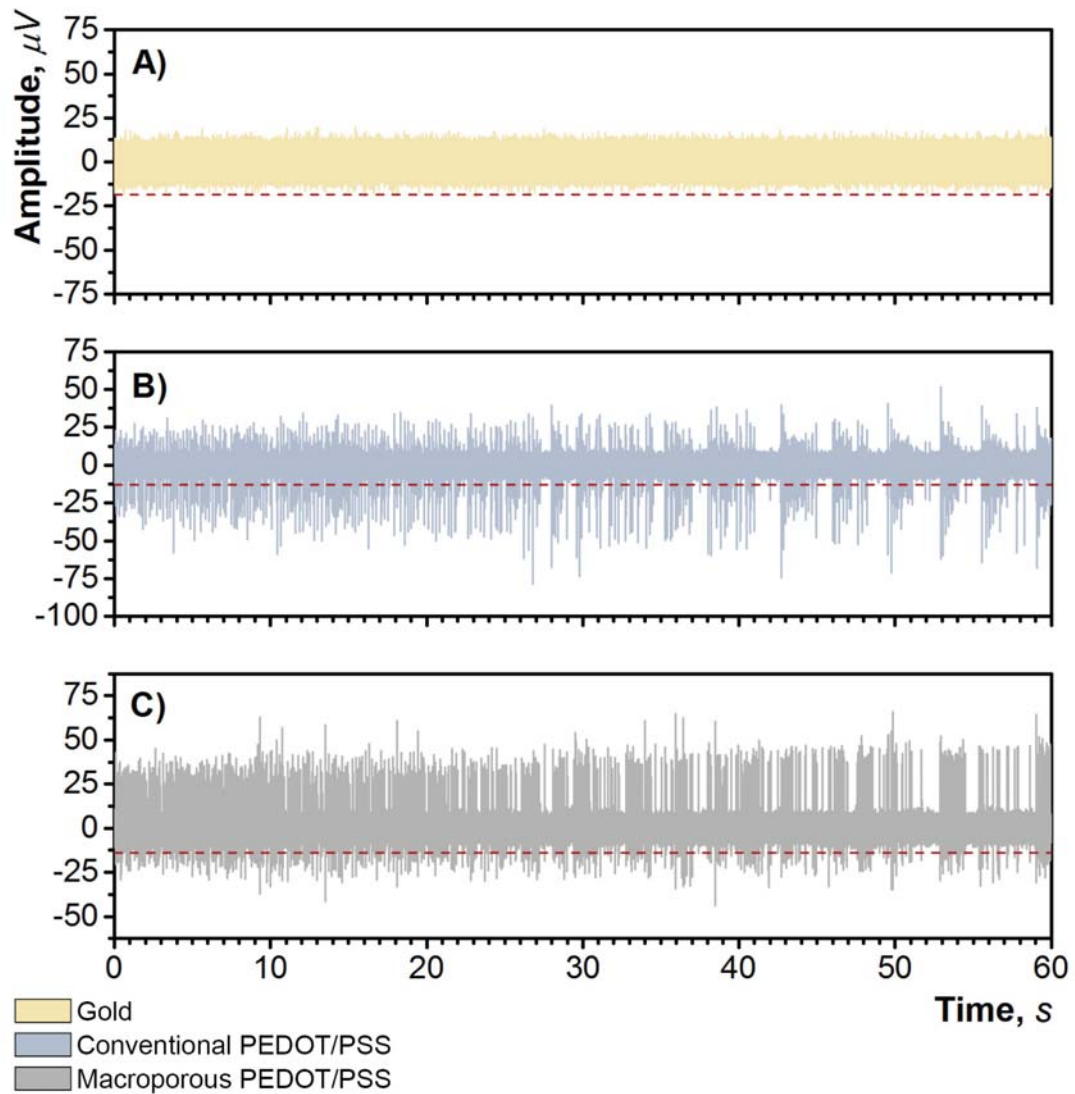


Figure 5.6: Representative time traces of recorded spontaneous activity from A) gold, B) conventional PEDOT/PSS and C) macroporous PEDOT/PSS microelectrodes, 16 days post-culture. Clear activity can be seen in both the CP coatings used whereas gold displayed activity at a much lower amplitude. The red dashed line indicates the threshold used to detect spikes and was set at 4σ (Equation 5.5).

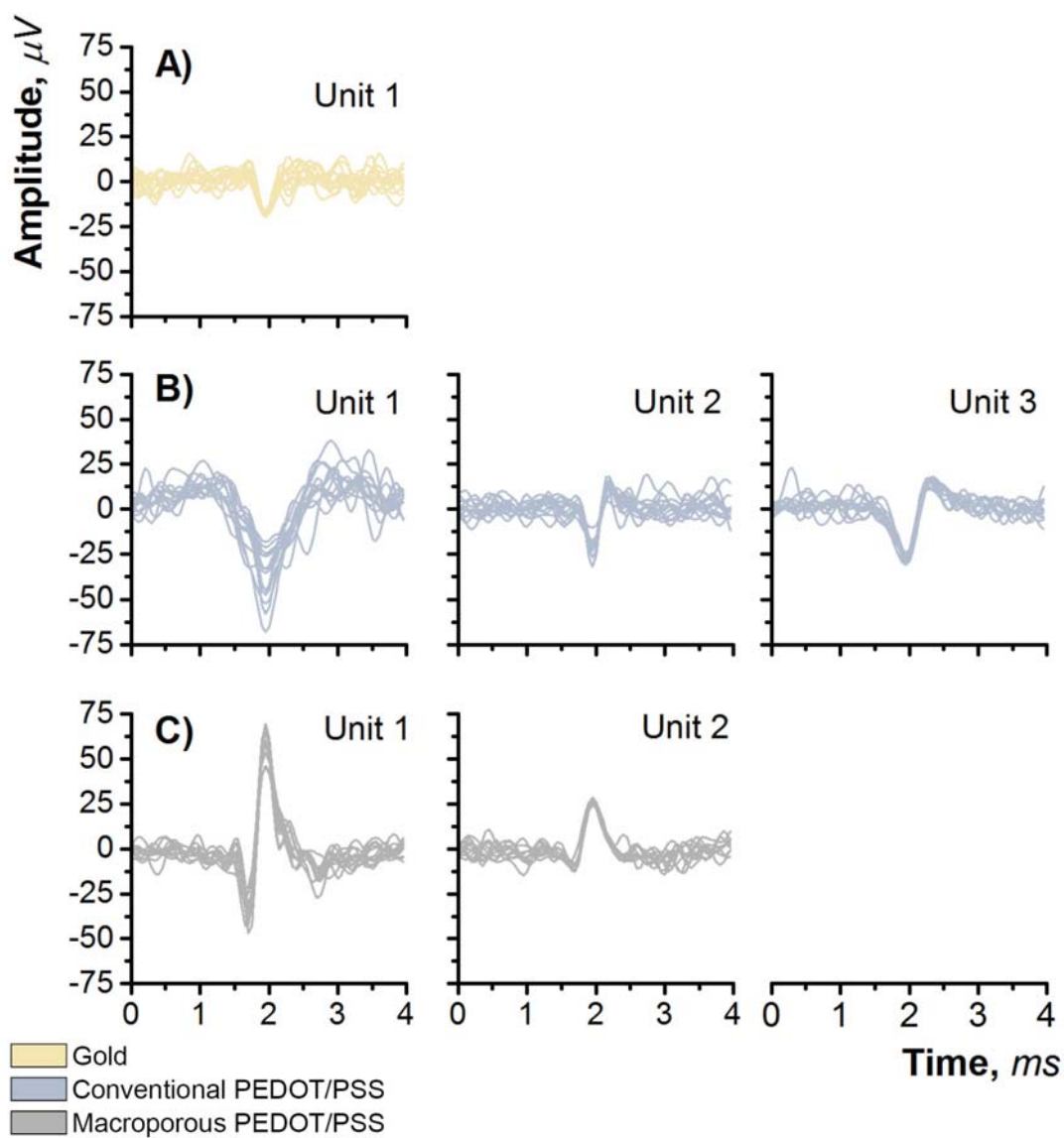


Figure 5.7: Extracted and clustered spikes from data presented in *Figure 5.6* for A) gold, B) conventional PEDOT/PSS and C) macroporous PEDOT/PSS.

Clustering results displayed one detected unit for gold with an average amplitude of $31.4 \mu\text{V}_{p-p}$. Three units were detected for recordings carried out through conventional PEDOT/PSS with average amplitudes of $54.0 \mu\text{V}_{p-p}$, $33.3 \mu\text{V}_{p-p}$ and $38.7 \mu\text{V}_{p-p}$. Two units were detected through macroporous PEDOT/PSS at amplitudes of $101.0 \mu\text{V}_{p-p}$ and $38.0 \mu\text{V}_{p-p}$. *Table 5.2* lists SNR values for each microelectrode with detectable neuronal activity and its associated units. The gold microelectrode detected unit activity with an SNR of 0.6, CP coated microelectrodes had SNR values from 1.4 to 16.6 for conventional PEDOT/PSS and 2.6 to 11.1 for macroporous PEDOT/PSS.

Table 5.2: SNR values of unmodified gold, conventional PEDOT/PSS and macroporous PEDOT/PSS with detectable neuronal recordings. Sig_{p-p} values were taken as the average peak to peak signal amplitude of the filtered waveform. Noise_{p-p} values were taken as the peak to peak noise amplitude of the filtered waveform.

Sample	Sample Number	Units Detected	Unit Number	Noise _{p-p} (μV)	Sig _{p-p} (μV)	SNR (dB)
Gold	1	1	1	29.4	31.4	0.6
	1	3	1	28.4	33.3	1.4
Conventional PEDOT/PSS	1	3	2	28.4	38.7	2.7
			3	28.4	54.0	5.6
			1	28.7	56.4	5.7
	2	2	2	28.7	76.4	8.5
			1	28.4	133.0	13.4
	3	3	2	28.4	74.6	8.4
			3	28.4	191.8	16.6
			1	26.7	46.6	4.8
	4	3	2	26.7	53.6	6.1
			3	26.7	51.7	5.7
			1	28.4	46.6	4.3
	Macroporous PEDOT/PSS	1	3	2	28.4	53.6
3				28.4	51.7	5.2
1				28.1	44.8	4.1
2		2	2	28.1	39.5	3.1
			1	28.1	101	11.1
3		2	2	28.1	38	2.6

Figure 5.8 represents a cumulative frequency plot of the SNR for each detected spike through uncoated gold, conventional PEDOT/PSS and macroporous PEDOT/PSS. The plot enables a visual representation of the distribution of SNR values for the respective microelectrodes.

Gold microelectrodes, conventional PEDOT/PSS and macroporous PEDOT/PSS coatings displayed maximum SNR values of 2.72, 17.57 and 12.65, respectively (*Table 5.3*). As expected both CP coatings improved mean and median SNR values of uncoated gold microelectrodes. The macroporous PEDOT/PSS coatings did not further improve recording performance of conventional PEDOT/PSS coatings with lower mean, 4.14 vs 5.43, and median, 4.05 vs 4.24, values respectively.

Table 5.3: Statistical parameters of SNR values for unmodified gold, conventional PEDOT/PSS and macroporous PEDOT/PSS, as calculated from the cumulative frequency plot represented in *Figure 5.8*

Sample	Minimum (dB)	Maximum (dB)	Mean (dB)	Median (dB)	Standard Deviation (dB)
Gold	0.02	2.72	0.86	0.64	0.64
Conventional PEDOT/PSS	0.01	17.57	5.43	4.24	4.11
Macroporous PEDOT/PSS	0.01	12.65	4.14	4.05	2.25

A limitation of the SNR metric to quantify microelectrode recording performance resides in its exclusion of a neuronal distance parameter. Neuronal distance is a large determinant in the amplitude of the recorded spike potential at the electrode site and can be modelled through *Equation 5.1*. It is possible that neurons surrounding conventional PEDOT/PSS microelectrodes were substantially closer than those surrounding unmodified gold and macroporous PEDOT/PSS coatings - resulting in higher SNR values. The effect of neuronal distance could be ‘averaged out’ with a much large sample number, however, a

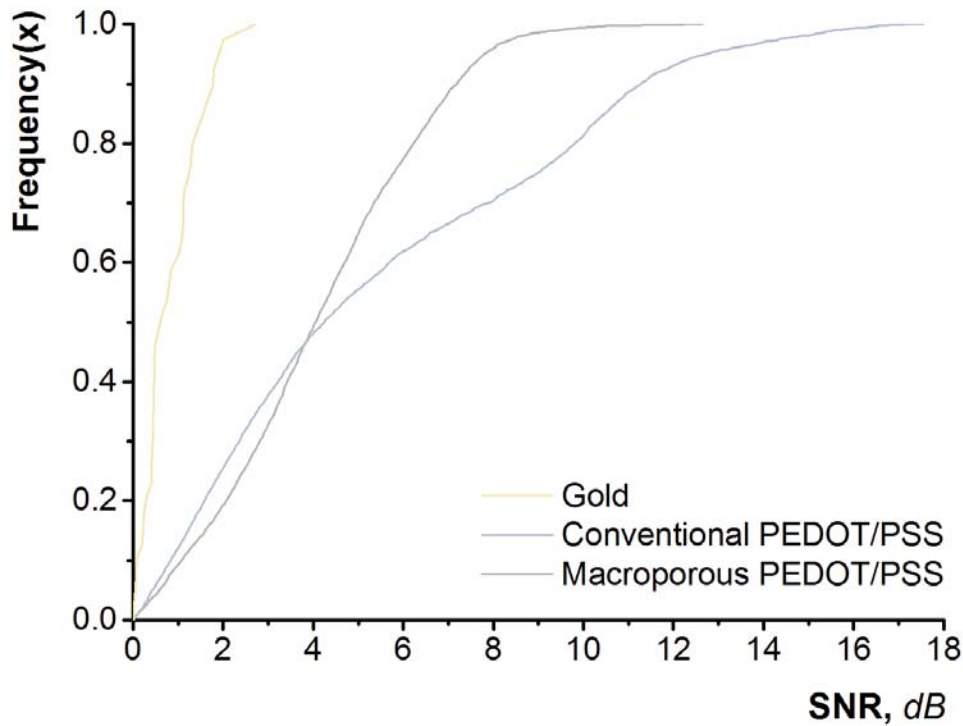


Figure 5.8: Cumulative frequency plot of SNR values for unmodified gold, conventional PEDOT/PSS and macroporous PEDOT/PSS coatings. The plot indicates both CP coatings out-perform gold microelectrodes and conventional PEDOT/PSS coatings achieving slightly higher values than macroporous PEDOT/PSS coatings.

more accurate determination of recording performance would link the expected potential at the microelectrode and the recorded spike amplitude. To achieve this, a system capable of optically visualising neuronal activity in real-time would be required and is described in the Future Directions section in *Chapter 6*.

5.3.3 *In-vitro* Stimulation Efficacy

Stimulation efficacy of unmodified gold, conventional PEDOT/PSS and macroporous PEDOT/PSS coatings was characterised through assessment of direct neuronal activity in response to injected voltage stimuli of increasing amplitudes. Unfortunately, no direct responses post-stimulus were recorded from any microelectrodes on MEA devices containing primary hippocampal cells at

either DIV7 or DIV14. This was a result of several limitations and mostly revolved around MEA device architecture. The architecture of the MEA devices used did not allow for the use of electrode pairs where one electrode would be used to stimulate, and the surrounding electrodes would record invoked neuronal responses. This was due to a large inter-electrode distance of approximately 2 mm. Therefore, our experiment used the same electrode for both stimulation and recording. In order to achieve this, the voltage source would be coupled to the electrode in parallel to the recording output. This method of connection presented two problems; (i) the introduction of noise from the voltage source in the recorded signal and (ii) an apparent stimulus artifact on the recording electrode as a result of an injected voltage pulse.

The level of noise observed through the microelectrodes after connection of the voltage source increased for all electrodes to a value of approximately $254 \mu V_{p-p}$. FFT analysis of the noise spectra revealed a large 50 Hz component with prominent 50 Hz harmonics throughout the entire bandwidth (*Figure 5.9*). This noise was likely due to interference from the mains power-line used to power the voltage stimulator. In order to remove noise contamination a comb filter was constructed in Matlab (*Figure 5.10*) which selectively removed the 50 Hz frequency and its accompanying harmonics. Although noise was successfully removed, the filter also attenuated signals in the frequency region where neuronal activity resides (300 - 3000 Hz).

To enable recording of direct invoked responses which occurred 20 ms post stimulus, the stimulation pulse had to be short in duration to reduce the recorded stimulation artifact. Both monophasic and biphasic stimuli, 100 μs duration, were trialled on an MEA device containing Tyrode's solution. Their respective post stimulus artifact times can be seen in *Figure 5.11*. Monophasic pulses were selected due to a shorter post-stimulus artifact (2 ms) when compared to the artifact resulting from biphasic pulses (6 ms). Pulses of greater phase duration

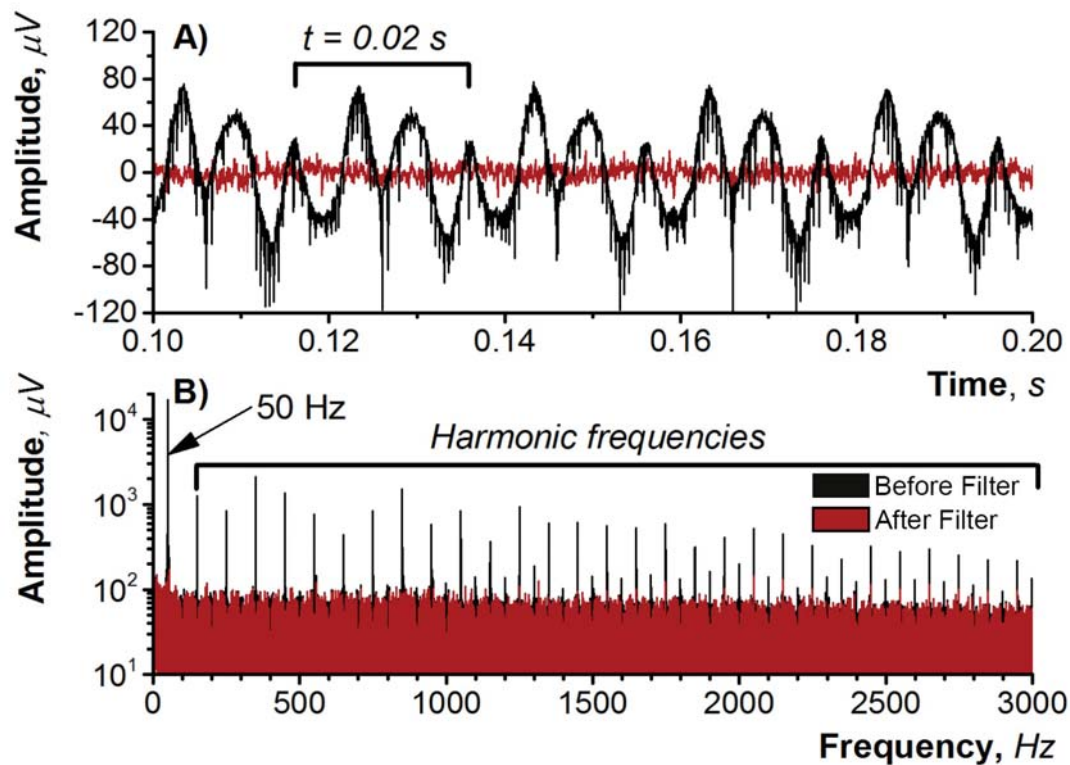


Figure 5.9: Noise recorded from a conventional PEDOT/PSS microelectrode with a voltage stimulator connected in parallel in the A) time and B) frequency domains. The graph shows noise spectra before and after application of a comb filter. A prominent 50 Hz signal can be seen in both the time and frequency domains (note the logarithmic scale for frequency domain) prior to filtering.

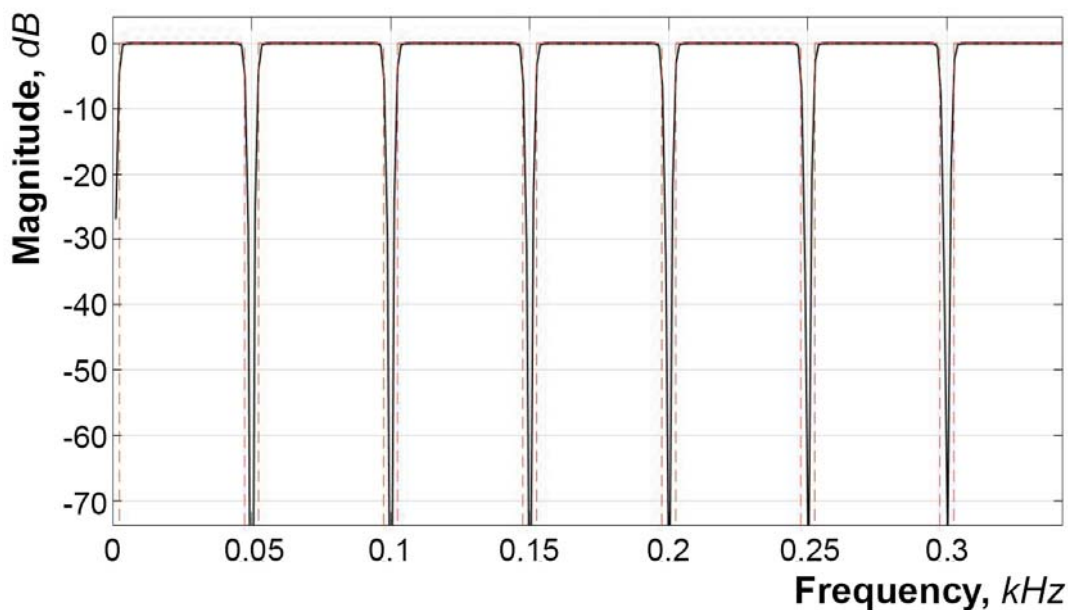


Figure 5.10: Magnitude response of the constructed IIR comb filter. The filter was designed to selectively remove 50 Hz and its harmonic components. A bandwidth of 300 Hz is shown in this graph for clarity, however, the filter removes all harmonics up to 10 kHz.

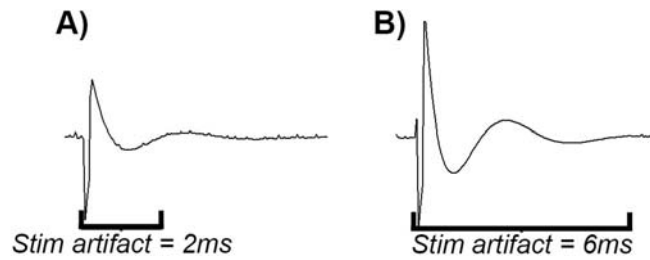


Figure 5.11: Stimulus artifact times in response to A) monophasic and B) biphasic voltage pulses of $100 \mu\text{s}$ duration and 1 V amplitude.

(> $100 \mu\text{s}$) introduced post-stimulus artifacts greater than 10 ms which made recording of direct responses difficult. It is possible that the short, monophasic, waveform was insufficient in stimulating direct neuronal responses from primary hippocampal neurons [149].

Limitations external to MEA device architecture revolved around the age of primary hippocampal neurons. Younger neurons were hypothesised to minimise interference from spontaneous neuronal activity, limiting the recorded spikes to direct responses post stimulus. In the future, a culture period of longer than DIV 14 may be required to ensure neuronal processes are sufficiently surrounding the microelectrode stimulation sites to achieve successful stimulation.

5.4 Conclusions

Unmodified gold, conventional PEDOT/PSS and macroporous PEDOT/PSS were investigated for recording performance and stimulation efficacy. Noise floor characterisation displayed the benefits of CP coatings in reducing recorded noise, with a significant decrease from $38 \pm 4 \mu\text{V}_{p-p}$ for gold, to $18 \pm 1 \mu\text{V}_{p-p}$ and $19 \pm 1 \mu\text{V}_{p-p}$ for conventional and macroporous PEDOT/PSS, respectively ($p < 0.05$). No significant improvements in recorded noise pre-culture were noticed from the macroporous PEDOT/PSS coating when compared to conventional PEDOT/PSS coatings ($p > 0.05$). All electrode materials exhibited an increase in noise post-culture, which was a result of electrode biofouling processes. However, CP coated microelectrodes still exhibited a lower noise floor when compared to unmodified gold. Recording performance, as measured through SNR, showed CP coatings increased mean SNR values of gold from 0.86 to 5.43 and 4.14 for conventional and macroporous PEDOT/PSS coatings. Macroporous PEDOT/PSS coatings yielded lower values over all the statistical metrics tested (max, mean and median SNR) and provided no additional improvements in SNR over conventional PEDOT/PSS coatings.

Results for stimulation efficacy were not obtained, which was attributed to the limitations of the MEA devices used. The large inter-electrode distance on the MEA devices resulted in the use of the same microelectrode for both stimulation and recording. Noise introduced from the voltage source and post-stimulus artifacts made recording direct neuronal responses difficult. The stimulation pulse could be refined to decrease noise and post-stimulus artifact length. In the future, an altered MEA architecture could be used with paired stimulation and recording electrodes as well as investigating the use of older cultures (DIV 21) which are likely to be more active.

Chapter 6

Conclusions & Future Outlook

6.1 Conclusions

To test the hypothesis that macroporous conducting polymer (CP) coatings would result in a microelectrode material with superior recording performance and stimulation efficacy, a microelectrode array (MEA) was constructed and comprised a glass substrate, gold electrode material and an SU-8 insulation layer which defined the size of the microelectrodes at 20 μm . Reproducible methods for conventional poly(3,4-ethylenedioxythiophene)/polystyrene sulphonate (PEDOT/PSS) and macroporous PEDOT/PSS electrodeposition (both potentiostatic and galvanostatic) on the gold microelectrodes were achieved. Flow controlled vertical deposition (FCVD) of the carboxyl-terminated polystyrene bead template was optimised to yield highly ordered macroporous CP coatings. The presence of macropores was confirmed via scanning electron microscopy (SEM). Both conventional and macroporous CP coatings drastically improved CSC_c , CIL, impedance properties and thermal noise of gold microelectrodes. No significant differences between conventional and macroporous PEDOT/PSS coatings were observed in CSC_c for all deposition charge densities. However, the macroporous coatings yielded significant improvements in CIL, impedance and thermal noise at the highest deposition charge density of 637 mC cm^{-2} ($p < 0.05$). There were no significant differences in the electrochemical parameters investigated between potentiostatic and galvanostatic polymerisation groups. Performance stability, as assessed via continuous biologically relevant stimulation pulses, revealed conventional PEDOT/PSS coatings were more resistant to delamination than macroporous coatings. However, the macroporous coatings exhibited interesting improvements in impedance prior to abrupt delamination after 500×10^3 pulses. Biocompatibility assays confirmed the ability of MEA devices and conventional and macroporous substrates to support the growth and viability of primary hippocampal neurons. No significant differences in neurite outgrowth and viability were observed between any of the substrates tested

when compared to positive control substrates.

To accompany the decrease in microelectrode thermal noise through CP modification, an amplification system was constructed with proportionately lower noise values. A target was set where the intrinsic amplifier noise would be at 45% (or less) of the microelectrode thermal noise [37]. Alongside this, the amplifier would need to be capable of amplifying neuronal signals. Two versions were constructed, the first version comprised (i) a high-pass filter, which removed DC offsets, (ii) a reference voltage offset set through a voltage divider, which allowed for the amplification of both positive and negative signals and (iii) two stages of amplification with a total gain of 2000 within the bandwidth of 7 to 10,000 Hz. Problems associated with the first version included an unstable reference voltage and poor amplifier front-end connections which resulted in environmental noise interference. Furthermore, the first amplifier presented an intrinsic noise value of $9.9 \mu\text{V}_{p-p}$ which only met the 45% threshold for gold microelectrodes, failing to meet this target for the lower thermal noise of conventional and macroporous PEDOT/PSS coatings. The revised amplifier consisted of a more accurate voltage reference and an improved MEA-to-amplifier connection method. Gain was redistributed (but kept at 2000) and was increased at the first stage of amplification (instrumentation amplifier) and reduced at the second stage (operational amplifier) within a wider bandwidth of 0.7 to 10,000 Hz. The modified amplifier resulted in reduced noise with an intrinsic value of $4.6 \mu\text{V}_{p-p}$, and met the lower threshold target of 45% microelectrode thermal noise for both conventional and macroporous PEDOT/PSS.

The MEA devices and data acquisition system were then used to characterise *in-vitro* recording performance and stimulation efficacy of gold, conventional PEDOT/PSS and macroporous PEDOT/PSS coatings. The recorded noise floor of conventional and macroporous PEDOT/PSS microelectrodes were consistently lower than unmodified gold microelectrodes both pre- and post-culture.

There were no significant differences between conventional and macroporous PEDOT/PSS coatings, in pre- or post-culture noise. Increases in recorded noise of over 100% were observed post-culture, when compared to pre-culture noise and was attributed to microelectrode biofouling processes. The max signal to noise (SNR) ratios of unmodified gold, conventional PEDOT/PSS and macroporous PEDOT/PSS were 2.72, 17.57 and 12.65, with mean values of 0.86, 5.43 and 4.14, respectively. The macroporous PEDOT/PSS coatings did not further improve *in-vitro* recorded performance of conventional PEDOT/PSS. Results for stimulation efficacy were not obtained due to limitations of the MEA devices used. The large inter-electrode distance on the MEA devices resulted in the use of the same microelectrode for both stimulation and recording. Noise introduced from the voltage source and post-stimulus artifacts made recording direct neuronal responses difficult. The stimulation pulse could be refined to decrease noise and post-stimulus artifact length. In the future, an altered MEA architecture could be used with paired stimulation and recording electrodes as well as investigating the use of older cultures (DIV 21) which are likely to be more active.

6.2 Limitations & Future Directions

6.2.1 Low Deposition Charge Density

Conventional and macroporous PEDOT/PSS coatings were deposited at deposition charge densities of 32, 127, 318 and 637 mC cm⁻². There were no significant differences in electrochemistry between conventional and macroporous PEDOT/PSS coatings at the lower deposition charge densities of 32, 127 and 318 mC cm⁻². However, at the deposition charge density of 637 mC cm⁻² a significant improvement in all electrochemical parameters (excluding CSC_c) was observed. This suggests that the macroporous coating becomes beneficial with thicker films. Future experiments should investigate this concept further and study whether increasing deposition charge densities beyond 637 mC cm⁻² reveals additional benefits of macroporous CP coating over conventional CP coatings.

6.2.2 Macroporous PEDOT/PSS Performance Stability

The reduced performance stability of macroporous PEDOT/PSS coatings when compared to conventional PEDOT/PSS coatings presents as a limiting factor for their use in long-term stimulation devices. The macroporous PEDOT/PSS coatings exhibited interesting improvements in impedance when subject to 500 x 10³ biphasic stimulation pulses or less. Further stimulation resulted in abrupt delamination. The improvement in impedance could have resulted from the macroporous structure, where long term stimulation resulted in repeated contraction and expansion of the CP [99, 157], exposing lower porous layers to the electrolyte and subsequently increasing the electrochemical surface area. Consequently, the reduced adhesion of the macroporous coatings to the underlying gold may have resulted from the highly porous, open network. Previous studies

have demonstrated the impact of dopant type and substrate material on CP adhesion [45,63,116,157]. Future works should investigate the influence of doping anion and substrate material/morphology to improve adhesion of macroporous coatings to the underlying substrate - yielding a mechanically stable stimulating electrode capable of improving charge transfer properties throughout its lifetime. Promising avenues for this future work would be utilising an iridium oxide (IrOx) adhesion layer and/or nanostructured platinum electrode substrates to improve macroporous CP adhesion, as suggested by Boehler et al. [157].

6.2.3 Signal to Noise Ratio Metric

As discussed in *Chapter 5*, the SNR metric is a common method of measuring microelectrode recording performance. One limitation of this metric is the exclusion of a neuronal distance parameter which is a key determinant of Sig_{p-p} amplitude. Therefore, a low impedance electrode could show low SNR values indicating poor performance, when in actual fact the neuron may be at a distant location. A system capable of visualising neuronal activity optically alongside electrical recordings through microelectrode may better inform transduction efficiency, and therefore, recording performance of the microelectrode material. We have made efforts towards such a system where neurons on the microelectrode array are labelled with voltage sensitive dyes (VSDs) which change their fluorescence intensity in response to membrane potential changes. VSDs offer the possibility to visualise, in real time, the activity of large neuronal populations with high spatial (up to $0.5 \mu\text{m}$ [158]) and temporal (μs) resolution [159]. The VSD labelled cells can be visualised through a fluorescent microscope and neuronal firing can be monitored using a high-speed CMOS (or CCD) camera (*Figure 6.1*).

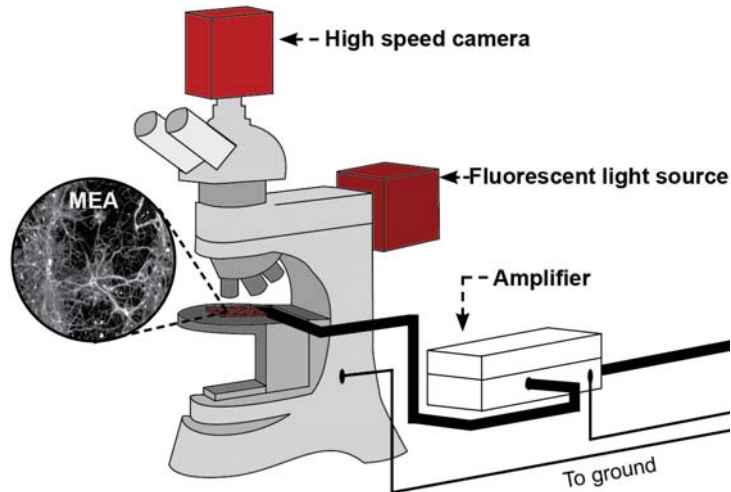


Figure 6.1: Illustration of the set-up used to obtain simultaneous electrical and optical signals from primary hippocampal cells cultured on MEA devices. The MEA devices sat on the microscope stage and shielded wires were connected to each of the electrodes through an interface board to enable electrical recording. The camera and mercury light source, required for fluorescent imaging of VSDs, were mounted onto the microscope.

This system would allow precise calculation of the distance between neuronal activity and the microelectrode. With a known distance, the expected potential at the microelectrode site can be modelled through *Equation 5.1* and a ‘performance factor’ can be calculated through *Equation 6.1*.

$$\text{Performance factor} = \frac{V_{\text{recorded}}}{V_{\text{expected}}} \quad (6.1)$$

The performance factor acts as a direct measure of microelectrode transduction efficacy and provides a better informed method towards characterisation of recording performance. *Figure 6.2* demonstrates the coupling of electrical and optical acquisition systems which record synchronously through digital cues. The representative electrical recording trace shown is derived from one conventional PEDOT/PSS microelectrode which is indicated on the images in *Figure 6.2* as a red encircled dot. Neuronal activity can clearly be seen optically and is in sync with recorded spikes from the PEDOT/PSS microelectrode. Spikes marked with a star (★) were identified electrically through the microelectrode

but not optically. This is due to the narrow field of view offered by the system and presents as a limiting factor. Ways to remedy this problem could be decreasing the objective lens magnification or adapting the set-up to be used with a fluorescent microscope capable of viewing the entire slide [160].

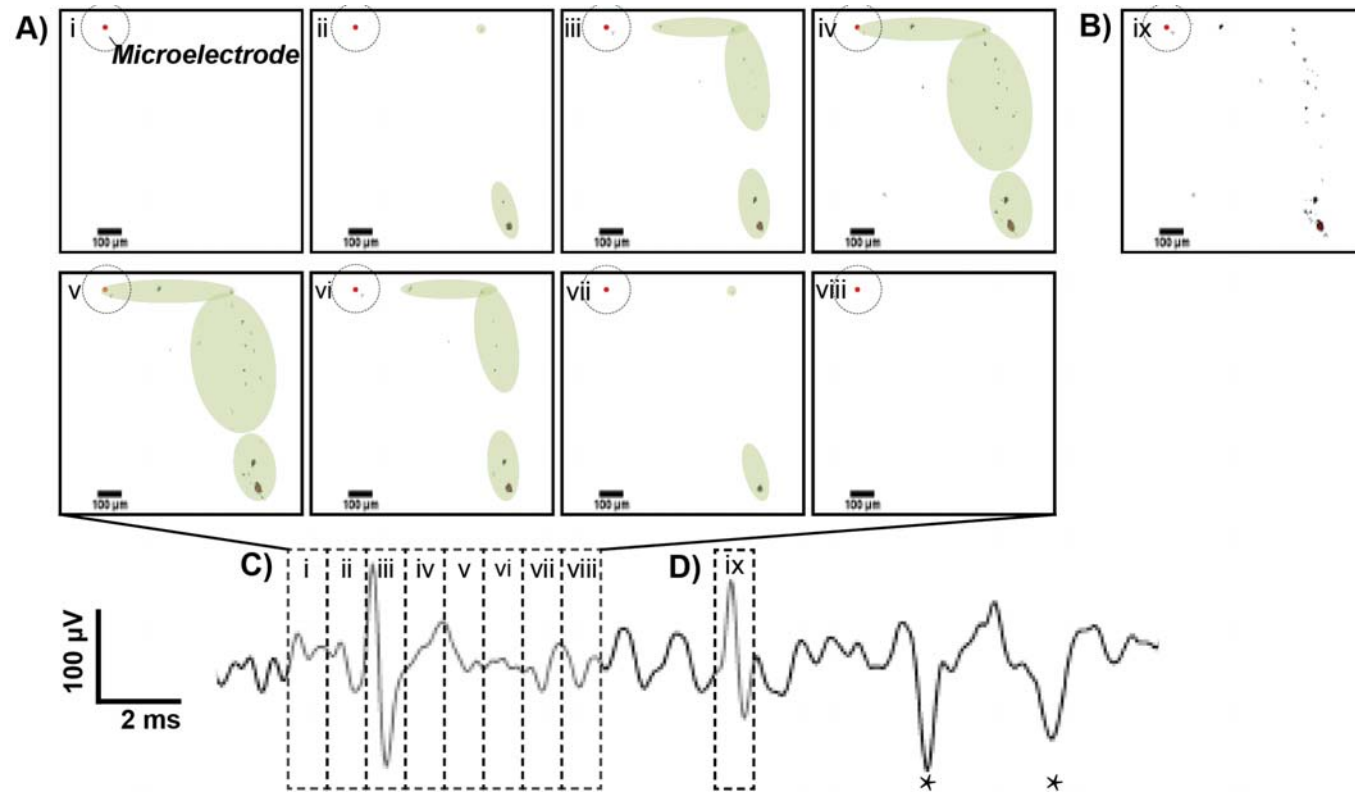


Figure 6.2: An example of combined electrical and optical recordings from a single electrode (indicated by a red encircled dot). The optical images A) and B) are correlated with action potentials C) and D) on the electrical trace, respectively. A breakdown of one action potential into 1 ms blocks is represented by A), where each time sequence in the optical image is correlated with a 1 ms block in the electrical trace through Roman numerals. The images were pseudo-colouring using an ImageJ look up table and neuronal activity was encircled with a green border to enable better visualisation of the active area. B) and D) represent another action potential recorded both optically and electrically (image only indicates when action potential is at its peak). Action potentials marked with a star (*) indicate those which were recorded electrically but not optically.

The recorded signals were confirmed to originate from neurons through use of tetrodotoxin (TTX), an inhibitor of neuronal action potentials through binding of voltage-gated sodium channels *Figure 6.3*. The optical images displayed in *Figure 6.3* indicate representative neuronal action potential maxima - this was done to simplify the figure, however, in reality more than one action potential was sensed optically. After 1 minute a significant reduction in electrical activity was noticed, optical imaging appeared to suffer from a slight loss in fluorescence intensity near the electrode. After 5 minutes, almost no action potentials could be sensed through the microelectrodes, and optical signals have started to show clear signs of diminishing activity. 20 minutes post TTX addition revealed diminished optical signals where only activity within the cell body could be sensed which is most likely due to sub-threshold activity [161].

These preliminary experiments are proof-of-concept that neuronal activity can be simultaneously visualised both optically and electrically to determine the performance factor of a microelectrode material. Limitations encountered to date revolve around the issue of noise in the recordings coming from the microscope and high speed camera as well as narrow field of view. The set-up also has applications in other scenarios such as the validation of spike sorting algorithms and improved detection of sub-threshold synaptic events which are can not be detected with sufficient resolution through extracellular microelectrodes [162–164].

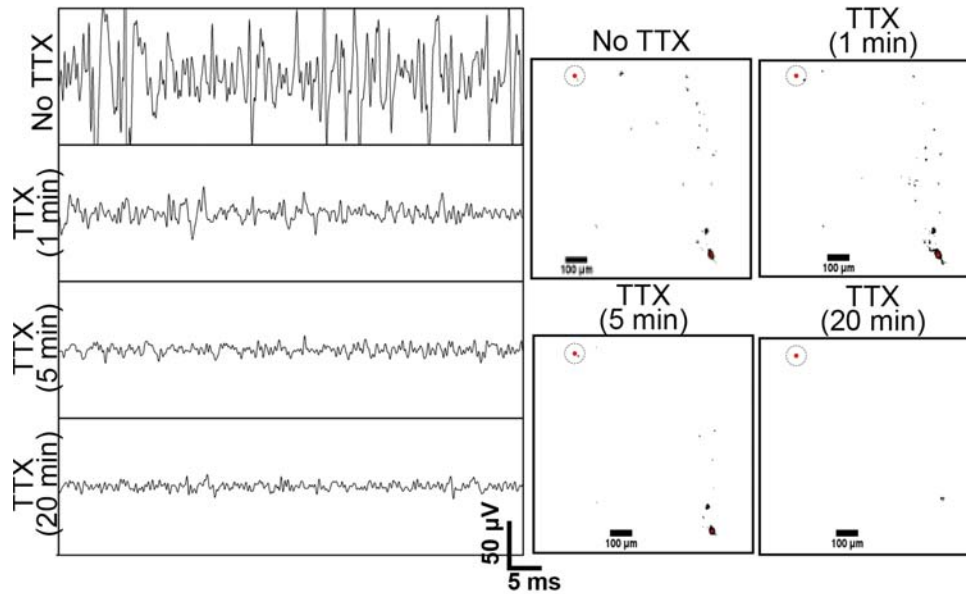


Figure 6.3: Signals were confirmed as neuronal action potentials due to antagonism following tetrodotoxin (TTX) addition. Optical images show a representative action potential maxima (when optical signals were strongest during an action potential cycle) within the 70 ms sampling interval.

6.2.4 Stimulation Efficacy

Unfortunately no data was obtained following *in-vitro* stimulation, limitations for this experiment were discussed in *Section 5.3.3*. Future work would revolve around redesigning the MEA to enable paired electrodes, where one electrode stimulates and surrounding electrodes record neuronal responses. The redesigned electrode configuration would incorporate a larger number of individually addressable microelectrode sites with inter-electrode spacing of 200 μm , or less [149]. To suppress noise from the voltage source alternative techniques to digital filtering, such as 50 Hz noise subtraction, can be applied so that neuronal signal rich frequency regions are not disturbed [165–167]. A commercial approach is the use of a Hum Bug Noise Eliminator (Quest Scientific, Canada) which subtracts a replica of the noise profile from the original signal [168]. In addition to MEA design, the use of young culture (DIV 7 and DIV 14) may have contributed to the lack of activity observed. Future experiments should utilise older cultures ($>$ DIV 14) to eliminate ‘premature’ neurons as a variable.

Bibliography

- [1] J. Pine, “Recording action potentials from cultured neurons with extracellular microcircuit electrodes,” *Journal of Neuroscience Methods*, vol. 2, no. 1, pp. 19–31, 1980.
- [2] C. A. Thomas Jr, P. A. Springer, G. E. Loeb, Y. Berwald-Netter, and L. M. Okun, “A miniature microelectrode array to monitor the bioelectric activity of cultured cells,” *Experimental Cell Research*, vol. 74, no. 1, pp. 61–66, 1972.
- [3] G. W. Gross, “Simultaneous single unit recording in vitro with a photoetched laser deinsulated gold multimicroelectrode surface,” *Biomedical Engineering, IEEE Transactions on*, vol. BME-26, no. 5, pp. 273–279, 1979.
- [4] G. W. Gross, E. Rieske, G. W. Kreutzberg, and A. Meyer, “A new fixed-array multi-microelectrode system designed for long-term monitoring of extracellular single unit neuronal activity in vitro,” *Neuroscience Letters*, vol. 6, no. 2–3, pp. 101–105, 1977.
- [5] H. Zhou, X. Cheng, L. Rao, T. Li, and Y. Y. Duan, “Poly(3,4-ethylenedioxythiophene)/multiwall carbon nanotube composite coatings for improving the stability of microelectrodes in neural prostheses applications,” *Acta Biomaterialia*, vol. 9, no. 5, pp. 6439–6449, 2013.
- [6] M. Heim, B. Yvert, and A. Kuhn, “Nanostructuring strategies to enhance microelectrode array (mea) performance for neuronal recording and stimulation,” *Journal of Physiology Paris*, vol. 106, no. 3-4, pp. 137–145, 2012.
- [7] R. Green and M. R. Abidian, “Conducting polymers for neural prosthetic and neural interface applications,” *Advanced Materials*, vol. 27, no. 46, pp. 7620–7637, 2015.
- [8] C. Boehler, T. Stieglitz, and M. Asplund, “Nanostructured platinum grass enables superior impedance reduction for neural microelectrodes,” *Biomaterials*, vol. 67, pp. 346–353, 2015.
- [9] H. Charkhkar, G. L. Knaack, D. G. McHail, H. S. Mandal, N. Peixoto, J. F. Rubinson, T. C. Dumas, and J. J. Pancrazio, “Chronic intracortical neural recordings using microelectrode arrays coated with pedot–tfb,” *Acta Biomaterialia*, vol. 32, pp. 57–67, 2016.

- [10] W. Franks, I. Schenker, P. Schmutz, and A. Hierlemann, "Impedance characterization and modeling of electrodes for biomedical applications," *IEEE Transactions on Biomedical Engineering*, vol. 52, no. 7, pp. 1295–302, 2005.
- [11] A. L. Kip, B. L. Nicholas, D. J. Mike, M. R.-B. Sarah, L. H. Jeffrey, and R. K. Daryl, "Poly(3,4-ethylenedioxythiophene) (pedot) polymer coatings facilitate smaller neural recording electrodes," *Journal of Neural Engineering*, vol. 8, no. 1, p. 014001, 2011.
- [12] A. R. Harris, S. J. Morgan, J. Chen, R. M. Kapsa, G. G. Wallace, and A. G. Paolini, "Conducting polymer coated neural recording electrodes," *Journal of Neural Engineering*, vol. 10, no. 1, pp. 1741–2560, 2013.
- [13] Z. J. Du, X. Luo, C. L. Weaver, and X. T. Cui, "Poly(3,4-ethylenedioxythiophene)-ionic liquid coating improves neural recording and stimulation functionality of meas," *Journal of Materials Chemistry C*, vol. 3, no. 25, pp. 6515–6524, 2015.
- [14] R. A. Green, N. H. Lovell, and L. A. Poole-Warren, "Cell attachment functionality of bioactive conducting polymers for neural interfaces," *Biomaterials*, vol. 30, no. 22, pp. 3637–3644, 2009.
- [15] J. Yang and D. C. Martin, "Microporous conducting polymers on neural microelectrode arrays: Ii. physical characterization," *Sensors and Actuators A: Physical*, vol. 113, no. 2, pp. 204–211, 2004.
- [16] K. J. Ressler and H. S. Mayberg, "Targeting abnormal neural circuits in mood and anxiety disorders: from the laboratory to the clinic," *Nature neuroscience*, vol. 10, no. 9, pp. 1116–1124, 2007.
- [17] A. M. Owen, "Cognitive dysfunction in parkinson's disease: the role of frontostriatal circuitry," *The Neuroscientist*, vol. 10, no. 6, pp. 525–537, 2004.
- [18] M. A. L. Nicolelis, "Brain-machine interfaces to restore motor function and probe neural circuits," *Nature Reviews Neuroscience*, vol. 4, no. 5, pp. 417–422, 2003.
- [19] M. A. Nicolelis, D. Dimitrov, J. M. Carmena, R. Crist, G. Lehew, J. D. Kralik, and S. P. Wise, "Chronic, multisite, multielectrode recordings in macaque monkeys," *Proceedings of the National academy of Sciences of the United States of America*, vol. 100, no. 19, pp. 11041–6, 2003.
- [20] M. E. Spira and A. Hai, "Multi-electrode array technologies for neuroscience and cardiology," *Nature Nanotechnology*, vol. 8, no. 2, pp. 83–94, 2013.
- [21] S. J. Rebscher, A. Hetherington, B. Bonham, P. Wardrop, D. Whinney, and P. A. Leake, "Considerations for design of future cochlear implant electrode arrays: electrode array stiffness, size, and depth of insertion," *Journal of Rehabilitation Research and Development*, vol. 45, no. 5, pp. 731–47, 2008.

- [22] r. Rizzo, J. F., J. Wyatt, J. Loewenstein, S. Kelly, and D. Shire, "Methods and perceptual thresholds for short-term electrical stimulation of human retina with microelectrode arrays," *Investigative Ophthalmology and Visual Science*, vol. 44, no. 12, pp. 5355–61, 2003.
- [23] J. G. Nicholls, *From Neuron to Brain*. Sinauer Associates, Incorporated, 2012.
- [24] A. L. Hodgkin and A. F. Huxley, "A quantitative description of membrane current and its application to conduction and excitation in nerve," *The Journal of Physiology*, vol. 117, no. 4, pp. 500–544, 1952.
- [25] P. Fromherz, "Electrical interfacing of nerve cells and semiconductor chips," *ChemPhysChem*, vol. 3, no. 3, pp. 276–284, 2002.
- [26] R. Kim, S. Joo, H. Jung, N. Hong, and Y. Nam, "Recent trends in micro-electrode array technology for in vitro neural interface platform," *Biomedical Engineering Letters*, vol. 4, no. 2, pp. 129–141, 2014.
- [27] A. Stett, U. Egert, E. Guenther, F. Hofmann, T. Meyer, W. Nisch, and H. Haemmerle, "Biological application of microelectrode arrays in drug discovery and basic research," *Analytical and Bioanalytical Chemistry*, vol. 377, no. 3, pp. 486–495, 2003.
- [28] B. C. Wheeler, "Building a brain on a chip," *Conference Proceedings IEEE Engineering in Medicine and Biology Society*, vol. 2008, pp. 1604–6, 2008.
- [29] S. Erkin, B. Yevgeny, R. B. Matthew, L. R. Michael, J. S. Kevin, and L. Y. Martin, "The fabrication of low-impedance nanoporous gold multiple-electrode arrays for neural electrophysiology studies," *Nanotechnology*, vol. 21, no. 12, p. 125504, 2010.
- [30] C. Wyart, C. Ybert, L. Bourdieu, C. Herr, C. Prinz, and D. Chatenay, "Constrained synaptic connectivity in functional mammalian neuronal networks grown on patterned surfaces," *Journal of Neuroscience Methods*, vol. 117, no. 2, pp. 123–131, 2002.
- [31] Y. J. Lo and M. M. Poo, "Heterosynaptic suppression of developing neuromuscular synapses in culture," *Journal of Neuroscience*, vol. 14, no. 8, pp. 4684–93, 1994.
- [32] M. Kwiat, R. Elnathan, A. Pevzner, A. Peretz, B. Barak, H. Peretz, T. Ducobni, D. Stein, L. Mittelman, U. Ashery, and F. Patolsky, "Highly ordered large-scale neuronal networks of individual cells – toward single cell to 3d nanowire intracellular interfaces," *ACS Applied Materials & Interfaces*, vol. 4, no. 7, pp. 3542–3549, 2012.
- [33] R. Bakker, D. Schubert, K. Levels, G. Bezgin, I. Bojak, and R. Kötter, "Classification of cortical microcircuits based on micro-electrode-array data from slices of rat barrel cortex," *Neural Networks*, vol. 22, no. 8, pp. 1159–1168, 2009.

- [34] D. R. Merrill, M. Bikson, and J. G. Jefferys, “Electrical stimulation of excitable tissue: design of efficacious and safe protocols,” *Journal of Neuroscience Methods*, vol. 141, no. 2, pp. 171–98, 2005.
- [35] D. A. Robinson, “The electrical properties of metal microelectrodes,” *Proceedings of the IEEE*, vol. 56, no. 6, pp. 1065–1071, 1968.
- [36] A. Hassibi, R. Navid, R. W. Dutton, and T. H. Lee, “Comprehensive study of noise processes in electrode electrolyte interfaces,” *Journal of Applied Physics*, vol. 96, no. 2, pp. 1074–1082, 2004.
- [37] M. E. J. Obien, K. Deligkaris, T. Bullmann, D. J. Bakkum, and U. Frey, “Revealing neuronal function through microelectrode array recordings,” *Frontiers in Neuroscience*, vol. 8, 2015.
- [38] R. Harrison and C. Charles, “A low-power low-noise cmos amplifier for neural recording applications,” *IEEE Journal of Solid-State Circuits*, vol. 38, no. 6, pp. 958–965, 2003.
- [39] C. Ferris, *Introduction to Bioinstrumentation: With Biological, Environmental, and Medical Applications*. Contemporary Instrumentation and Analysis, Humana Press, 1978.
- [40] D. Budai, “Ultralow-noise headstage and main amplifiers for extracellular spike recording,” *Acta Biologica Szegediensis*, vol. 48, no. 1-4, pp. 13–17, 2004.
- [41] C. H. Chen, S. H. Pun, P. U. Mak, M. I. Vai, A. Klug, and T. C. Lei, “Circuit models and experimental noise measurements of micropipette amplifiers for extracellular neural recordings from live animals,” *Biomed Research International*, vol. 2014, p. 14, 2014.
- [42] R. Harrison, P. Watkins, R. Kier, R. Lovejoy, D. Black, B. Greger, and F. Solzbacher, “A low-power integrated circuit for a wireless 100-electrode neural recording system,” *IEEE Journal of Solid-State Circuits*, vol. 42, no. 1, pp. 123–133, 2007.
- [43] S. F. Cogan, “Neural stimulation and recording electrodes,” *Annual Review of Biomedical Engineering*, vol. 10, no. 1, pp. 275–309, 2008.
- [44] R. D. Meyer, S. F. Cogan, T. H. Nguyen, and R. D. Rauh, “Electrode-deposited iridium oxide for neural stimulation and recording electrodes,” *IEEE Transactions on Neural Systems and Rehabilitation Engineering*, vol. 9, no. 1, pp. 2–11, 2001.
- [45] S. Baek, R. A. Green, and L. A. Poole-Warren, “Effects of dopants on the biomechanical properties of conducting polymer films on platinum electrodes,” *Journal of Biomedical Materials Research Part A*, vol. 102, no. 8, pp. 2743–2754, 2014.
- [46] K. Najafi, J. Ji, and K. D. Wise, “Scaling limitations of silicon multi-channel recording probes,” *Biomedical Engineering, IEEE Transactions on*, vol. 37, no. 1, pp. 1–11, 1990.

- [47] T. Nyberg, A. Shimada, and K. Torimitsu, "Ion conducting polymer microelectrodes for interfacing with neural networks," *Journal of Neuroscience Methods*, vol. 160, no. 1, pp. 16–25, 2007.
- [48] S. Venkatraman, J. Hendricks, Z. A. King, A. J. Sereno, S. Richardson-Burns, D. Martin, and J. M. Carmena, "In vitro and in vivo evaluation of pedot microelectrodes for neural stimulation and recording," *IEEE Transactions on Neural Systems and Rehabilitation Engineering*, vol. 19, no. 3, pp. 307–316, 2011.
- [49] S. B. Brummer, L. S. Robblee, and F. T. Hambrecht, "Criteria for selecting electrodes for electrical stimulation: Theoretical and practical considerations," *Annals of the New York Academy of Sciences*, vol. 405, no. 1, pp. 159–171, 1983.
- [50] V. Castagnola, E. Descamps, A. Lecestre, L. Dahan, J. Remaud, L. G. Nowak, and C. Bergaud, "Parylene-based flexible neural probes with pedot coated surface for brain stimulation and recording," *Biosensors and Bioelectronics*, vol. 67, pp. 450–457, 2015.
- [51] H. Charkhkar, G. L. Knaack, H. S. Mandal, E. W. Keefer, and J. J. Pancrazio, "Effects of carbon nanotube and conducting polymer coated microelectrodes on single-unit recordings in vitro," in *2014 36th Annual International Conference of the IEEE Engineering in Medicine and Biology Society, EMBC 2014*, pp. 469–473.
- [52] V. S. Polikov, P. A. Tresco, and W. M. Reichert, "Response of brain tissue to chronically implanted neural electrodes," *Journal of Neuroscience Methods*, vol. 148, no. 1, pp. 1–18, 2005.
- [53] B. C. Thompson, R. T. Richardson, S. E. Moulton, A. J. Evans, S. O'Leary, G. M. Clark, and G. G. Wallace, "Conducting polymers, dual neurotrophins and pulsed electrical stimulation — dramatic effects on neurite outgrowth," *Journal of Controlled Release*, vol. 141, no. 2, pp. 161–167, 2010.
- [54] R. Tang, W. Pei, S. Chen, H. Zhao, Y. Chen, Y. Han, C. Wang, and H. Chen, "Fabrication of strongly adherent platinum black coatings on microelectrodes array," *Science China Information Sciences*, vol. 57, no. 4, pp. 1–10, 2014.
- [55] X. Luo, C. L. Weaver, D. D. Zhou, R. Greenberg, and X. T. Cui, "Highly stable carbon nanotube doped poly(3,4-ethylenedioxythiophene) for chronic neural stimulation," *Biomaterials*, vol. 32, no. 24, pp. 5551–5557, 2011.
- [56] R. A. Green, N. H. Lovell, G. G. Wallace, and L. A. Poole-Warren, "Conducting polymers for neural interfaces: challenges in developing an effective long-term implant," *Biomaterials*, vol. 29, no. 24-25, pp. 3393–9, 2008.

- [57] Z. Aqrawe, J. Montgomery, J. Travas-Sejdic, and D. Svirskis, "Conducting polymers as electrode coatings for neuronal multi-electrode arrays," *Trends in Biotechnology*, vol. 35, no. 2, pp. 93–95, 2016.
- [58] S. Chen, W. Pei, Q. Gui, Y. Chen, S. Zhao, and H. Chen, "Multi-channel microelectrode array for cortical recording and stimulation: Fabrication and modification," in *8th Annual IEEE International Conference on Nano/Micro Engineered and Molecular Systems, IEEE NEMS 2013*, pp. 395–398.
- [59] Y. Hanein and L. Bareket-Keren, "Carbon nanotube-based multi electrode arrays for neuronal interfacing: progress and prospects," *Frontiers in Neural Circuits*, vol. 6, p. 122, 2013.
- [60] K. Wang, H. A. Fishman, H. Dai, and J. S. Harris, "Neural stimulation with a carbon nanotube microelectrode array," *Nano Letters*, vol. 6, no. 9, pp. 2043–2048, 2006.
- [61] M. R. Abidian, J. M. Corey, D. R. Kipke, and D. C. Martin, "Conducting-polymer nanotubes improve electrical properties, mechanical adhesion, neural attachment, and neurite outgrowth of neural electrodes," *Small*, vol. 6, no. 3, pp. 421–9, 2010.
- [62] S. F. Cogan, A. A. Guzelian, W. F. Agnew, T. G. Yuen, and D. B. McCreery, "Over-pulsing degrades activated iridium oxide films used for intracortical neural stimulation," *Journal of Neuroscience Methods*, vol. 137, no. 2, pp. 141 – 150, 2004.
- [63] R. A. Green, R. T. Hassarati, L. Bouchinet, C. S. Lee, G. L. M. Cheong, J. F. Yu, C. W. Dodds, G. J. Suaning, L. A. Poole-Warren, and N. H. Lovell, "Substrate dependent stability of conducting polymer coatings on medical electrodes," *Biomaterials*, vol. 33, no. 25, pp. 5875–5886, 2012.
- [64] X. Cui and D. C. Martin, "Electrochemical deposition and characterization of poly(3,4-ethylenedioxythiophene) on neural microelectrode arrays," *Sensors and Actuators B: Chemical*, vol. 89, no. 1–2, pp. 92–102, 2003.
- [65] D.-H. Kim, S. Richardson-Burns, J. Hendricks, C. Sequera, and D. Martin, "Effect of immobilized nerve growth factor on conductive polymers: Electrical properties and cellular response," *Advanced Functional Materials*, vol. 17, no. 1, pp. 79–86, 2007.
- [66] X. Cui, J. F. Hetke, J. A. Wiler, D. J. Anderson, and D. C. Martin, "Electrochemical deposition and characterization of conducting polymer polypyrrole/pss on multichannel neural probes," *Sensors and Actuators A: Physical*, vol. 93, no. 1, pp. 8–18, 2001.
- [67] X. Cui, V. A. Lee, Y. Raphael, J. A. Wiler, J. F. Hetke, D. J. Anderson, and D. C. Martin, "Surface modification of neural recording electrodes with conducting polymer/biomolecule blends.," *Journal of biomedical materials research*, vol. 56, pp. 261–72, Aug 2001.

- [68] R. Gerwig, K. Fuchsberger, B. Schroepel, G. S. Link, G. Heusel, U. Kraushaar, W. Schuhmann, A. Stett, and M. Stelzle, "Pedot-cnt composite microelectrodes for recording and electrostimulation applications: Fabrication, morphology, and electrical properties," *Frontiers in Neuroengineering*, vol. 5, p. 8, 2012.
- [69] B. M. Egeland, M. G. Urbanek, A. Peramo, S. M. Richardson-Burns, D. C. Martin, D. R. Kipke, J. Kuzon, W. M., and P. S. Cederna, "In vivo electrical conductivity across critical nerve gaps using poly(3,4-ethylenedioxythiophene)-coated neural interfaces," *Plastic and Reconstructive Surgery*, vol. 126, no. 6, pp. 1865–73, 2010.
- [70] M. R. Abidian and D. C. Martin, "Experimental and theoretical characterization of implantable neural microelectrodes modified with conducting polymer nanotubes," *Biomaterials*, vol. 29, no. 9, pp. 1273–83, 2008.
- [71] M. R. Abidian, K. A. Ludwig, T. C. Marzullo, D. C. Martin, and D. R. Kipke, "Interfacing conducting polymer nanotubes with the central nervous system: Chronic neural recording using poly(3,4-ethylenedioxythiophene) nanotubes," *Advanced Materials*, vol. 21, no. 37, pp. 3764–3770, 2009.
- [72] M. Asplund, T. Nyberg, and O. Inganäs, "Electroactive polymers for neural interfaces," *Polymer Chemistry*, vol. 1, no. 9, pp. 1374–1391, 2010.
- [73] A. J. Hackett, J. Malmstrom, P. J. Molino, J. E. Gautrot, H. Zhang, M. J. Higgins, G. G. Wallace, D. E. Williams, and J. Travas-Sejdic, "Conductive surfaces with dynamic switching in response to temperature and salt," *Journal of Materials Chemistry B*, vol. 3, no. 48, pp. 9285–9294, 2015.
- [74] L. T. Strover, J. Malmström, and J. Travas-Sejdic, "Graft copolymers with conducting polymer backbones: A versatile route to functional materials," *The Chemical Record*, vol. 16, no. 1, pp. 393–418, 2016.
- [75] L. T. Strover, J. Malmström, L. A. Stubbing, M. A. Brimble, and J. Travas-Sejdic, "Electrochemically-controlled grafting of hydrophilic brushes from conducting polymer substrates," *Electrochimica Acta*, vol. 188, pp. 57–70, 2016.
- [76] 2013.
- [77] J. Malmström, M. K. Nieuwoudt, L. T. Strover, A. Hackett, O. Laita, M. A. Brimble, D. E. Williams, and J. Travas-Sejdic, "Grafting from poly(3,4-ethylenedioxythiophene): A simple route to versatile electrically addressable surfaces," *Macromolecules*, vol. 46, no. 12, pp. 4955–4965, 2013.
- [78] J. Rivnay, R. M. Owens, and G. G. Malliaras, "The rise of organic bioelectronics," *Chemistry of Materials*, vol. 26, no. 1, pp. 679–685, 2014.
- [79] T. A. Skotheim, *Handbook of Conducting Polymers, Second Edition*. Taylor & Francis, 1997.

- [80] M. F. John, F. Leandro, N. Hieu, D. B. James, K. Yann-Fuu, S.-N. Jeja, and E. S. Christine, "Biocompatibility implications of polypyrrole synthesis techniques," *Biomedical Materials*, vol. 3, no. 3, p. 034124, 2008.
- [81] S. Baek, R. A. Green, and L. A. Poole-Warren, "The biological and electrical trade-offs related to the thickness of conducting polymers for neural applications," *Acta Biomaterialia*, vol. 10, no. 7, pp. 3048–3058, 2014.
- [82] A. Michalska, A. Gałuszkiewicz, M. Ogonowska, M. Ocypa, and K. Maksymiuk, "Pedot films: multifunctional membranes for electrochemical ion sensing," *Journal of Solid State Electrochemistry*, vol. 8, no. 6, pp. 381–389, 2004.
- [83] M. Vázquez, J. Bobacka, A. Ivaska, and A. Lewenstam, "Influence of oxygen and carbon dioxide on the electrochemical stability of poly(3,4-ethylenedioxythiophene) used as ion-to-electron transducer in all-solid-state ion-selective electrodes," *Sensors and Actuators B: Chemical*, vol. 82, no. 1, pp. 7–13, 2002.
- [84] H. Yamato, M. Ohwa, and W. Wernet, "Stability of polypyrrole and poly(3,4-ethylenedioxythiophene) for biosensor application," *Journal of Electroanalytical Chemistry*, vol. 397, no. 1–2, pp. 163–170, 1995.
- [85] P. Pfluger and G. B. Street, "Chemical, electronic, and structural properties of conducting heterocyclic polymers: A view by xps," *The Journal of Chemical Physics*, vol. 80, no. 1, pp. 544–553, 1984.
- [86] E. Tamburri, S. Orlanducci, F. Toschi, M. L. Terranova, and D. Passeri, "Growth mechanisms, morphology, and electroactivity of pedot layers produced by electrochemical routes in aqueous medium," *Synthetic Metals*, vol. 159, no. 5–6, pp. 406–414, 2009.
- [87] H. S. Mandal, G. L. Knaack, H. Charkhkar, D. G. McHail, J. S. Kastee, T. C. Dumas, N. Peixoto, J. F. Rubinson, and J. J. Pancrazio, "Improving the performance of poly(3,4-ethylenedioxythiophene) for brain-machine interface applications," *Acta Biomaterialia*, vol. 10, no. 6, pp. 2446–2454, 2014.
- [88] A. L. Kip, D. U. Jeffrey, Y. Junyan, C. M. David, and R. K. Daryl, "Chronic neural recordings using silicon microelectrode arrays electrochemically deposited with a poly(3,4-ethylenedioxythiophene) (pedot) film," *Journal of Neural Engineering*, vol. 3, no. 1, p. 59, 2006.
- [89] S. Wilks, S. Richardson-Burn, J. Hendricks, D. Martin, and K. Otto, "Poly(3,4-ethylene dioxythiophene) (pedot) as a micro-neural interface material for electrostimulation," *Frontiers in Neuroengineering*, vol. 2, p. 7, 2009.
- [90] J. M. Fonner, L. Forciniti, H. Nguyen, J. Byrne, Y.-F. Kou, J. Syeda-Nawaz, and C. E. Schmidt, "Biocompatibility implications of polypyrrole synthesis techniques," *Biomedical materials (Bristol, England)*, vol. 3, no. 3, pp. 034124–034124, 2008.

- [91] B. C. Thompson, S. E. Moulton, R. T. Richardson, and G. G. Wallace, "Effect of the dopant anion in polypyrrole on nerve growth and release of a neurotrophic protein," *Biomaterials*, vol. 32, no. 15, pp. 3822–31, 2011.
- [92] C. Vallejo-Giraldo, A. Kelly, and M. J. P. Biggs, "Biofunctionalisation of electrically conducting polymers," *Drug Discovery Today*, vol. 19, no. 1, pp. 88–94, 2014.
- [93] X. Strakosas, B. Wei, D. C. Martin, and R. M. Owens, "Biofunctionalization of polydioxothiophene derivatives for biomedical applications," *Journal of Materials Chemistry B*, vol. 4, no. 29, pp. 4952–4968, 2016.
- [94] T. D. Y. Kozai, K. Catt, Z. Du, K. Na, O. Srivannavit, R. u. M. Haque, J. Seymour, K. D. Wise, E. Yoon, and X. T. Cui, "Chronic in vivo evaluation of pedot:cnt for stable neural recordings," *IEEE Transactions on Biomedical Engineering*, vol. 63, pp. 111–119, Jan 2016.
- [95] J. W. Gunn, S. D. Turner, and B. K. Mann, "Adhesive and mechanical properties of hydrogels influence neurite extension," *Journal of Biomedical Materials Research. Part A*, vol. 72, no. 1, pp. 91–7, 2005.
- [96] G. L. Mario Cheong, K. S. Lim, A. Jakubowicz, P. J. Martens, L. A. Poole-Warren, and R. A. Green, "Conductive hydrogels with tailored bioactivity for implantable electrode coatings," *Acta Biomaterialia*, vol. 10, no. 3, pp. 1216–1226, 2014.
- [97] D.-H. Kim, J. A. Wiler, D. J. Anderson, D. R. Kipke, and D. C. Martin, "Conducting polymers on hydrogel-coated neural electrode provide sensitive neural recordings in auditory cortex," *Acta Biomaterialia*, vol. 6, no. 1, pp. 57–62, 2010.
- [98] R. A. Green, S. Baek, L. A. Poole-Warren, and P. J. Martens, "Conducting polymer-hydrogels for medical electrode applications," *Science and Technology of Advanced Materials*, vol. 11, no. 1, p. 014107, 2010.
- [99] D. Svirskis, J. Travas-Sejdic, A. Rodgers, and S. Garg, "Electrochemically controlled drug delivery based on intrinsically conducting polymers," *Journal of Controlled Release*, vol. 146, no. 1, pp. 6–15, 2010.
- [100] S. Golde, A. Coles, J. A. Lindquist, and A. Compston, "Decreased inos synthesis mediates dexamethasone-induced protection of neurons from inflammatory injury in vitro," *European Journal of Neuroscience*, vol. 18, no. 9, pp. 2527–2537, 2003.
- [101] W. Shain, L. Spataro, J. Dilgen, K. Haverstick, S. Retterer, M. Isaacson, M. Saltzman, and J. N. Turner, "Controlling cellular reactive responses around neural prosthetic devices using peripheral and local intervention strategies," *Neural Systems and Rehabilitation Engineering, IEEE Transactions on*, vol. 11, no. 2, pp. 186–188, 2003.
- [102] M. Asplund, C. Boehler, and T. Stieglitz, "Anti-inflammatory polymer electrodes for glial scar treatment: bringing the conceptual idea to future results," *Frontiers in Neuroengineering*, vol. 7, p. 9, 2014.

- [103] A. Seyfoddin, A. Chan, W. T. Chen, I. D. Rupenthal, G. I. N. Waterhouse, and D. Svirskis, "Electro-responsive macroporous polypyrrole scaffolds for triggered dexamethasone delivery," *European Journal of Pharmaceutics and Biopharmaceutics*, vol. 94, pp. 419–426, 2015.
- [104] C. L. Kolarcik, K. Catt, E. Rost, I. N. Albrecht, D. Bourbeau, Z. Du, T. D. Y. Kozai, X. Luo, D. J. Weber, and X. T. Cui, "Evaluation of poly(3,4-ethylenedioxythiophene)/carbon nanotube neural electrode coatings for stimulation in the dorsal root ganglion," *Journal of Neural Engineering*, vol. 12, no. 1, p. 016008, 2015.
- [105] A. D. McNaught and A. Wilkinson, *IUPAC. Compendium of Chemical Terminology*. Blackwell Scientific Publications, 2 ed., 1997.
- [106] G. I. N. Waterhouse and M. R. Waterland, "Opal and inverse opal photonic crystals: Fabrication and characterization," *Polyhedron*, vol. 26, no. 2, pp. 356–368, 2007.
- [107] MicroChemicals, *Baking steps in photoresists processing*. MicroChemicals, 2013.
- [108] Z. Zhang, P. Zhao, G. Xiao, B. R. Watts, and C. Xu, "Sealing sub-8 microfluidic channels using pdms," *Biomicrofluidics*, vol. 5, no. 4, pp. 046503–046503–8, 2011.
- [109] S.-E. Shim, Y.-J. Cha, J.-M. Byun, and S. Choe, "Size control of polystyrene beads by multistage seeded emulsion polymerization," *Journal of Applied Polymer Science*, vol. 71, no. 13, pp. 2259–2269, 1999.
- [110] M. Sharma, G. I. N. Waterhouse, S. W. C. Loader, S. Garg, and D. Svirskis, "High surface area polypyrrole scaffolds for tunable drug delivery," *International Journal of Pharmaceutics*, vol. 443, no. 1–2, pp. 163–168, 2013.
- [111] J. Bobacka, A. Lewenstam, and A. Ivaska, "Electrochemical impedance spectroscopy of oxidized poly(3,4-ethylenedioxythiophene) film electrodes in aqueous solutions," *Journal of Electroanalytical Chemistry*, vol. 489, no. 1–2, pp. 17–27, 2000.
- [112] H. Nyquist, "Thermal agitation of electric charge in conductors," *Physical Review*, vol. 32, pp. 110–113, Jul 1928.
- [113] J. E. Cheyne, L. Grant, C. Butler-Munro, J. W. Foote, B. Connor, and J. M. Montgomery, "Synaptic integration of newly generated neurons in rat dissociated hippocampal cultures," *Molecular and Cellular Neuroscience*, vol. 47, no. 3, pp. 203–214, 2011.
- [114] M. H. Arons, C. J. Thynne, A. M. Grabrucker, D. Li, M. Schoen, J. E. Cheyne, T. M. Boeckers, J. M. Montgomery, and C. C. Garner, "Autism-associated mutations in prosap2/shank3 impair synaptic transmission and neurexin–neuroligin-mediated transsynaptic signaling," *The Journal of Neuroscience*, vol. 32, no. 43, pp. 14966–14978, 2012.

- [115] R. T. Hassarati, L. J. R. Foster, and R. A. Green, "Influence of biphasic stimulation on olfactory ensheathing cells for neuroprosthetic devices," 2016.
- [116] R. Green, *Conducting polymers for neural interfaces: impact of physico-chemical properties on biological performance*. PhD thesis, University of New South Wales, 2009.
- [117] C. Hassler, T. Boretius, and T. Stieglitz, "Polymers for neural implants," *Journal of Polymer Science Part B: Polymer Physics*, vol. 49, no. 1, pp. 18–33, 2011.
- [118] L. Yue, S. Wang, X. Zhao, and L. Zhang, "Nano-silicon composites using poly(3,4-ethylenedioxythiophene):poly(styrenesulfonate) as elastic polymer matrix and carbon source for lithium-ion battery anode," *Journal of Materials Chemistry*, vol. 22, pp. 1094–1099, 2012.
- [119] D. Alemu, H.-Y. Wei, K.-C. Ho, and C.-W. Chu, "Highly conductive pedot:pss electrode by simple film treatment with methanol for ito-free polymer solar cells," *Energy & Environmental Science*, vol. 5, pp. 9662–9671, 2012.
- [120] I. Rodríguez-Ruiz, A. Llobera, J. Vila-Planas, D. W. Johnson, J. Gómez-Morales, and J. M. García-Ruiz, "Analysis of the structural integrity of su-8-based optofluidic systems for small-molecule crystallization studies," *Analytical Chemistry*, vol. 85, no. 20, pp. 9678–9685, 2013.
- [121] K. Aoki, "Theory of ultramicroelectrodes," *Electroanalysis*, vol. 5, no. 8, pp. 627–639, 1993.
- [122] G. T. A. Kovacs, "Introduction to the theory, design and modeling of thin-film microelectrodes for neural interfaces," in *Enabling Technologies for Cultured Neural Networks* (D. A. Stenger and T. M. McKenna, eds.), pp. 121–165+, Academic Press, 1994.
- [123] R. A. Green, P. B. Matteucci, C. W. D. Dodds, J. Palmer, W. F. Dueck, R. T. Hassarati, P. J. Byrnes-Preston, N. H. Lovell, and G. J. Suaning, "Laser patterning of platinum electrodes for safe neurostimulation," *Journal of Neural Engineering*, vol. 11, no. 5, p. 056017, 2014.
- [124] C. E. Schmidt, V. R. Shastri, J. P. Vacanti, and R. Langer, "Stimulation of neurite outgrowth using an electrically conducting polymer," *Proceedings of the National Academy of Sciences of the United States of America*, vol. 94, no. 17, pp. 8948–53, 1997.
- [125] J. Y. Lee, C. A. Bashur, A. S. Goldstein, and C. E. Schmidt, "Polypyrrole-coated electrospun {PLGA} nanofibers for neural tissue applications," *Biomaterials*, vol. 30, no. 26, pp. 4325 – 4335, 2009.
- [126] Y. Geerts, M. Steyaert, and W. Sansen, *Design of Multi-Bit Delta-Sigma A/D Converters*. Kluwer International Series in, Springer, 2002.

- [127] D. Fan, D. Rich, T. Holtzman, P. Ruther, J. Dalley, A. Lopez, M. Rossi, J. Barter, D. Salas-Meza, S. Herwik, T. Holzhammer, J. Morizio, and H. Yin, “A wireless multi-channel recording system for freely behaving mice and rats,” *PLOS ONE*, vol. 6, no. 7, 2011.
- [128] R. H. I. I. Olsson, A. N. Gulari, and K. D. Wise, “A fully-integrated bandpass amplifier for extracellular neural recording,” in *First International IEEE EMBS Conference on Neural Engineering, 2003. Conference Proceedings.*, pp. 165–168, March 2003.
- [129] S. Park, D. Borton, M. Kang, A. Nurmikko, and Y.-K. Song, “An implantable neural sensing microsystem with fiber-optic data transmission and power delivery,” *Sensors (Switzerland)*, vol. 13, no. 5, pp. 6014–6031, 2013.
- [130] G. Perlin and K. Wise, “An ultra compact integrated front end for wireless neural recording microsystems,” *Journal of Microelectromechanical Systems*, vol. 19, no. 6, pp. 1409–1421, 2010.
- [131] M. Yin and M. Ghovanloo, “A low-noise preamplifier with adjustable gain and bandwidth for biopotential recording applications,” pp. 321–324, 2007.
- [132] M. Yin, S. B. Lee, and M. Ghovanloo, “In vivo testing of a low noise 32-channel wireless neural recording system.,” *Annual International Conference of the IEEE Engineering in Medicine and Biology Society.*, vol. 2009, pp. 1608–11, 2009.
- [133] L. Technology, *LT3042 20V, 200mA, Ultralow Noise, Ultrahigh PSRR RF Linear Regulator*. Linear Technology.
- [134] P. Molnar and J. Hickman, *Patch-Clamp Methods and Protocols*. Methods in Molecular Biology, Humana Press, 2007.
- [135] K. P. Eaton and C. S. Henriquez, “Confounded spikes generated by synchrony within neural tissue models,” *Neurocomputing*, vol. 65–66, pp. 851 – 857, 2005.
- [136] J. Martinez, C. Pedreira, M. J. Ison, and R. Q. Quiroga, “Realistic simulation of extracellular recordings,” *Journal of Neuroscience Methods*, vol. 184, no. 2, pp. 285 – 293, 2009.
- [137] D. Jäckel, U. Frey, M. Fiscella, F. Franke, and A. Hierlemann, “Applicability of independent component analysis on high-density microelectrode array recordings,” *Journal of Neurophysiology*, vol. 108, p. 334, July 2012.
- [138] L. A. Camuñas-Mesa and R. Q. Quiroga, “A detailed and fast model of extracellular recordings,” *Neural Computation*, vol. 25, no. 5, pp. 1191–1212, 2013.
- [139] R. C. Gesteland, B. Howland, J. Y. Lettvin, and W. H. Pitts, “Comments on microelectrodes,” *Proceedings of the IRE*, vol. 47, pp. 1856–1862, Nov 1959.

- [140] X. Liu, A. Demosthenous, and N. Donaldson, "On the noise performance of pt electrodes," *Conference Proceedings IEEE Engineering in Medicine and Biology Society*, vol. 2007, pp. 434–6, 2007.
- [141] S. Musa, D. R. Rand, C. Bartic, W. Eberle, B. Nuttin, and G. Borghs, "Coulometric detection of irreversible electrochemical reactions occurring at pt microelectrodes used for neural stimulation," *Analytical Chemistry*, vol. 83, no. 11, pp. 4012–4022, 2011.
- [142] J. McHardy, L. S. Robblee, J. M. Marston, and S. B. Brummer, "Electrical stimulation with pt electrodes. iv. factors influencing pt dissolution in inorganic saline," *Biomaterials*, vol. 1, no. 3, pp. 129–34, 1980.
- [143] T. Narahashi, J. W. Moore, and W. R. Scott, "Tetrodotoxin blockage of sodium conductance increase in lobster giant axons.," *The Journal of general physiology*, vol. 47, pp. 965–74, May 1964.
- [144] B. Hille, *Ionic Channels of Excitable Membranes*. Sinauer, 2001.
- [145] R. Q. Quiroga, Z. Nadasdy, and Y. Ben-Shaul, "Unsupervised spike detection and sorting with wavelets and superparamagnetic clustering," *Neural Computation*, vol. 16, no. 8, pp. 1661–1687, 2004.
- [146] D. L. Donoho and J. M. Johnstone, "Ideal spatial adaptation by wavelet shrinkage," *Biometrika*, vol. 81, no. 3, p. 425, 1994.
- [147] W. Press, *Numerical Recipes 3rd Edition: The Art of Scientific Computing*. Cambridge University Press, 2007.
- [148] M. Blatt, S. Wiseman, and E. Domany, "Superparamagnetic clustering of data," *Physical Review Letters*, vol. 76, pp. 3251–3254, Apr 1996.
- [149] D. A. Wagenaar, J. Pine, and S. M. Potter, "Effective parameters for stimulation of dissociated cultures using multi-electrode arrays," *Journal of Neuroscience Methods*, vol. 138, no. 1, pp. 27 – 37, 2004.
- [150] S. F. Lempka, M. D. Johnson, M. A. Moffitt, K. J. Otto, D. R. Kipke, and C. C. McIntyre, "Theoretical analysis of intracortical microelectrode recordings," *Journal of Neural Engineering*, vol. 8, no. 4, p. 045006, 2011.
- [151] S. F. Lempka, M. D. Johnson, D. W. Barnett, M. A. Moffitt, K. J. Otto, D. R. Kipke, and C. C. McIntyre, "Optimization of microelectrode design for cortical recording based on thermal noise considerations," in *2006 International Conference of the IEEE Engineering in Medicine and Biology Society*, pp. 3361–3364, Aug 2006.
- [152] P. Daggumati, Z. Matharu, L. Wang, and E. Seker, "Biofouling-resilient nanoporous gold electrodes for dna sensing," *Analytical Chemistry*, vol. 87, no. 17, pp. 8618–8622, 2015.
- [153] T. D. Y. Kozai, N. B. Langhals, P. R. Patel, X. Deng, H. Zhang, K. L. Smith, J. Lahann, N. A. Kotov, and D. R. Kipke, "Ultrasmall implantable composite microelectrodes with bioactive surfaces for chronic neural interfaces," *Nature Materials*, vol. 11, pp. 1065–73, Dec 2012.

- [154] E. W. C. Chan, P. Baek, D. Barker, and J. Travas-Sejdic, “Highly functionalisable polythiophene phenylenes,” *Polymer Chemistry*, vol. 6, no. 43, pp. 7618–7629, 2015.
- [155] T. Narahashi, “Pharmacology of tetrodotoxin,” *Journal of Toxicology: Toxin Reviews*, vol. 20, no. 1, pp. 67–84, 2001.
- [156] G. Baranauskas, E. Maggiolini, E. Castagnola, A. Ansaldo, A. Mazzoni, G. N. Angotzi, A. Vato, D. Ricci, S. Panzeri, and L. Fadiga, “Carbon nanotube composite coating of neural microelectrodes preferentially improves the multiunit signal-to-noise ratio,” *Journal of Neural Engineering*, vol. 8, no. 6, p. 066013, 2011.
- [157] C. Boehler, F. Oberueber, S. Schlabach, T. Stieglitz, and M. Asplund, “Long-term stable adhesion for conducting polymers in biomedical applications: Irox and nanostructured platinum solve the chronic challenge,” *ACS Applied Materials & Interfaces*, vol. 9, no. 1, pp. 189–197, 2017.
- [158] A. Grinvald and R. Hildesheim, “VSDI: a new era in functional imaging of cortical dynamics,” *Nature Reviews. Neuroscience*, vol. 5, pp. 874–885, Nov. 2004.
- [159] S. Chemla and F. Chavane, “Voltage-sensitive dye imaging: Technique review and models,” *Journal of Physiology-Paris*, vol. 104, no. 1–2, pp. 40 – 50, 2010.
- [160] J. S. Blackburn, S. Liu, A. R. Raimondi, M. S. Ignatius, C. D. Salthouse, and D. M. Langenau, “High-throughput imaging of adult fluorescent zebrafish with an led fluorescence microscope,” *Nature Protocols*, vol. 6, pp. 229–241, Feb. 2011.
- [161] F. Colomo and S. D. Erulkar, “Miniature synaptic potentials at frog spinal neurones in the presence of tetrodotoxin,” *The Journal of Physiology*, vol. 199, pp. 205–221, Nov. 1968.
- [162] M. Taketani and M. Baudry, *Advances in Network Electrophysiology: Using Multi-Electrode Arrays*. Alpha Med Sciences, Springer, 2006.
- [163] M. Hutzler, A. Lambacher, B. Eversmann, M. Jenkner, R. Thewes, and P. Fromherz, “High-resolution multitransistor array recording of electrical field potentials in cultured brain slices,” *Journal of Neurophysiology*, vol. 96, no. 3, pp. 1638–1645, 2006.
- [164] L. Berdondini, K. Imfeld, A. Maccione, M. Tedesco, S. Neukom, M. Koudelka-Hep, and S. Martinoia, “Active pixel sensor array for high spatio-temporal resolution electrophysiological recordings from single cell to large scale neuronal networks,” *Lab on a chip*, vol. 9, pp. 2644–51, Sep 2009.
- [165] J. C. Huhta and J. G. Webster, “60 hz interference in electrocardiography,” *IEEE Transactions on Biomedical Engineering*, vol. 20, 1973.

- [166] I. A. Dotsinsky and I. K. Daskalov, "Comments on 'dynamic levkov-christov subtraction of mains interference'," *Medical and Biological Engineering and Computing*, vol. 33, 1995.
- [167] G. Mihov, I. Dotsinsky, and T. s. Georgieva, "Subtraction procedure for power-line interference removing from ecg: Improvement for non-multiple sampling," *Journal of Medical and Engineering Technology*, vol. 29, 2005.
- [168] Quest Scientific, *Hum Bug 50/60 Hz Noise Eliminator Reference Manual*, Feb. 2010.

**JOHN WILEY AND SONS LICENSE
TERMS AND CONDITIONS**

This Agreement between Zaid Aqrawe ("You") and John Wiley and Sons ("John Wiley and Sons") consists of your license details and the terms and conditions provided by John Wiley and Sons and Copyright Clearance Center.

License Number	4138490107596
License date	Jun 29, 2017
Licensed Content Publisher	John Wiley and Sons
Licensed Content Publication	Small
Licensed Content Title	Conducting-Polymer Nanotubes Improve Electrical Properties, Mechanical Adhesion, Neural Attachment, and Neurite Outgrowth of Neural Electrodes
Licensed Content Author	Mohammad Reza Abidian, Joseph M. Corey, Daryl R. Kipke, David C. Martin
Licensed Content Date	Jan 13, 2010
Licensed Content Pages	9
Type of use	Dissertation/Thesis
Requestor type	University/Academic
Format	Print and electronic
Portion	Figure/table
Number of figures/tables	1
Original Wiley figure/table number(s)	2
Will you be translating?	No
Title of your thesis / dissertation	Optimising Recording and Stimulation Performance of Neuronal Microelectrode Arrays through Macroporous Conducting Polymer Modification
Expected completion date	Jun 2017
Expected size (number of pages)	220
Requestor Location	Zaid Aqrawe 85 Park Road Grafton Auckland, 1023 New Zealand Attn: Zaid Aqrawe
Publisher Tax ID	EU826007151
Billing Type	Invoice
Billing Address	Zaid Aqrawe 85 Park Road

ELSEVIER LICENSE TERMS AND CONDITIONS

This Agreement between Zaid Aqrawe ("You") and Elsevier ("Elsevier") consists of your license details and the terms and conditions provided by Elsevier and Copyright Clearance Center.

License Number	4138490260749
License date	Jun 29, 2017
Licensed Content Publisher	Elsevier
Licensed Content Publication	Acta Biomaterialia
Licensed Content Title	Improving the performance of poly(3,4-ethylenedioxythiophene) for brain-machine interface applications
Licensed Content Author	Himadri S. Mandal,Gretchen L. Knaack,Hamid Charkhkar,Daniel G. McHail,Jemika S. Kastee,Theodore C. Dumas,Nathalia Peixoto,Judith F. Rubinson,Joseph J. Pancrazio
Licensed Content Date	Jun 1, 2014
Licensed Content Volume	10
Licensed Content Issue	6
Licensed Content Pages	9
Start Page	2446
End Page	2454
Type of Use	reuse in a thesis/dissertation
Intended publisher of new work	other
Portion	figures/tables/illustrations
Number of figures/tables/illustrations	1
Format	both print and electronic
Are you the author of this Elsevier article?	No
Will you be translating?	No
Original figure numbers	7
Title of your thesis/dissertation	Optimising Recording and Stimulation Performance of Neuronal Microelectrode Arrays through Macroporous Conducting Polymer Modification
Expected completion date	Jun 2017
Estimated size (number of pages)	220
Requestor Location	Zaid Aqrawe 85 Park Road Grafton